Two-Photon Physics and Online Beam Monitoring Using the DELPHI Detector at LEP

A Thesis Submitted for the Degree of
Doctor of Philosophy in Physics
by

Jonas Bjarne

DEPARTMENT OF PHYSICS, UNIVERSITY OF LUND
LUND, 1994

Organization **LUND UNIVERSITY** Department of Physics, University of Lund, Sölvegatan 14, S-223 62 Lund, Sweden	Document name **DOCTORAL DISSERTATION** Date of issue September 6, 1994 CODEN: LUNFD6/(NFFL-7089)1994
Author(s) Jonas Bjarne	**Sponsoring organization**

Title and subtitle

Two-Photon Physics and Online Beam Monitoring Using the DELPHI Detector at LEP

Abstract

This thesis is based on work done during 1989-1993 using the DELPHI detector at LEP, which is summarised in five articles. It consists of three main parts.

The first part describes the Very Small Angle Tagger (VSAT), which is a sub-detector of the DELPHI detector at LEP. It consists of four silicon-tungsten electromagnetic calorimeter modules having silicon strip planes for position determination. The modules are placed adjacent to the beam pipe, at ± 7.7 m from the interaction point and after superconducting quadrupole magnets, allowing the detection of electrons in a polar angle range of 4 to 13 mrad.

The second part is devoted to two-photon physics at DELPHI, with strong emphasis on a VSAT single-tagged event analysis. Here is shown, for the first time, evidence of hard scattering processes in single tagged two-photon collisions. A QCD Resolved Photon Contribution (QCD-RPC) model is introduced. Data is then seen to be well described by a full VDM+QPM+(QCD-RPC) model. Different parton density functions are compared with data.

The third part first describes the system for online monitoring of LEP beam background and luminosity at the DELPHI interaction point. Details are given of contributing sub-detector signals and program structure. Then follows a description of the VSAT online monitoring program (`VSAT_MONITOR`). A good agreement is found between the `VSAT_MONITOR` estimates of luminosity and beam spot and those of other detectors. Finally, results are presented of VSAT measurements of a LEP beam separation scan.

Key words
LEP, DELPHI, VSAT, electromagnetic calorimeter, two-photon physics, hard scattering, parton density function, online beam monitoring, luminosity, beam spot, beam separation

Classification system and/or index terms (if any)

Supplementary bibliographical information | **Language** English

ISSN and key title | **ISBN** 91-628-1388-9

Recipient's notes | **Number of pages** 126 | **Price**

Security classification

Distribution by (name and address) Jonas Bjarne, Department of Physics, University of Lund, Sölvegatan 14, S-223 62 Lund, Sweden

Signature Jonas Bjarne **Date** September 6, 1994

KRONTRYCK - ESLÖV

ISBN 91-628-1388-9
LUNFD6/(NFFL-7089)1994

Two-Photon Physics and Online Beam Monitoring Using the DELPHI Detector at LEP

By due permission of the faculty of mathematics and natural sciences of the University of Lund to be publicly discussed at the lecture hall F of the Department of Theoretical Physics, September 30, 1994, at 10.15 a.m., for the degree of Doctor of Philosophy

by

Jonas Bjarne
Department of Physics, University of Lund, Sölvegatan 14, S-223 62 Lund, Sweden

This thesis is based on the following articles, included as **Appendices A** to **E**:

A A Silicon-Tungsten Electromagnetic Calorimeter for LEP,
Nucl. Instr. and Meth. A305(1991)320

B Two-Photon Physics at DELPHI,
Proc. of the International Europhysics Conference on High Energy Physics (HEP93)
and DELPHI 93-127 PHYS 342

C First Evidence of Hard Scattering Processes in Single Tagged $\gamma\gamma$ Collisions,
To be submitted to Phys. Lett. B

D The System for Online Monitoring of LEP Beam Background and Luminosity at the DELPHI Interaction Point, DELPHI 93-3 DAS 137

E VSAT Results of the LEP Beam Separation Scan, DELPHI 90-30 GEN 110 MIG 4

Contents

Abstract

This thesis is based on work done during 1989-1993 using the DELPHI detector at LEP, which is summarised in five articles. It consists of three main parts.

The first part describes the Very Small Angle Tagger (VSAT), which is a sub-detector of the DELPHI detector at LEP. It consists of four silicon-tungsten electromagnetic calorimeter modules having silicon strip planes for position determination. The modules are placed adjacent to the beam pipe, at ± 7.7 m from the interaction point and after superconducting quadrupole magnets, allowing the detection of electrons in a polar angle range of 4 to 13 mrad.

The second part is devoted to two-photon physics at DELPHI, with strong emphasis on a VSAT single-tagged event analysis. Here is shown, for the first time, evidence of hard scattering processes in single tagged two-photon collisions. A QCD Resolved Photon Contribution (QCD-RPC) model is introduced. Data is then seen to be well described by a full VDM+QPM+(QCD-RPC) model. Different parton density functions are compared with data.

The third part first describes the system for online monitoring of LEP beam background and luminosity at the DELPHI interaction point. Details are given of contributing sub-detector signals and program structure. Then follows a description of the VSAT online monitoring program (`VSAT_MONITOR`). A good agreement is found between the `VSAT_MONITOR` estimates of luminosity and beam spot and those of other detectors. Finally, results are presented of VSAT measurements of a LEP beam separation scan.

Preface

This thesis, submitted for the degree of Doctor of Philosophy in Physics, gives a survey of the work I've done for the DELPHI Collaboration as a postgraduate student. Not included are all the dead-ends and mistakes experienced by most students, like me!

The resulting five physics articles are included at the end of the thesis, as Appendix A to Appendix E. They are preceeded by an introductory text containing relevant theory and terminology, as well as extensions and summaries of the papers. The VSAT online monitoring program, not included in any article, is also described.

My first encounter with elementary particle physics was during the summer of 1988, when I, as a CERN Summer Student, worked together with people of the LEP Beam Instrumentation group. My contribution, later resulting in a B.Sc. thesis [1], consisted of participating in program development for and beam tests of the LEP luminosity monitors [2]. I also participated in initial prototype tests of the DELPHI VSAT, modelled after the LEP luminosity monitors, using the same test set-up.

Staying at CERN from early 1989 to late 1991, most of my time was spent setting up and working with the VSAT detector (Appendix A). I concentrated on working with online monitoring in DELPHI (Appendix D) and, in particular, the extraction of monitoring information from the VSAT (Appendix E). My main responsability was writing the VSAT online monitoring program.

Later, staying in Lund, an exciting time was spent working with two Russian visiting scientists and friends, analysing DELPHI two-photon data. With VSAT-tagged data, the first evidence was found for hard scattering processes in single-tagged two-photon collisions (Appendix C). This, together with other DELPHI two-photon results, were reported by me at the HEP 93 conference in Marseille (Appendix B).

Summing up my views of these years, I'd like to quote an Italian Summer Student working for the VSAT group a few years ago:

> *I think I have been very lucky to work inside the VSAT group that maintains a peculiar dimension in search of a singular reality.*

After this, what can I add? I have enjoyed it!!!

Jonas Bjarne
Lund, August 1994

Chapter 1

Apparatus

Below is given a short overview over the apparatus used for this work. LEP and DELPHI are first briefly described, followed by a more detailed description of the VSAT sub-detector.

1.1 The LEP Collider

The **Large Electron-Positron collider (LEP)** is the largest collider ever built. It was designed by engineers and physicists from CERN and built by the European industry. The, at that time, 14 CERN member states contributed the 1300 million Swiss francs required for its construction. Planning started in September 1978, the first electron-positron collisions were produced on August 13, 1989, while the machine was officially inaugurated on November 13, 1989. The LEP collider has been described by several other authors, ranging from popular to more technical papers [3]-[5]. Below will be given only a very short summary of some key LEP parameters.

The LEP tunnel is placed outside of Geneva, on the borderland between Switzerland and France. It is roughly circular with a circumference of almost 27 km. The construction consists of eight straight 500 m sections connected by eight 2800 m arcs. Underground depth varies between 50 and 175 m. The tunnel inside diameter is 3.8 m, except for the four large experimental halls having diameters 23 m and lengths 80 m.

The LEP particle injection scheme is rather complex, using four smaller accelerators and storage rings before injection into LEP. The electrons and positrons are divided into four (later changed to eight) bunches each. Each bunch contains about 10^{11} particles, corresponding to a current of 3 mA per circulating beam. At the interaction points the bunches have strongly elliptical cross-sectional areas of around 210 μm (horisontally) times 8 μm (vertically). Longitudinal length is around 1.1 cm. Maximum LEP luminosity is 1.7×10^{31} cm^{-2}s^{-1}, but normal luminosities seldom exceeded 1×10^{31} cm^{-2}s^{-1} during the 1989-1992 runs.

Particle injection energy is 20 GeV, with further acceleration being performed by LEP. Standard final beam energy is 45.625 GeV, this being optimal for studying the Z^0 resonance at 91.25 GeV. In 1996 LEP will be upgraded to a new phase, called LEP200. Beam energy will then be around 90 GeV to allow detailed studies of the W resonance.

1.2 The DELPHI Detector

One of the four detectors at LEP is **DELPHI, a DEtector with Lepton, Photon and Hadron Identification**. Though DELPHI is a general purpose detector special emphasis is put on powerful particle identification, three-dimensional information with high granularity and precise vertex determination.

The DELPHI detector is shaped like a cylinder with the beam pipe along the cylinder axis (Figure 1.1). It has a radius of 5 m and a length of 10 m. DELPHI is divided into a cylindrical barrel part and two conical end-cap parts. The transition regions, at polar angles 43° and 137°, are partially obscured by cables and connectors. The end-caps can be pulled out from the barrel. A superconducting solenoid is installed at a radius of 2.6 m, providing a uniform magnetic field of 1.2 T along the beam-pipe when an electric current of 5000 A floats through it. DELPHI is installed in a cavern 100 m below ground. Data is sent *via* an optical link to the main computer and control room at ground level.

DELPHI is a complex detector system consisting of around 20 sub-detectors. A brief description will be given below only of those of main interest to this work, *i.e.* charged particle tracking devices and electromagnetic calorimeters. The VSAT is treated in more detail. More information about the DELPHI detector can be found in [6]. Though DELPHI has evolved over the years, with many performance upgrades, the description below is based mainly on this report.

The coordinate system is defined to have the z-axis along the beam pipe. Polar angles θ are given with respect to z, while azimuthal angles ϕ are given starting from the horizontal plane. Radii is denoted by R.

1.2.1 Charged Particle Tracking Devices

The **micro-VerTeX (VTX)** consisted initially of two concentric silicon-strip shells surrounding the beam pipe. They have radii 9 and 11 cm and lengths 24 cm, covering a θ-range of 37° to 143°. Each shell is built of 24 ϕ modules, each module having four z segments. A third silicon-strip shell was later added when the beam-pipe at the DELPHI interaction point was changed to a tube of smaller diameter. Three $R\phi$-points per track are now measured. The intrinsic $R\phi$ resolution is 6 μm.

The **Inner Detector (ID)** [7] consists of two concentric parts. The inner part is a jet chamber having an inner radius of 12 cm, an outer radius of 22 cm and a z-length of 80 cm. This results in a θ-coverage of 17° to 163°. The jet chamber provides 24 $R\phi$-points per track through its 24 ϕ sectors, each having 24 sense wires. A coordinate resolution of 90 μm in the $R\phi$-plane is obtained. The outer part of the ID is a multi-wire proportional chamber (MWPC). Its radial placement is between 23 and 28 cm, length is 50 cm along z and θ-coverage is from 30° to 150°. The MWPC contains five concentric layers, each having 192 wires and circular cathode strips. The wires provide fast trigger information (>95% single track trigger efficiency) while the strips measure z with a resolution of <1 mm.

The main tracking device is a **Time Projection Chamber (TPC)** [8]. It consists of two cylindrical parts placed after each other along the beam pipe. Each part has an active z-length of 134 cm, with inner and outer radii of 35 and 111 cm respectively. θ is measured between 20° and 160°. The two cylindrical parts are

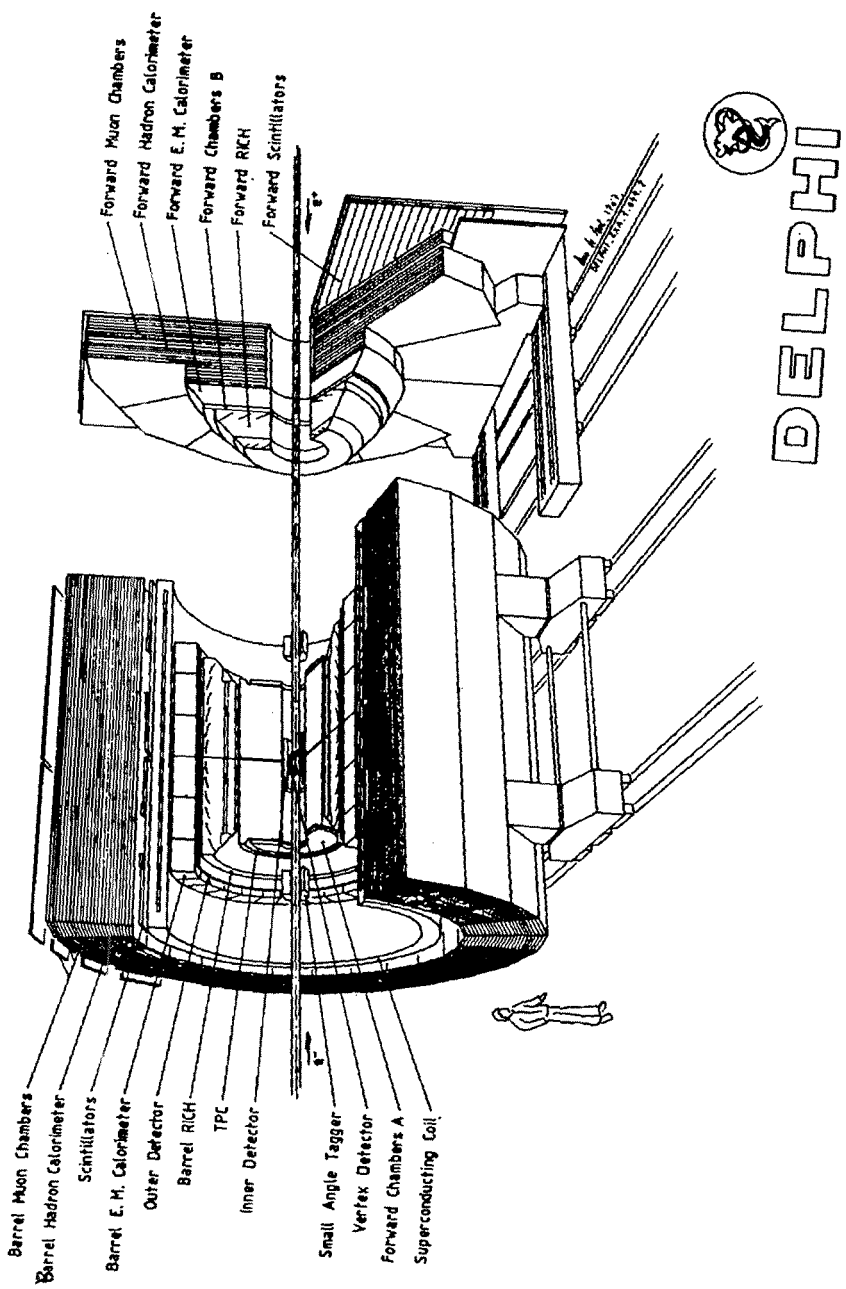

Figure 1.1: The DELPHI detector. The VSAT modules, at $|z| = \pm 7.7$ m, fall outside this figure.

each divided into six sectors in ϕ, each such sector having 16 radial pad rows and 192 sense wires. The pads give 16 points per track in the $R\phi$-plane, resulting in a resolution of 230 μm. A z-resolution of 900 μm is reached through the 192 track points provided by the wires.

The outermost tracking device is the **Outer Detector (OD)** [9], composed of 24 modules in ϕ. Each module is 4.7 m along z, has an inner radius of 198 cm and an outer radius of 206 cm. This leads to a θ-coverage between 43° and 137°. There are five radial layers of drift tubes per module. All the layers measure the $R\phi$-coordinate with a resolution of 110 μm. Three of them also contribute to a z-measurement with a resolution of 4.4 cm.

Each end-cap contains two **Forward Chambers (FCA, FCB)** for tracking in the forward and backward regions (θ from 11° to 35° and 145° to 169° respectively). FCA is the inner one, having R and $|z|$ extensions of 30 to 103 cm and 155 to 165 cm. Each FCA-side contains three double layer half-disc chambers, rotated 120° in ϕ with respect to each other. The layers consist of square cells (15 mm side) with an anode wire in the centre. Six track points are measured by FCA with a total resolution of 150 μm in the $R\phi$-plane. FCB covers R between 53 and 195 cm and $|z|$ between 267 and 283 cm. It also consists of double layer half-disc chambers, but each half-disc is for the FCB divided into six ϕ segments. Each segment consists of 12 pair-wise rotated sense wire planes, having a wire spacing of 2 cm. The 12 track points result in an FCB $R\phi$-resolution of 120 μm.

1.2.2 Electromagnetic Calorimeters

The **Forward ElectroMagnetic Calorimeter (FEMC)** [10]-[12] consists of two modules, one on each end-cap, situated between $|z|$-values of 284 and 340 cm. Each module is in the form of a disk having radial extension from 46 to 240 cm. The θ-acceptance is from 10° to 36.5° for the forward module, and from 143.5° to 170° for the one in the backward direction. A module is built of 4532 lead glass blocks in the form of truncated pyramids. They are arranged to point towards the interaction point. Each pyramid is 20 radiation lengths deep and has a granularity of one degree in both θ and ϕ. Read-out is *via* vacuum phototriodes. FEMC has a 4% energy resolution at a beam energy of 45.6 GeV.

The **Small Angle Tagger (SAT)** [13] also consists of two end-cap modules. They are placed longitudinally between $|z|$=233 and 285 cm, and radially between 10 and 36 cm. The SAT modules cover a θ-range of 2.5° to 7.7° (172.3° to 17.5°) in the forward (backward) direction. Each calorimeter module is built from alternating lead sheets and plastic scintillating fibres, which are aligned parallel to the beam-pipe. Read-out is *via* lightguides and photodiodes, segmented in the $R\phi$-plane to have a granularity in ϕ of 7.5° (15°) for the inner (outer) four radial rings, while θ-granularity is 0.7°. The 28 radiation lengths deep modules have energy resolutions of 1.6% at a beam energy of 45.6 GeV. For the 1994 runs the SAT was replaced by a **Small angle TIle Calorimeter (STIC)** [14, 15].

1.2.2.1 The VSAT Sub-Detector

The **Very Small Angle Tagger (VSAT)** is described in detail in Appendix A.

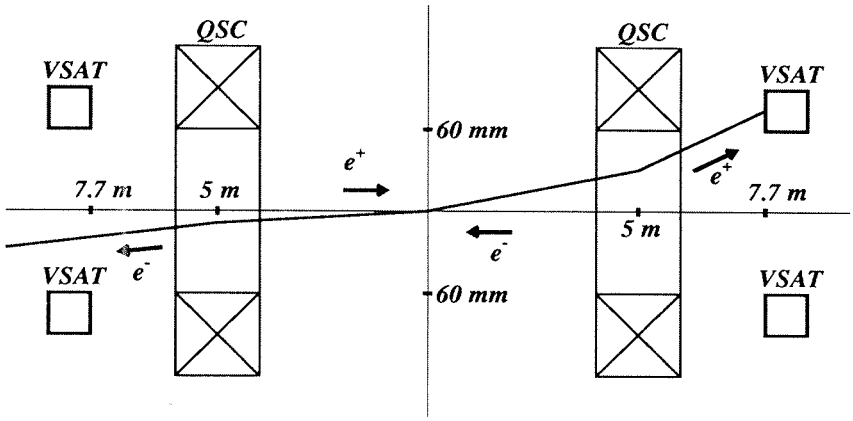

Figure 1.2: Picture (not to scale) of the LEP beam transport around the DELPHI interaction point. The four VSAT modules are placed symmetrically at ± 7.7 m from the interaction point, and on both the inner and outer sides of the LEP ring. The trajectories of charged particles are bent in the superconducting quadrupole magnets (QSC) in front of the VSAT modules.

Here only a summary will be given of some main VSAT features, together with a few extensions and figures to complement the reading of Appendix A.

The VSAT consists of four electromagnetic calorimeter modules placed at ± 7.7 m from the interaction point, *i.e.* after the superconducting quadrupole magnets (QSC) as shown in Figure 1.2. The modules are placed horisontally around short elliptical sections of the beam pipe, with one module on each side of it (left picture in Figure 1.3).

The QSC's in front of the VSAT modules, focusing outgoing charged particles in the vertical direction and defocusing them in the horisontal direction, distorts the VSAT (θ,ϕ)-acceptance. The VSAT acceptance above 20 GeV has a usable θ-range from 4 to 13 mrad. The ϕ-coverage, while about $\pm 45°$ around the horisontal axis per module at nominal beam energy, increases for lower energies due the QSC focusing.

Each VSAT calorimeter module contains 12 two radiation lengths thick tungsten absorbers, stacked with 12 silicon detector planes for energy measurements (right picture in Figure 1.3). The overall active size for each calorimeter stack is 3 cm horisontally and 5 cm vertically with a depth of 10 cm (24 radiation lengths). However, due to the beam pipe flanges in front of the VSAT modules, the area illuminated by particles is only 1.5 cm horisontally. The resulting energy resolution for transversely contained showers is $35\%/\sqrt{E}$, *i.e.* $\sim 5\%$ at nominal beam energy.

Horisontal and vertical electromagnetic shower coordinates are measured by three silicon strip planes (1 mm pitch) placed at 5, 7 and 9 radiation lengths into each stack, this being close to the shower maxima. Two strip planes measure x-coordinates and one y-coordinate. Strip information is used to eliminate showers being too close to a calorimeter edge, as well as to correct for transversal shower

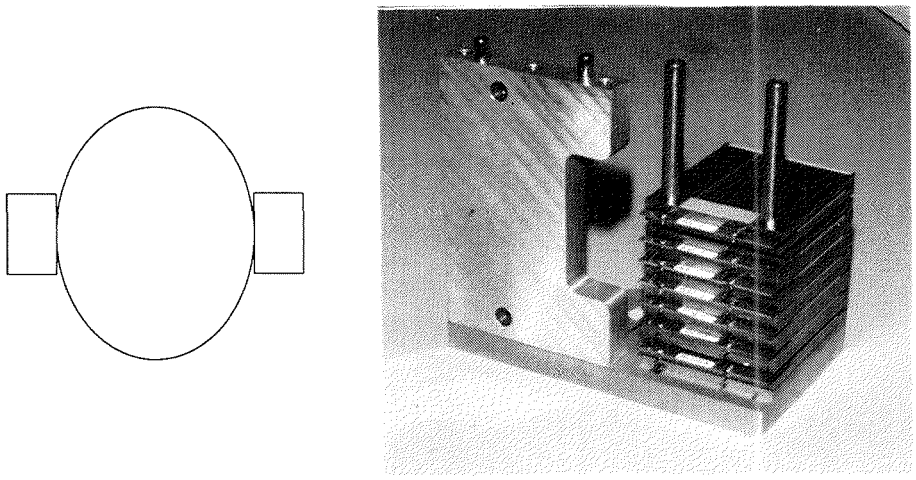

Figure 1.3: Transversal view of the beam pipe, showing the placement of two VSAT modules around an elliptical beam pipe section (left picture). Photo of a dismounted VSAT calorimeter module, showing the stacking of silicon detector planes and tungsten energy absorbers (right picture).

leakage. The reconstructed position resolution is about 200 μm.

The VSAT provides three kinds of triggers:

- A Bhabha event is defined as the coincidence between diagonal modules, each module detecting at least an energy of 20 GeV.
- Bremsstrahlung off-momentum beam particles, called Single Electrons, are recorded by a downscaled trigger also having a 20 GeV threshold.
- Accidental diagonal coincidences, called False Bhabhas, are recorded by a trigger requiring a Single Electron in an inner module and another one in its diagonal (outside) module N bunches later (N=the number of LEP bunches).

Any VSAT event is accompanied by trigger information to DELPHI . This information can be used by other DELPHI subtriggers for trigger decisions.

Since the VSAT trigger rate is higher than the DELPHI trigger rate, VSAT events are accumulated in a local event buffer which is read out at each DELPHI event. A DELPHI event is forced by VSAT when the event buffer is full, which rarely happens.

Chapter 2

Two-Photon Physics

Classical electromagnetic theory only allows the superposition of two crossing electromagnetic waves, but no interaction between them. Photon-photon interactions are instead allowed by modern quantum electrodynamic theory (QED). However, the probability for these interactions is extremely small at low energies, preventing two-photon interactions to be observed with even the strongest of photon beams, like lasers. These interactions have instead been studied using colliding electron and positron beams. By QED radiative quantum effects the electrons and positrons are surrounded by clouds of virtual photons. The circulating e^+e^- beams of a collider can thus be seen to be the sources of two strong photon beams.

These photon beams have some special properties. The resulting photon luminosities are normally quite high, only about a magnitude smaller than the e^+e^- luminosities. As the cross-section for two-photon scattering increases with beam energy E ($\sim \log^2(E/m_e)$), high-energy colliders are ideal machines for two-photon studies. The photons are radiated according to a Bremsstrahlung-like spectrum (probability $\sim 1/E_\gamma$), and mainly into small angles ($\sim m_e/E$) relative to the beams. This leads to a dominance of two-photon events having low invariant masses W. Since normally the two radiated photons have different energies, most two-photon event axes are strongly boosted along the e^+e^- beam direction. Here particles are more difficult to detect, making the visible (*i.e.* detected) cross-section appreciably smaller than the true (*i.e.* total) cross-section. Note that the energy spectra of the photons allow different values of W to be measured, while the e^+e^- kinematics which is fixed by the e^+e^- beam energy.

Two-photon studies have been performed by many e^+e^- experiments, *e.g.* at DESY by PLUTO [16], at SLAC by TPC/2γ [17] and at KEK by AMY [18]. Recently, two-photon results have also been presented by all the four LEP experiments (ALEPH [19], DELPHI, L3 [20] and OPAL [21]).

The two-photon results obtained with the DELPHI detector are described below, with emphasis on the analysis of VSAT-tagged events. This is preceeded by a short introductory theoretical background to the field of two-photon physics.

2.1 Theoretical Background

Below is given a very brief introduction to two-photon theory, discussing competing processes before concentrating on two-photon kinematics, tagging and models.

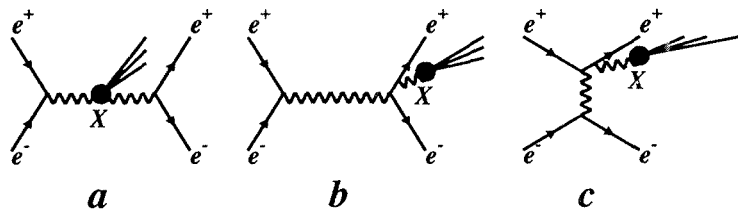

Figure 2.1: Feynman diagrams of (a) the γ cascade process, (b) the virtual Bremsstrahlung process with e^+e^- annihilation and (c) the virtual Bremsstrahlung process with e^+e^- scattering.

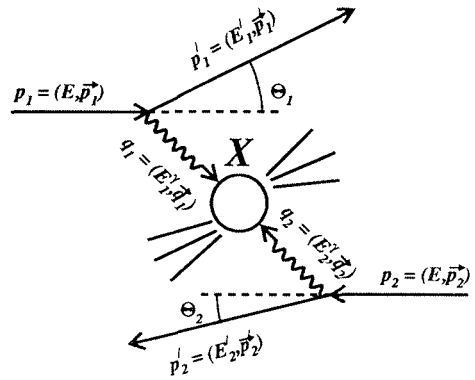

Figure 2.2: Kinematics of the two-photon process.

More detailed descriptions can be found in Appendix C as well as in several other papers [22]-[27].

2.1.1 Processes

Inelastic electron-positron processes ($e^+e^- \rightarrow e^+e^- + X$, where X is a particle system) can be classified as

- γ cascade processes
- virtual Bremsstrahlung processes with e^+e^- annihilation
- virtual Bremsstrahlung processes with e^+e^- scattering
- two-photon processes

Feynman diagrams over these processes are shown in Figure 2.1 and Figure 2.2. In each of these diagrams a photon propagator can be replaced by a Z^0 particle. However, due to the very high mass of the Z^0 boson ($m_{Z^0} \approx 91$ GeV), the diagrams

with Z^0 propagators are heavily suppressed and will not be considered further in this thesis.

The amplitudes of the diagrams depend on the propagation factors $1/q_i^2$, where q_i is the momentum transfer of propagator i. The diagrams of Figs. 2.1.1a and 2.1.1b are one-propagator e^+e^- annihilation diagrams, with $q = \sqrt{s} = 2E_{beam}$ for a collider. At the high beam energies of LEP ($E_{beam} \approx 46$ GeV) the amplitudes of these diagrams are negligible. The one-propagator diagram of Fig. 2.1.1c has the propagation factor $1/q^2$, while the two-propagator diagram of Fig. 2.1.1 has a total factor of $1/q_1^2 \cdot 1/q_2^2$. In this thesis will be considered the case with very small momentum transfers q, leading to a dominance of the latter diagram. It is thus seen that the two-photon diagram of Fig. 2.1.1 is the dominant diagram at the beam energies and momentum transfers of concern for this work.

2.1.2 Kinematics

The momentum transfer Q_i^2 in each lepton-photon vertex i in the two-photon reaction can be calculated as (see Fig. 2.1.1)

$$-Q_i^2 = q_i^2 = (p_i - p_i')^2 = 2m_e^2 - 2EE_i'(1 - \sqrt{1-(m_e/E)^2} \cdot \sqrt{1-(m_e/E_i')^2} \cdot \cos\theta_i), \tag{2.1}$$

which, for $\theta_i \gg m_e/E$, can be approximated by

$$-Q_i^2 = q_i^2 \approx -4EE_i' \sin^2(\theta_i/2) \tag{2.2}$$

At LEP $m_e/E \approx 10^{-5}$. This is indeed much smaller than the polar angles θ_i in which it is possible to detect the scattered leptons at DELPHI, meaning that (2.2) is applicable.

With $E_i^\gamma = E - E_i'$ the invariant mass W of the produced particle system X is given by

$$W^2 = (q_1 + q_2)^2 = 4E_1^\gamma E_2^\gamma - 2E_1'E_2'(1 - \cos\theta_1\cos\theta_2 - \sin\theta_1\sin\theta_2\cos\Phi) \tag{2.3}$$

Here Φ is the angle between the two planes defined by the two scattered leptons and the beam axis. Since we will here only treat the case with very low momentum transfer scattering, equation (2.3) can be simplified to

$$W^2 \approx 4E_1^\gamma E_2^\gamma \tag{2.4}$$

2.1.3 Tagging

Experimentally one can detect the energy and angles of both, one or none of the leptons scattered from the two-photon reaction. This is called "tagging" the interacting photons. One differentiates between the four cases of double-tagging, single-tagging, no-tagging and anti-tagging. Tagging is normally done by detectors placed in the forward regions, typically covering $\theta < 100$ mrad.

2.1.3.1 Double-tagging

In this case, knowing both photon four-vectors, the full reaction kinematics is available for precise cross-section studies *etc.* Double-tagging also ensures a complete dominance of the two-photon diagram over competing diagrams. However, experimental limits on the W resolution severely limit the obtainable accuracy. An unfolding procedure is often required to link the visible W to the true W. Due to the strong forward peaking of the scattered leptons, tagging needs to be done at very small angles. Here high-rate background sources, such as small angle Bhabha scattering, can be difficult to reject. The experimentally visible cross-section for double-tagged two-photon events is very small.

2.1.3.2 Single-tagging

Detecting either the scattered electron or the positron is necessary for studying the Q^2 dependence of, for example, the photon structure function F_2^γ. The Q^2 of the virtual photon, which probes the target photon structure, is given by the measurement of the tagged lepton. Large Q^2-values are required to enter into the deep inelastic scattering range, implying rather large scattering angles ($\theta_{tag} > 100$ mrad). Here the cross-section is comparatively small due to the forward peaking of the leptons. Moving to the low-Q^2 range ($\theta_{tag} < 30$ mrad) the event rate goes up, and one can, by analysing relatively high-$W_{\gamma\gamma}$ events, study the production and properties of jets with high transverse momenta p_T. The measured energy spectrum of the leptons can be useful in this analysis. Resonance formation studies can also be carried out with single-tagged two-photon events. Detecting a scattered lepton is useful for reducing different background sources, like e^+e^- annihilation processes. One has to make sure that the non-detected electron is not scattered into large angles (*i.e.* large Q^2), as the virtual Bremsstrahlung process with e^+e^- scattering (Fig. 3.1c) will then dominate. Experimentally visible cross-sections for single-tagged two-photon events, though dependent on Q^2, are typically at least 10 times larger than for the double-tagged case.

2.1.3.3 No-tagging

Not detecting any of the scattered leptons, the only information available is that of the produced particle system X. However, two-photon reactions generally involve small momentum transfers Q^2, implying also comparatively low W. Also the no-tagged events can be used for studying low-p_T jets, resonances *etc.* The two-photon process is dominant at low W, reducing the background contamination from other processes such as the one-photon reaction $e^+e^- \rightarrow X$. It is also necessary to require low-Q^2 scattering in order to ensure this dominance; only accepting events with small total p_T ensures a sample being completely reconstructed. Not requiring any tagging greatly increases the visible cross-section, this being at least a factor 100 larger than for the double-tagged case.

2.1.3.4 Anti-tagging

It is shown above that in order to ensure the dominance of the two-photon

process, it is necessary for the single-tagged and no-tagged cases to require the untagged leptons to have small scattering angles. This can be done by an anti-tagging requirement, where an event is rejected if two leptons (one for the no-tagged case) are detected. Having a detector in the very forward direction thus assures very low Q^2 for the untagged leptons.

2.1.4 Cross-Sections

Two-photon cross-section calculations are in general quite lengthy and complicated. Using some approximations, the cross-section $\sigma_{\mu\mu}$ for $e^+e^- \rightarrow e^+e^-\mu^+\mu^-$ is, however, seen to be a managable and instructive case [28]. The QPM model, discussed later, is based on calculations analogous to what will be described below. The $\mu^+\mu^-$ production is given by the QPM-diagram of Figure 2.3.b, where $q\bar{q}$ should be replaced by $\mu^+\mu^-$. This diagram can be divided into two parts, the first one describing $e^+e^- \rightarrow \gamma\gamma$ and the second $\gamma\gamma \rightarrow X \rightarrow \mu^+\mu^-$. Only the no-tag case is treated here.

The Bremsstrahlung spectrum of the beam-radiated photons can be approximated by the Weizsäcker-Williams formula, with $\omega = E^\gamma/E$ and $\alpha \approx 1/137$

$$\frac{dN}{d\omega} = \frac{\alpha}{2\pi}\frac{1+(1-\omega)^2}{\omega}\ln\left(\frac{E^2}{m_e^2}\right) \tag{2.5}$$

The convoluted photon spectra at some W define a two-photon luminosity function $L_{\gamma\gamma}$. Its dependence on the energy fraction $\tilde{s} = W/\sqrt{s} = W/2E$ is given by

$$\frac{dL_{\gamma\gamma}}{d\tilde{s}} = \left(\frac{\alpha}{\pi}\right)^2\frac{f(\tilde{s})}{\tilde{s}}\ln^2\left(\frac{E^2}{m_e^2}\right) \tag{2.6}$$

with

$$f(\tilde{s}) = (2+\tilde{s}^2)^2\ln\left(\frac{1}{\tilde{s}}\right) - (1-\tilde{s}^2)(3+\tilde{s}^2) \tag{2.7}$$

This approximation describes the shape of $L_{\gamma\gamma}$ well, but overestimates its value by around 10% for $\tilde{s} < 0.8$.

By finally convoluting $L_{\gamma\gamma}$ with the approximated cross-section $\sigma_{\gamma\gamma} = 4\pi\alpha^2/W^2$ for $\gamma\gamma \rightarrow X \rightarrow \mu^+\mu^-$, the total cross-section $\sigma_{\mu\mu}$ becomes

$$\sigma_{\mu\mu} = \int L_{\gamma\gamma}\,\sigma_{\gamma\gamma}\,d\tilde{s} = \frac{8\alpha^4}{\pi}\frac{1}{m_\mu^2}\ln^2\left(\frac{E}{m_e}\right)\ln\left(\frac{E}{m_\mu}\right) \tag{2.8}$$

Notice the $\ln E$ dependence of $\sigma_{\mu\mu}$, showing the increasing two-photon cross-section with energy.

2.1.5 Models

The photon is a complex object to describe, as it shows several different characteristics. Results from some experiments (photoproduction, electromagnetic form factors *etc.*) show the characteristics of soft hadron interactions. Other experiments (*e.g.* high energy e^+e^- annihilation) show a direct coupling to pointlike quarks inside the hadrons. The first characteristic is described by the VDM model, while the

second is described by the QPM model. Until recently, a composite VDM+QPM model was able to explain all two-photon data. However, several experiments ([29]-[31]) have reported high-p_T event excesses which can not be explained inside this model. A third component, the QCD-based hard scattering model, has therefore been added to better describe the data. The latter model requires specific parton density functions to calculate parton momenta fractions. Below is given a very brief overview over these models.

2.1.5.1 The VDM Model

The non-perturbative, phenomenological **Vector meson Dominance Model (VDM)** (Figure 2.3.a) is well-known from hadron-hadron interaction physics. To describe the interaction between a photon and hadrons, VDM assumes the photon to convert into vector mesons. These then interact with hadrons through the strong force. VDM thus predicts photon-photon scattering to have the characteristics observed for hadron-hadron scattering. VDM is only applicable for small transverse momenta p_T, where the lifetime of the quark-antiquark pair is long enough for them to interact *via* gluon exchange to form bound vector meson states. The main contribution to the total two-photon cross-section comes from VDM processes.

The VDM cross-section is given by [32] as

$$\sigma_{\gamma\gamma}^{VDM}(Q_1^2, Q_2^2, W^2) = F_{VDM}(Q_1^2) F_{VDM}(Q_2^2) \left[A + \frac{B}{W} \right] \tag{2.9}$$

The last term, in brackets, describes the W-dependence of $\sigma_{\gamma\gamma}$. The underlying theory here is the Regge model, resulting in a W-behaviour of $W^{2\alpha-2}$ [33]. Treating only the terms with α=1/2, 1 and 2 as significant to $\sigma_{\gamma\gamma}$, a comparison with measured cross-sections results in A = 275 nb and B = 300 nb·GeV [34]. These values were used for this work as they have been found by previous experiments [16, 18].

The first two terms describe how $\sigma_{\gamma\gamma}$ varies with momentum transfers Q_i^2. The quantity F_{VDM} is the VDM form factor. However, F_{VDM} is here taken from the **Generalised VDM model (GVDM)** since this model also takes into account effects from the higher mass resonances and the continuum. It is given by [35] as

$$F_{VDM}(Q^2) = \sum_{V=\rho,\omega,\phi} r_V \frac{1 + Q^2/4m_V^2}{(1 + Q^2/m_V^2)^2} + \frac{0.22}{1 + Q^2/m_0^2} \tag{2.10}$$

Here m_0 = 1.4 GeV and m_V denotes the mass of vector meson V. The factors r_V are related to the coupling between vector meson V and the photon. The following r_V-values were used [27]: r_ρ=0.65, r_ω=0.08 and r_ϕ=0.05.

$\sigma_{\gamma\gamma}^{VDM}$ varies with p_T^2 as

$$\frac{d\sigma_{\gamma\gamma}^{VDM}}{dp_T^2} \sim \frac{1}{e^{\alpha p_T}} \tag{2.11}$$

This exponential behaviour leads to a suppression of high-p_T VDM events.

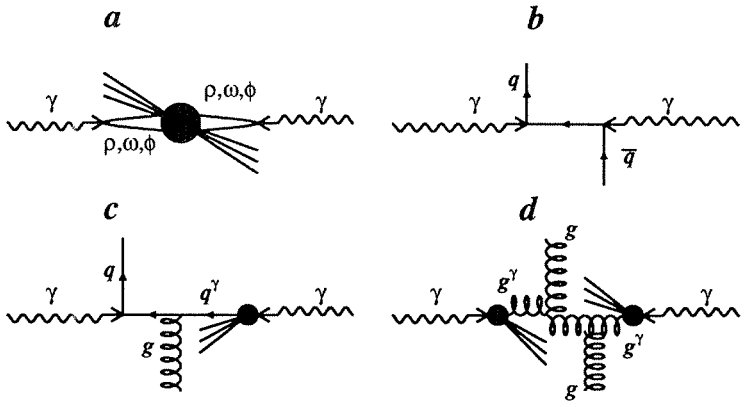

Figure 2.3: Diagrams which are contributing in lowest order to the two-photon multi-hadronic system X. (a) VDM contribution, (b) QPM contribution, (c) and (d) examples of singly and doubly resolved QCD-RPC contributions.

2.1.5.2 The QPM Model

From other experiments it is known that photons can exhibit pointlike coupling directly to a quark-antiquark pair ($e^+e^- \rightarrow e^+e^- + q\bar{q}$), which subsequently fragments into hadrons. The resulting events show typical two-jet topologies. This lowest order Born procedure is modelled by the perturbative **Quark Parton Model (QPM)** (Figure 2.3.b). Contrary to VDM, QPM is only applicable at large Q^2 or high quark p_T. In these regions the interaction times are too short for the formation of bound states. The dominant scale for the QPM model is p_T^2, meaning that $p_T^2 > Q^2$ for the QPM case.

The QPM contribution $\sigma_{\gamma\gamma}^{QPM}$ to the total cross-section is in general comparatively small at the relatively low Q^2 of most two-photon events. However, at large Q^2 the influence of the QPM process becomes significant. A full calculation of $\sigma_{\gamma\gamma}^{QPM}$ for hadron production is rather complicated, involving the sum of several terms [27]. Refer to the sub-chapter on Cross-Sections above for further details. The QPM W dependence in lowest order is found to follow

$$\sigma_{\gamma\gamma}^{QPM} \sim \frac{1}{W^2} \tag{2.12}$$

while the p_T^2 dependence is given by

$$\frac{d\sigma_{\gamma\gamma}^{QPM}}{dp_T^2} \sim \frac{1}{p_T^4} \tag{2.13}$$

By comparing (2.11) and (2.13), it is seen that the QPM hard scattering processes become dominant above around p_T >1 GeV. This p_T limit and the involved energies are quite small compared to other reactions. Two-photon events thus allow clean, low-energetic studies of hard scattering processes.

2.1.5.3 The QCD-RPC Model

Apart from the QPM model, generating two-jet events, other hard scattering multi-jet diagrams are possible. For the case $p_T^2 > Q^2$, where Q^2 is very small, these diagrams start to dominate. Their contributions are described by the **QCD Resolved Photon Contribution (QCD-RPC)** model. Two cases are possible: single resolved (Figure 2.3.c) and double resolved (Figure 2.3.d) diagrams. By resolved is meant that one, or both, of the photons are resolved into its (their) hadronic constituents. The resulting particles produce (together with the normal two jets) so-called remnant jets. The QCD-RPC model thus generates three-jet and four-jet events. However, the remnant jets are mainly produced at very small angles relative to the beams, making them difficult to detect. The bulk of the visible QCD-RPC events will therefore be seen to have a similar high-p_T two-jet topology as the QPM events.

The single resolved QCD-RPC contribution contains two sub-processes, $\gamma g \rightarrow q\bar{q}$ and $\gamma q \rightarrow gq$, while the double resolved one contains eight $(q, \bar{q}, g)$ sub-processes. Here g means a gluon, while q ($\bar{q}$) is a quark (antiquark). These sub-processes allow experimental tests of the theoretical predictions for the photon quark and gluon densities.

Important ingredients in cross-section calculations involving incoming particle hadronic structures, such as the QCD-RPC model, are the **Parton Density Functions (PDF)**. The variable X is here defined as the fraction of the total hadron longitudinal momentum carried by a given parton (q, $\bar{q}$ or g). The PDF's give, for each parton, the parton density for a given (X,Q^2)-value, where Q^2 is the momentum transfer. This is needed in perturbative QCD calculations as they solve the Altarelli-Parisi equations to describe the Q^2 dependence of the parton densities.

There are several different PDF sets available, though some of them are not applicable for two-photon studies since they are derived from deep inelastic $e\gamma$ experiments at high Q^2. Experimental results are needed to differentiate between the PDF's. A free parameter for each PDF is its p_T^{min}-value, *i.e.* the minimum transverse momentum required for the associated QCD-RPC process to take place. Since these processes are perturbative, such a p_T-cut is required to stay above the non-perturbative VDM region to avoid event double-counting. The p_T^{min}-values are constrained by the visible cross-sections. Normal values vary between 1.5 and 3.0 GeV, depending on the actual PDF set. The PDF's are finally compared by studying key physical distributions (*e.g.* W, p_T^{jet} *etc*).

The cross-section calculations for the single and double resolved QCD-RPC processes are seen above to be dependent on the PDF. The resulting calculations are outside the scope of this work; an overview over the calculations for some different PDF sets is given by [27]. Asymptotically, the QCD-RPC cross-section is found to have a similar p_T^{-4}-behavour as for the QPM case (2.13).

2.2 Two-Photon Physics at DELPHI

Two-photon physics at DELPHI have, so far, been studied in the single-tagged and no-tagged modes. Double-tagged event studies will also be performed once the LEP integrated luminosity is large enough for having a significant data sample.

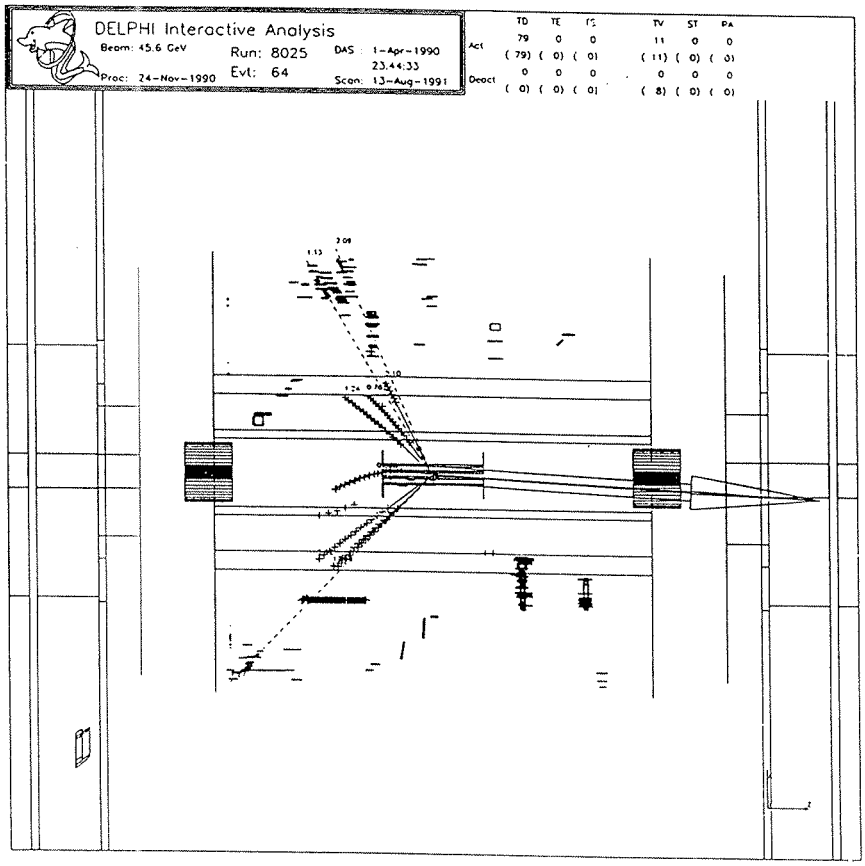

Figure 2.4: Longitudinal event display of a two-photon event as seen by the DELPHI detector. The arrow represents the calculated missing momentum.

DELPHI allows two-photon tagging inside a large Q^2-range through its three forward electromagnetic calorimeters. Different aspects of the photon can therefore be studied. High-Q^2 events are used for testing deep inelastic scattering theory, while perturbative QCD resolved photon processes can be studied by low-Q^2 events. At DELPHI, the latter can be studied both in the single-tagged and no-tagged modes. Different DELPHI tagging parameters are given in the table below. Figure 2.4 show a longitudinal event display of a two-photon event as seen by DELPHI [27].

Main parameters for the different DELPHI two-photon tagging cases.

Tagger	θ [mrad]	$< Q^2 >$ [GeV^2]	$\int\mathcal{L}$ [pb^{-1}]	#ev.	σ [pb]	Backgr. [%]
FEMC	175 - 637	80	61	100	1.7	7
SAT	43 - 135	12	26	300	12	5
VSAT	5 - 13	0.06	28	500	17	4
(no tag)	<43	0.12	32	18000	570	3

The table illustrates clearly how the two-photon cross-section increases for low Q^2. The different integrated luminosities ($\int\mathcal{L}$) reflect which data have been included in the corresponding analyses (FEMC: 1991-93, SAT and VSAT: 1991-92, no-tag: 1990-92). Reasonably low background levels are also seen, independently of tagging case. The no-tag events are anti-tagged by SAT and FEMC, but not by VSAT. This results in VSAT-tagged events, which lie inside a very narrow Q^2-range, having a smaller $< Q^2 >$ than no-tagged events.

An overview over two-photon physics at DELPHI is given in Appendix B. Below will first be given a very brief description over the results obtained from FEMC- and SAT-tagged data, after which follows a more detailed discussion of two-photon physics with VSAT-tagged data. This is also described in Appendix C. Finally follows a short section on the results of the no-tag analysis.

2.2.1 Results of FEMC- and SAT-Tagged Data Analyses

For the FEMC- and SAT-tagged cases, having rather large $< Q^2 >$ of 80 and 12 GeV^2 respectively, the two-photon process can be viewed as deep inelastic scattering of electrons off quasi-real photons. This approach assumes the non-tagged photons to have negligible momentum transfers, which is assured by anti-tagging requirements. Simulation studies showed these momentum transfers to have an average value of around 0.1 GeV^2 for the SAT-tagged case.

A VDM+QPM model was found [36, 37] to fully describe the data for both the FEMC- and SAT-tagged cases. In the description of the QPM model, it was stated that the relative weight of QPM increases with $< Q^2 >$. A simulation study of $R = \sigma_{QPM}/(\sigma_{VDM} + \sigma_{QPM})$ illustrates this, SAT here having $R = 58\%$ and FEMC $R = 81\%$. This should be compared to QPM influences of around 10% for the low-Q^2 cases.

Work is currently in progress to unfold the FEMC- and SAT-tagged data to be able to study the photon structure function F_2^γ.

2.2.2 Results of VSAT-Tagged Data Analyses

Results of VSAT-tagged two-photon data analyses have been reported at the HEP 93 conference ([38] and Appendix B) and in a forthcoming *Physics Letters B* article (Appendix C). The latter gives a detailed description of the simulation methods, event selection cuts, background rejection procedures *etc* that were used for analysing the VSAT-tagged events. This will not be repeated here, emphasis instead being put on a rather thorough discussion of the main results available so far. Appendix C should therefore be read in conjunction with the text below to obtain a complete picture of the VSAT-tagged two-photon data analyses.

Comparing the VDM+QPM model with VSAT-tagged data reveals the simulated cross-section to be too small to explain the data. The shapes of relevant physics histograms are also seen to differ from the data distributions. However, there is a large theoretical uncertainty in the calculation of the VDM cross-section. A study was carried out to investigate if increasing the VDM cross-section would result in a better agreement with data.

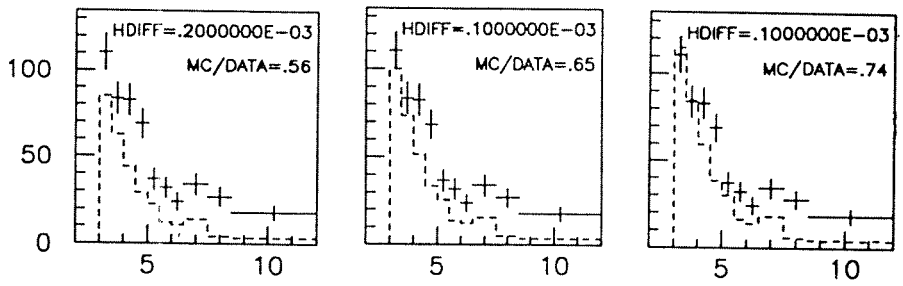

Figure 2.5: Three histograms showing comparisons between the number of events in VSAT-tagged data and the VDM+QPM model *vs.* $W_{visible}$ [GeV]. The VDM cross-sections are multiplied by 1.0, 1.2 and 1.4 respectively.

Figure 2.5 shows three histograms over number of events *vs.* $W_{visible}$ [GeV]. The VDM+QPM predicitions are represented by hatched lines while the data are shown with error bars. Below each histogram is indicated the relevant VDM cross-section multipliers, increases of 0%, 20% and 40% being tested here. The MC/DATA ratios compare simulated and data cross-sections by dividing the corresponding number of events. Without any VDM increase only 56% of the data cross-section is reproduced by the VDM+QPM model, while even a rather large (40%) VDM increase leads to the data having 26% more events than the model.

The shapes of the VDM+QPM and data distributions of Figure 2.5 were compared using the HDIFF statistical test algorithm included in the HBOOK program package [39]. A Kolmogorov test [40] is performed on the distributions, resulting in a returned HDIFF value between zero and one. The higher the value, the higher the compatibility between the tested distributions. Very low HDIFF values are shown in Figure 2.5, confirming the visibly large differences between the VDM+QPM and data distributions independently of VDM cross-section multiplier. Comparing the first and last histograms, the larger VDM cross-section is seen to result mainly in more low-$W_{visible}$ events as given by equation (2.9). The VDM+QPM model is

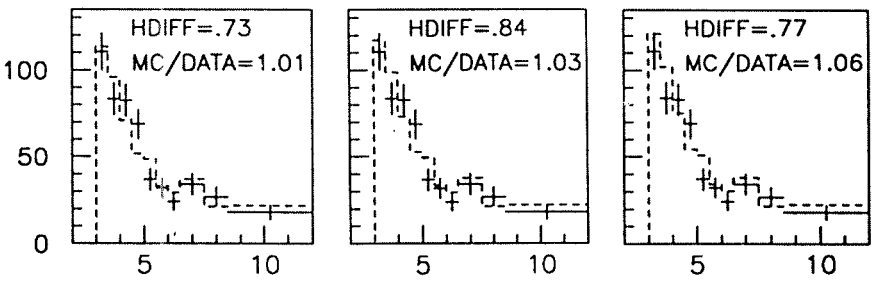

Figure 2.6: Three histograms showing comparisons between the number of events in VSAT-tagged data and a full VDM+QPM+(QCD-RPC) model *vs.* $W_{visible}$ [GeV]. The VDM cross-sections are multiplied by 1.0, 1.05 and 1.1 respectively.

thus seen to be inadequate, even when appreciable VDM cross-section increases are applied.

Figure 2.6 also shows three $W_{visible}$ histograms, but with a QCD-RPC component being added (*i.e.* the full VDM+QPM+(QCD-RPC) model). The included QCD-RPC parton density function is here the one according to M. Drees and K. Grassie (DG) [41], with p_T^{min}=1.45 GeV. Subsequent tuning of p_T^{min} have resulted in an optimum value of 1.56 GeV for DG. The VDM cross-section multipliers in this figure corresponds to increases of 0%, 5% and 10%. All three histograms are now seen to be compatible with the data, a 5% VDM cross-section increase leading to the best result with MC/DATA=1.03 (*i.e.* 3% too many simulated events) and HDIFF=0.84. The inclusion of the QCD-RPC model is thus seen to strongly improve the description of the experimental data.

Many histograms over VSAT-tagged data are given by Appendix C, but in addition Figure 2.7 and Figure 2.8 contain some of the main results obtained. These histograms were presented at the HEP 93 conference (Appendix B). Individual model behaviours are included in the first three histograms, with QCD-RPC abbreviated to QCD. The included parton density function is also here DG for all histograms, again with a p_T^{min}-value of 1.45 GeV.

The upper histogram of Figure 2.7 shows the number of charged tracks *vs.* inclusive charged p_T^2. The VDM part, though large at low p_T^2, is seen to diminish rapidly with increasing p_T^2 and is negligible above p_T^2=2 GeV^2. The QPM model is about an order of magnitude smaller at low p_T^2, but the comparatively weak decrease with increasing p_T^2 makes QPM dominate over VDM at large p_T^2. However, the summed VDM+QPM model is seen to fail to describe the data. The large deficit of simulated tracks at low p_T^2 corresponds to a too low model cross section, while the too strong VDM+QPM decrease for larger p_T^2 do not follow the shape of the data. The QCD-RPC contribution is seen to be of approximately the same magnitude as the VDM model at low p_T^2, but has a more gentle decrease for larger p_T^2. It is instructive to compare the relative p_T^2 behaviours of these models to the $d\sigma_{\gamma\gamma}/dp_T^2$ relations given in the chapter on Theoretical Background. Finally, including also the QCD-RPC contribution into a full VDM+QPM+(QCD-RPC) model, data is seen to be well-described both concerning cross section and overall p_T^2-dependence.

The $W_{visible}$ spectrum is shown in the lower histogram of Figure 2.7. The VDM+QPM model is again seen to have difficulties describing the data, a too small cross section and a lack of events above $W_{visible}$=8 GeV being apparent. Adding also the QCD-RPC model results in a good agreement with data. Notice how QCD-RPC processes become dominant for $W_{visible}$ >5 GeV.

Figure 2.8 (upper histogram) shows the distribution of the beam-normalised tag energy E_{tag}/E_{beam}, with E_{tag} measured by the VSAT. Data is again seen to require the full three-component model. This histogram being drawn in a linear scale, the relative contributions of the different models can be estimated from the areas under their corresponding curves. As expected for low-Q^2 data, the contribution from the QPM process is quite small (~10%). The VDM and QCD-RPC contributions are seen to be approximately equal in magnitude. While the peak around E_{tag}/E_{beam}=0.9 is due mainly to VDM contributions, QCD-RPC processes are seen to dominate for E_{tag}/E_{beam} <0.8

Observing the above QCD-RPC dominated regions, the lower plot of Figure 2.8

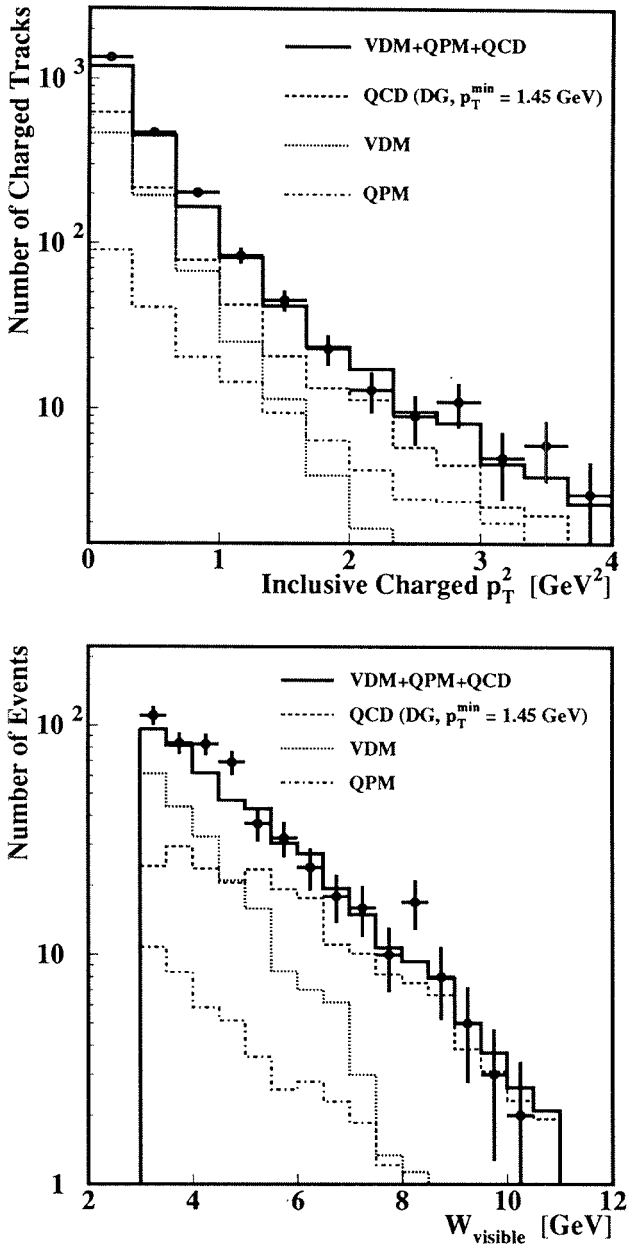

Figure 2.7: Both histograms show comparisons between VSAT-tagged data and a full VDM+QPM+(QCD-RPC) model. Individual model behaviours are also indicated. The upper histogram shows inclusive charged p_T^2, while the lower one shows $W_{visible}$.

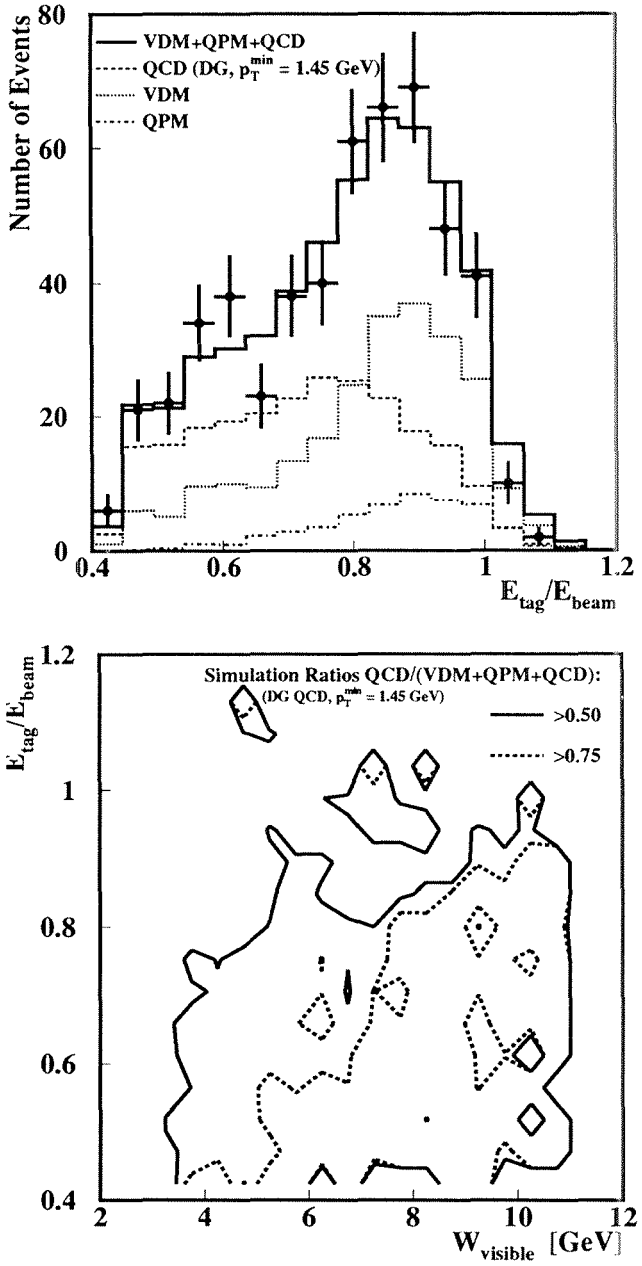

Figure 2.8: The upper histogram shows a comparison between VSAT-tagged data and a full VDM+QPM+(QCD-RPC) model for E_{tag}/E_{beam}. Individual model behaviours are also indicated. The lower histogram shows, for simulated VSAT-tagged data, the influence of the QCD-RPC component in the E_{tag}/E_{beam} *vs.* $W_{visible}$ plane. QCD-RPC contributions of 50% and 75% are indicated.

is a two-dimensional contour histogram of E_{tag}/E_{beam} *vs.* $W_{visible}$. Only simulated data are used in this figure. The bins are filled with the number of QCD-RPC events normalised to the number of events of the full three-component model, *i.e.* the ratio (QCD-RPC)/(VDM+QPM+(QCD-RPC)). Two contours are shown: those corresponding to 50% and 75% QCD-RPC contributions. Ignore the small 'islands' in this plot, they are due to low statistics in some bins. This plot suggests a method of isolating an event sample dominated by QCD-RPC processes by introducing cuts in the E_{tag}/E_{beam} *vs.* $W_{visible}$ plane. Initial tests show that requiring a 50% QCD-RPC contribution rejects about half the initial two-photon event sample, a more strict 75% requirement of course leaving still fewer events to study. Due to the at present rather limited VSAT-tagged two-photon event sample ($\sim$500 events), this method of selecting QCD-RPC events will be pursued when more data have been collected.

Having shown the need for QCD-RPC processes to describe the VSAT-tagged data, several different parton density functions (PDF) are available for inclusion in the simulations [42]. Five PDF's have so far been simulated and compared with the data. Two of them, that of D.W. Duke and J.F. Owens (DO) and set 3 of A. Levy, H. Abramowicz and and K. Charchula (LAC3), where found to be incompatible with the data. Differentiating between the other three simulated PDF's, those of L.E. Gordon and J.K. Storrow (GS), DG and set 1 of LAC (LAC1), will require a larger data sample than presently available. Refer to Appendix C for a detailed description of the PDF *vs.* data comparisons.

2.2.3 Results of No-Tagged Data Analyses

Analyses have been performed also with DELPHI no-tagged data [43], *i.e.* with data showing similar low-Q^2 and low-$W_{visible}$ characteristics as the VSAT single-tagged data. The results of the two analyses support each other.

No-tag data were also found to require QCD-RPC processes in order to describe the cross-section and distributions of data. Tests of different parton density functions were carried out by analysing an event sample containing high-p_T jets. The DO and DG PDF's were found to be worse than GS and LAC1 when compared to data.

Chapter 3

Online Beam Monitoring

By an online beam monitoring system is meant a real-time system providing fast response to changing beam parameters. We will here consider the case of monitoring beam conditions at the interaction points of an electron-positron collider.

Real-time knowledge of beam parameters is essential for several reasons. The accelerator physicists need to know how the experiments react to different machine set-ups. They can then tune their accelerator for optimum physics conditions at the interaction points. The particle physicists, having sensitive detectors, need to know the beam conditions to see when they are good enough to start taking data.

In this chapter the main beam parameters of interest to a particle physicist is first introduced, after which the DELPHI system for online monitoring of these is briefly described. This system is treated at length in Appendix D. The features of the VSAT online detector and beam monitoring program `VSAT_MONITOR` is then thoroughly discussed. Finally, a short summary of VSAT measurements of a LEP beam separation scan is given. A more complete discussion is found in Appendix E.

3.1 Main Beam Parameters

From an accelerator physicist's point of view there are many parameters which must be monitored in order to run the machine efficiently. The special devices needed for this task, called beam instruments, are often tailor-made to the accelerator [44]. However, for the particle physicist usually only a few of the main machine parameters are of interest: the luminosity, the background and the beam spot.

3.1.1 Luminosity

A key parameter of any accelerator is its luminosity, which is a measure of the machine's ability to produce particle reactions. The concept of luminosity will first be defined for LEP-like conditions, after which follows a brief description of the Bhabha scattering process which is used for luminosity determination.

3.1.1.1 Definition of Luminosity

Consider the case of an electron-positron collider having its beam particles divided into bunches of the same transverse dimensions. Assuming the beams collide

without any relative incident angle, the counting rate per unit time $dN_{\mathcal{P}}/dt$ of a specific process $\mathcal{P}$ one observes is then given by [45]

$$\frac{dN_{\mathcal{P}}}{dt} = \frac{f\,N^+\,N^-}{2k}\,\frac{\sigma_{\mathcal{P}}}{2\pi\,\sigma_x\,\sigma_y} \tag{3.1}$$

Here f is the particle revolution frequency and $N^+(N^-)$ is the number of positrons (electrons) in the beam. k is the number of particle bunches per beam, leading to $2k$ interaction points around the machine. The probability of the observed reaction $\mathcal{P}$ to occur is called its cross-section $\sigma_{\mathcal{P}}$ and has the dimension of area. The horisontal and vertical transverse beam dimensions are given by σ_x and σ_y. The last denominator thus gives the cross-sectional area under which the beams collide.

It is more common to talk about rates in terms of beam currents I^j, defined by $I^j = N^j\,e\,f$. Here j is either $+$ or $-$ and e is the electron charge. Equation (3.1) can then be rewritten

$$\frac{dN_{\mathcal{P}}}{dt} = \frac{I^+\,I^-}{e^2\,f\,2k}\,\frac{\sigma_{\mathcal{P}}}{2\pi\,\sigma_x\,\sigma_y} \tag{3.2}$$

The luminosity $\mathcal{L}$ is defined by

$$\mathcal{L} \equiv \frac{dN_{\mathcal{P}}/dt}{\sigma_{\mathcal{P}}} \tag{3.3}$$

while the totally delivered luminosity during a certain time interval (*e.g.* a fill), the integrated luminosity $\bar{\mathcal{L}}$, is defined through

$$\bar{\mathcal{L}} \equiv \int \mathcal{L}\,dt = \frac{N_{\mathcal{P}}}{\sigma_{\mathcal{P}}} \tag{3.4}$$

Knowing the luminosity to a high precision is crucial to any particle physics experiment as it, through (3.4), relates the number of detected events N of some interesting reaction (*e.g.* hadronic Z^0 decays) in a certain time to its cross-section, which is often to be found. All data are therefore normalised to the integrated luminosity during which they were taken.

The luminosity of a collider can be found directly by measuring its beam currents I^j and using (3.2) and (3.3). However, the accuracy of this method is too low for high-precision experiments. Instead one normally calculates the luminosity at an interaction point indirectly by measuring the reaction rate of a special process with a known cross-section. This luminosity-calculation process should fulfill the following requirements:

- It should have a comparatively large visible, *i.e.* detectable, cross-section for minimising the statistical error of the measurement. Ideally the cross-section of the luminosity process should be several times that of the physics reactions of interest.
- It should be well-known in order to minimise the systematical error of the measurement. This means both accurately knowing its cross-section and the acceptance of the experimental set-up.

- It should have a high signal-to-noise ratio, again to minimise the systematic error of the measurement. The process should be chosen so that interfering background sources are easily rejectable.

3.1.1.2 The Bhabha Scattering Process

At virtually all electron-positron colliders one has chosen the Bhabha scattering process [46] as luminosity calculation process. The electrons and positrons here undergo elastic scattering against each other, *i.e.* $e^+ + e^- \rightarrow e^+ + e^-$ (Figure 3.1).

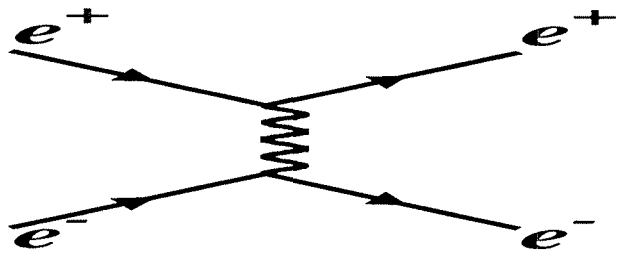

Figure 3.1: The Bhabha scattering process in lowest order QED.

In a lowest order QED approximation the scattered particles have the same energy, but opposite azimuthal and polar angles. A precise luminosity measurement requires that also different weak and radiative processes are taken into account for calculating the Bhabha cross-section [47, 48]. However, for the precision required of an online beam monitoring system, only the lowest order QED process needs to be taken into account, since at high energies and small polar angles the neglected higher order terms are only a factor 10^{-5} of the lowest term [49].

The lowest order QED differential cross-section for the special case of Bhabha scattering into very small polar angles θ at high centre-of-mass energies $\sqrt{s}$ is [48]

$$\frac{d\sigma}{d\Omega} = \frac{4\alpha^2}{s}\frac{1}{\theta^4} \tag{3.5}$$

Here $d\Omega$ is the solid angle element and α is the fine-structure constant. The sharply falling distribution of Bhabha scattered particles with polar angle is evident. Placing detectors closely around the beam pipe thus optimises the yield of Bhabha scattered events.

3.1.2 Background

Ideally, the beam particles in an electron-positron collider circulate in perfect vacuum around a closely defined orbit, each particle having the same energy. In reality this is not true as there also always exists lower momenta beam particles which needs to be rejected by the physics experiments [50]. Beam particles can lose momenta mainly through two processes. Though both involve the acceleration of charges, one normally refers to Bremsstrahlung for motion through matter and

synchrotron radiation for circular acceleration. These processes limit the life-time of the circulating beams.

3.1.2.1 Bremsstrahlung Off-Momentum Beam Particles

Even though the vacuum in the beam pipe might be good there always remain some gas molecules. The nuclei of these molecules can interact electromagnetically with the beam electrons and positrons, bending their trajectories. This acceleration causes photons to be emitted. The process is called Bremsstrahlung [51].

The energy loss of beam particles due to Bremsstrahlung can be considerable, around several GeV, giving rise to beam particles being strongly off-momenta with respect to the nominal value. Most of them go forward, into small polar angles, creating a type of envelope around the beams, and they are thus mainly seen by detectors in the forward direction. The photons mainly go undetected into the beam pipe. When Bremsstrahlung processes occur near the interaction points the photons can be seen by the central tracking devices. The amount of observed background depends on how good the vacuum is around the interaction region.

3.1.2.2 Synchrotron Radiated Photons

Around an electron-positron collider there are several magnets used for beam transport, orbit correction and squeezing. The beam particles emit photons, so-called synchrotron radiated photons, when being accelerated by these magnetic fields [52]. The photon energies are only a few hundred keV. The magnets in the sections around the interaction points can produce photons which are seen principally by the central tracking detectors. The energy losses of the electrons and positrons are small enough to be mostly insignificant, hence there is no beam loss due to this.

3.1.3 Beam Spot

By beam spot is meant the envelope created by the vertices, *i.e.* the exact volume in space at which the beam particles collide. The nominal vertex is designed to be concident with $(x,y,z)=(0,0,0)$ in the detector coordinate system. Due to variations in beam parameters, anomalous situations, alignment problems *etc.* this is not always the case in reality, necessiating beam spot monitoring. Though the precision of an online measurement need not be very high, some (offline) physics analyses require good knowledge of the beam spot.

3.2 The DELPHI Online Monitoring System

A purpose-made system exists for information exchange between the LEP accelerator and the physics experiments [53]. The former provides data on LEP beam currents, collimator settings *etc.* while the experiments measure luminosity, background *etc.* at their interaction points. At the DELPHI experiment the data are available for display [54] as well as logged to a database [55]. The DELPHI online monitoring system, which is fully described in Appendix D, has been used in joint

LEP-DELPHI investigations to optimise the beam conditions at the DELPHI interaction point [56]. Parts of the system hardware and software are also described in [57] and [58]. Some parts of the system have recently been updated to increase speed and reliability [59].

Several DELPHI sub-detectors participate in the online monitoring system in order to have a complete and redundant picture of the beam conditions. Thus luminosity is measured by SAT and VSAT, synchrotron radiated photons are measured by ID and TPC while all of them, as well as special Radiation Monitors (RM), measure off-momentum beam particles.

Some SAT and VSAT signals, and all the RM signals, are always available independently of the DELPHI data acquisition system. The TPC signals and some ID signals also become available when their high-voltages are turned on. When the DELPHI data acquisition is finally running all the monitoring signals are available.

The available signals at a given time are thus dependent on the current beam conditions. This is displayed by Figure 3.2, showing DELPHI online monitoring for the beginning of a LEP fill. The top histogram (VSAT BKGD1) is a measure of the VSAT off-momentum beam particle trigger rate. The second histogram (VSAT TRIGGER LUM.) shows the VSAT Bhabha trigger rate, which is proportional to luminosity. Since SAT is the main luminosity detector of DELPHI, this rate is scaled to the SAT-calculated luminosity. Both these VSAT signals come directly from its local trigger, and they are therefore always available. Histogram three (TPC BKGD2) is proportional to the total counting rate of the TPC wires, *i.e.* proportional to both synchrotron photons and off-momentum beam particles. The luminosity given by the SAT online monitoring program (SAT ONLINE LUM.) is displayed in the fourth histogram. This signal is available only when DELPHI is taking data. All histograms show rate or luminosity along the vertical axis and time along the horisontal axis.

Below is a description of what is seen in Figure 3.2. The letters **A** to **F** refer to those along the bottom of the figure, indicating at what time some operation was carried out.

- **A** No beams in LEP.
- **B** Particles are injected into LEP. The beams are rather 'dirty' as can be seen from the high VSAT BKGD1 rate. The low VSAT TRIGGER LUM. values indicate that the beams are circulating with very few collisions.
- **C** VSAT TRIGGER LUM. rises steeply, meaning the beams have correct energy and are brought into collision. Some further beam tuning is performed as VSAT TRIGGER LUM. continues to increase slowly. VSAT BKGD1 is still high.
- **D** The collimators are moved into their correct positions. This is monitored by VSAT BKGD1 as a sharp decrease in background.
- **E** The VSAT BKGD1 background is considered low and stable enough for the DELPHI operators to turn on the TPC high-voltages. TPC BKGD2 then goes up to a stable value.
- **F** Both VSAT BKGD1 and TPC BKGD2 backgrounds are low and stable so the DELPHI data acquisition is started. SAT ONLINE LUM. is seen to agree well with VSAT TRIGGER LUM.

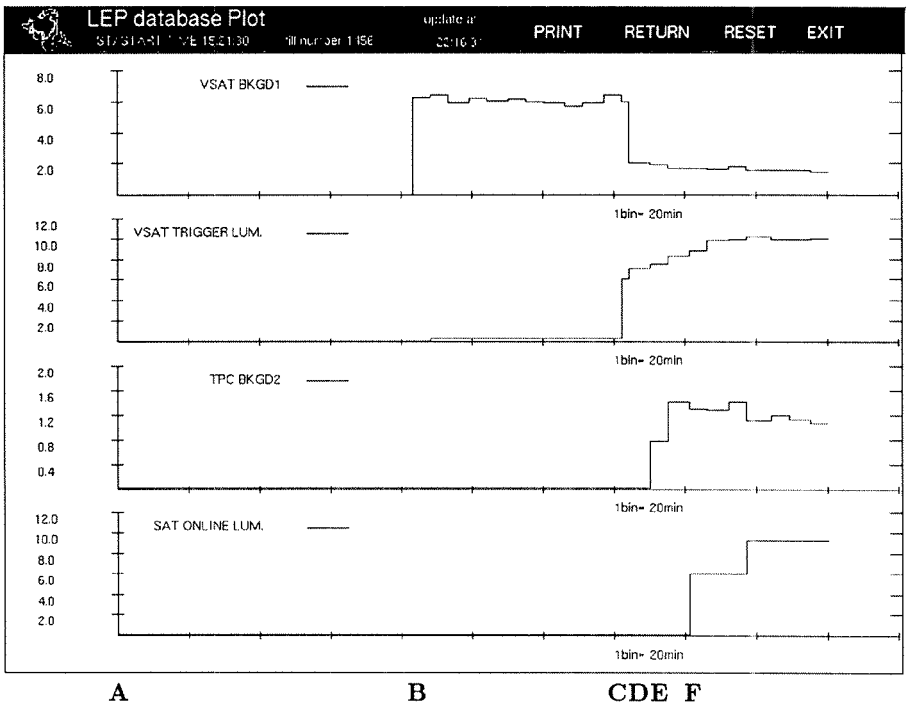

Figure 3.2: DELPHI online monitoring of the beginning of LEP fill 1456. The data were picked up from the database. The figure is described in the text.

3.3 The VSAT Online Monitoring Sub-System

Due to the VSAT coverage of very small polar angles, *i.e.* being placed close to the beam pipe, it can provide useful information on different beam parameters. Online beam monitoring was originally the main reason for constructing the VSAT. Several VSAT signals are available online, some of them independently of the DELPHI data acquisition.

Both DELPHI-gated and ungated signals are sent directly from the local VSAT trigger. They give information on off-momentum beam particle background, Bhabha scattering events (for luminosity determinations) and background to the Bhabha events. The signals are available together with a bunch counter, making studies of individual LEP particle bunches possible. The VSAT trigger signals are described in detail in Appendix D, and they will not be further discussed here.

DELPHI-gated online signals are also available from the VSAT online monitoring program, `VSAT_MONITOR`, which is decribed below. This program, running on

the VSAT-specific equipment computer, analyses the sample of VSAT data made available for monitoring by the DELPHI data acquisition system [60, 61, 62, 63]. Then follows a performance test of the VSAT_MONITOR routines, where comparisons are made with online and offline results from different DELPHI and LEP detectors. VSAT raw data files were moved to the DELPHI online cluster for some of these comparisons. VSAT_MONITOR was then set up to run in a so-called playback mode (see details below).

3.3.1 The VSAT_MONITOR Program Package

The main purpose of an online monitoring program is to immediately spot any errors in the detector's data stream. It can also supervise the general status of the detector, detecting changes in pedestal values *etc.* Some detectors can also directly, through its online monitoring program, provide useful physics results by rapidly analysing the data as they are taken. All these tasks are performed by the VSAT online monitoring program package, called VSAT_MONITOR, consisting of around 6000 lines of FORTRAN code and 1000 lines of DCL command language code. It provides both interactive and non-interactive monitoring of the VSAT [64].

Interactive monitoring of individual data buffers, which for the VSAT normally contains a few events each, is available through event displays. The user can here either display the raw data which, for the VSAT, are packed in hexadecimal format or in the final unpacked, pedestal-subtracted and calibrated format. A graphical event display have also been available, showing profiles over all data channels together with trigger information (see Appendix A, Figure 5 or Appendix E, Figure 2). It is also possible to interactively access the run-integrated histograms produced by the non-interactive task (see below) through a histogram presenter. Different operations can be performed on the histograms. Reference histograms, displaying how it 'should' look, are superimposed on each plot for comparison. Any number of users can run interactively, also from remote terminals. The user can select to look at data either online or offline, running the program in playback mode and analysing previously taken data from a file on the DELPHI online cluster. The user has at each level the option to print the current display.

The non-interactive VSAT_MONITOR task, running in batch mode on the VSAT equipment computer, is the main monitoring utility. It is always running when DELPHI is taking data, hibernating between runs. Each event is unpacked and decoded concerning physics data, pedestal data, trigger and error flags *etc.* In order to optimise the CPU-usage very few operations are performed on an event-by-event basis. Event data is instead stored in vectors. At certain time intervals operations are performed on these vectors. Thus every 60 seconds some vectors are normalised and histogrammed, while every 10 minutes results on LEP beam spot and luminosity are calculated and sent to the DELPHI online monitoring system.

Most of the operations are performed at the end of each run when output files are written and error checks are made. Error checking is crucial to ensure a stable VSAT performance. Checks are therefore carried out on a large number of parameters like percentage of corrupt events, trigger distributions in the four VSAT modules, mean ADC-values for the channels *etc.* Any value found to be outside the allowed range results in an error message being injected into a special error message utility, routing

the message to predefined receivers. Key data, any error messages and all delivered beam spot and luminosity values are automatically written to end-of-run summary files which are saved for reference.

VSAT_MONITOR also communicates with the VSAT online database [65]. At each beginning of a new run, VSAT_MONITOR reads in the current database values concerning pedestal values and channel status flags (*i.e.* which channels are considered non-functional). New pedestal values, and widths, together with new channel status flags are calculated by VSAT_MONITOR at certain intervals. The database update routines, which are normally hibernating, are then woken up. Any significant changes lead to updates in the database.

The global steering of VSAT_MONITOR is to a large extent determined by values read in from external files at each start-of-run. A user can thus decide what error checks to be made, what error limits to be allowed, what files to write *etc.*

The non-interactive part of VSAT_MONITOR should always be running in online mode only. However, for special sessions a user can redefine its data input area to point to a data file. This is called playback mode. The difference between the playback and online modes is that in playback mode all the data is seen by VSAT_MONITOR, while in online mode the data sample actually monitored depends on the CPU load of the VSAT equipment computer and the live-time of the data acquisition. During the 1991 runs about 80% of the VSAT data were monitored online. In later years practically 100% have been monitored, due to the installation of a more powerful equipment computer.

3.3.2 Event Selection

VSAT_MONITOR uses only selected and background-corrected Bhabha events for its online luminosity and beam spot analyses. The event selection criteria are broadly similar to those of the VSAT offline analysis programs. The main criteria are listed below, as are the differences from the routines on the offline level.

- The data words are first unpacked and checked for correct data format. Any corrupt or unreconstructable events are discarded.
- The analyses use only events triggered as Bhabha or False Bhabha. A False Bhabha event is defined as an accidental Bhabha coincidence, *i.e.* an event where a single hit in a VSAT module is followed by a hit in its diagonal module the next time the same two bunches collide. These events, coming from purely statistical coincidences between off-momentum beam particles surrounding the beams, indicate the background level.
- Incident (x, y)-positions are reconstructed. The online routines only find which strips were hit, and assign the centres of these strips as incident (x, y)-positions. As the strip planes have a one millimeter pitch this means a 500 μm position resolution. Special position-reconstruction algorithms are used offline, here resulting in a position resolution of 200 μm [66].
- Hits within one millimeter from any calorimeter edge are considered to have lost too much of their electromagnetic showers outside the detectors, and the event is discarded.

- A one-dimensional shower leakage correction is applied for hits with an x-position between 2 and 10 mm to the beam-pipe edge of a module. The correction, which is in the form of a pre-calculated look-up table, gives a maximum contribution of 25%. VSAT offline routines use a more exact two-dimensional correction function, taking into account also the cases of leakages close to a calorimeter corner and along the vertical (y) edges.
- Low-energetic events, with a hit having energy less than 36.5 GeV after leakage correction, are discarded. This fixed energy cut is 80% of the beam energy at the Z^0 peak. The offline energy cut was originally 80% of the actual beam energy. For later analyses this has been lowered to 70%.
- The number of False Bhabha events, which survive the above cuts, are finally subtracted. The events are then considered to be background corrected.

3.3.3 Luminosity Measurements

The precision of the VSAT_MONITOR online luminosity measurements was first tested by comparing with final SAT and VSAT offline results. SAT results were here used as reference in order to discover any VSAT-specific systematic errors. Due to statistical reasons all comparisons were carried out on a run by run basis, where each run was required to have more than 20 Bhabha events in the SAT. The average SAT and VSAT combined statistical error per run (see below) was found to be around 10%. Accepted runs needed to have both SAT and VSAT offline status flags set to zero (*i.e.* good runs). The final data sample consisted of 63 runs taken from ten LEP fills.

The upper histogram of Figure 3.3 shows, for each of the 63 runs, the ratios between the number of accepted Bhabha events by VSAT_MONITOR and by SAT offline. VSAT_MONITOR is seen to accept 18.25 times more Bhabha events than SAT, reflecting the strong forward peaking of the Bhabha cross-section (equation (3.5)). This high event rate is essential for having a reasonable statistical event sample inside the small time intervals (10 to 20 minutes) required for online monitoring purposes. Fitting a straight line to the ratios results in a χ^2 of 1.133, indicating a stable ratio between VSAT online and SAT offline Bhabha counting.

Corresponding ratios for VSAT offline and SAT offline Bhabha events are given by the lower histogram of Figure 3.3. The lower energy cut of the VSAT offline routines is here seen to lead to the slightly higher mean ratio of 19.13, while the fit results in the same χ^2-value. The Bhabha counting precision is therefore virtually identical for the VSAT online and offline programs.

Knowing the visible Bhabha cross-section is essential for a precise luminosity measurement. For the VSAT case this cross-section is quite sensitive to different beam parameters, which is corrected for at the offline level using dedicated algorithms [67, 68]. Similar corrections were also tried for VSAT_MONITOR, but they were found not to improve results since the statistical fluctuations inside a 10 min update interval are large compared to the corrections. A fixed Bhabha cross-section of 500 nb was instead used, taken as the mean value from offline results. This cross-section can vary slightly from year to year depending on the exact positions of the VSAT modules.

Figure 3.4 shows differences in luminosity values weighted by the combined VSAT

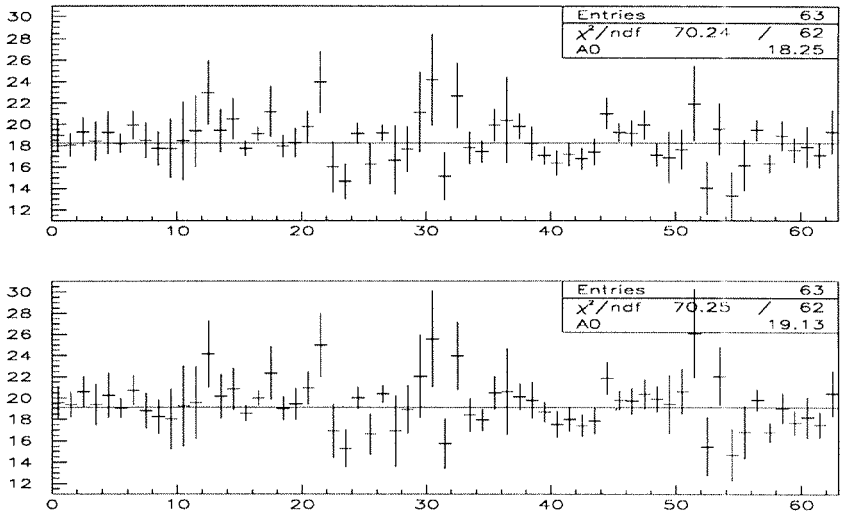

Figure 3.3: Bhabha counting ratios between VSAT online and SAT offline routines (upper histogram), and VSAT offline and SAT offline routines (lower histogram).

and SAT statistical errors, *i.e.* for each run R the histograms are filled with

$$\frac{\bar{\mathcal{L}}_R^{VSAT} - \bar{\mathcal{L}}_R^{SAT}}{\sigma^2_{comb.stat.}} \tag{3.6}$$

where the combined statistical error is given by

$$\sigma_{comb.stat.} = \sqrt{1/N^{VSAT}_{Bhabha} + 1/N^{SAT}_{Bhabha}} \tag{3.7}$$

The upper histogram compares VSAT online and SAT offline, while the lower one reflects VSAT offline *vs.* SAT offline. Using the RMS-values of Figure 3.4, estimates of the combined VSAT and SAT systematic errors of the luminosity measurements can be calculated by [69]

$$RMS^2 - 1 = \frac{\sigma^2_{comb.syst.}}{\sigma^2_{comb.stat.}} \tag{3.8}$$

The calculations give a combined VSAT online and SAT offline systematic error of (3.4±2.3)%, while the combined VSAT and SAT offline error is (2.9±2.4)%.

Again the VSAT online and offline routines give similar results, especially taking into account the large uncertainties of the systematic error estimates. These arise due to fluctuations in the comparatively small data sample tested. Knowing the systematic errors to higher precision requires using much more data, on the scale of the full DELPHI 1991 data sample. This has been performed for final VSAT offline analysis, resulting in a systematic error on the relative luminosity measurements of less than 0.2% [70].

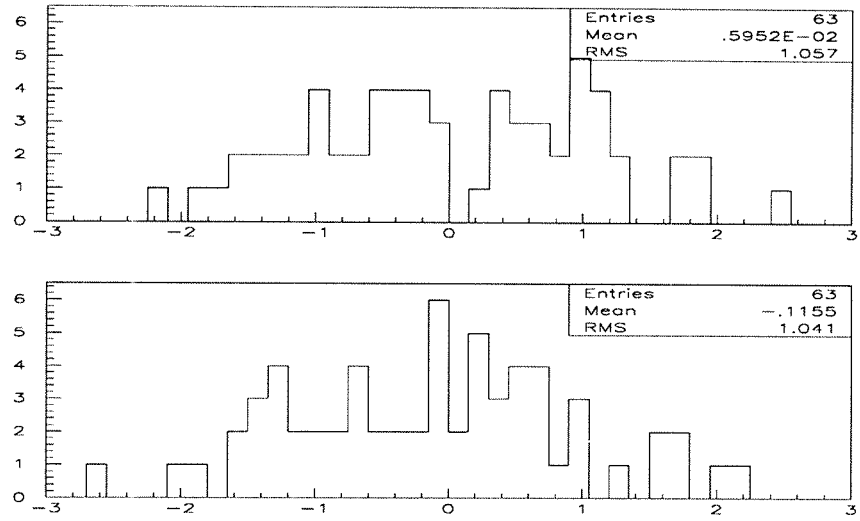

Figure 3.4: Error weighted luminosity differences between VSAT online and SAT offline (upper histogram) and VSAT offline and SAT offline (lower histogram).

The above combined VSAT+SAT systematic errors correspond to the average VSAT statistical error for a 10 minute online data sample. The accuracy of **VSAT_MONITOR** can therefore be considered adequate for the purpose of an online luminosity measurement, being much better than the required 10% error level.

Finally, **VSAT_MONITOR** luminosity calculations were compared inside a fill to those calculated by the SAT online monitoring program, which is being claimed to agree within a few percent to the SAT offline results. Data from a 1992 fill are displayed in Figure 3.5.

The upper histogram shows superimposed VSAT and SAT luminosities. SAT is the trace having wider (20 min) bins than VSAT (10 min). The lower histogram gives the VSAT/SAT luminosity ratio. A good agreement is seen between the two detectors' measurements: both respond to luminosity changes inside the fill in a similar manner, resulting in a stable ratio of around one. The peaks are due to few events inside the rather short time intervals, the SAT having about nine times less data than VSAT.

3.3.4 Beam Spot Measurements

The **VSAT_MONITOR** beam spot calculations use Bhabha events having passed the event selection criteria of Chapter 3.3.2. For each event the horisontal beam spot position (*i.e.* the x-position) is calculated by summing, with signs, the two reconstructed x-positions of the VSAT modules. This sum is proportional to the horisontal beam position. The final value is found at the end of each time interval by taking the weighted mean value of the sums in the two VSAT Bhabha diagonals.

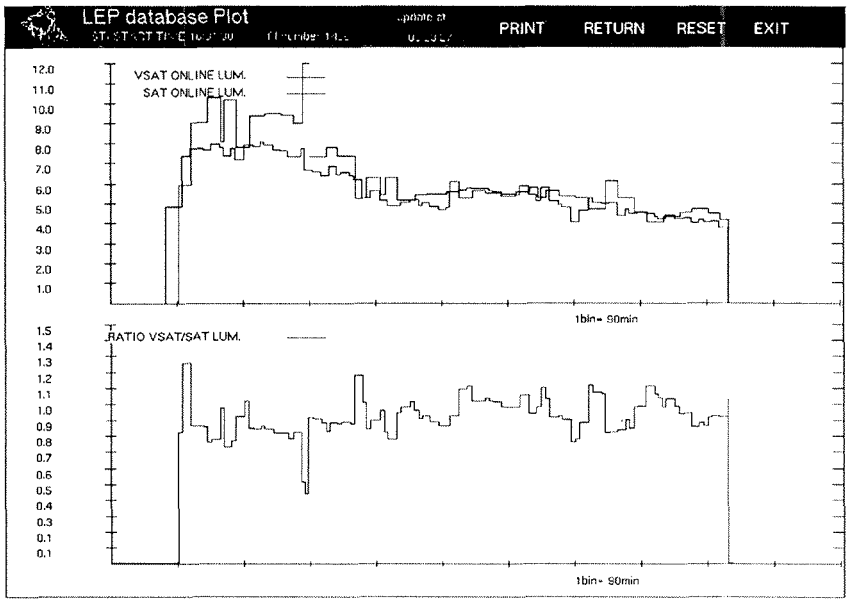

Figure 3.5: VSAT online and SAT online luminosities from fill 1456. In the upper histogram the SAT trace is the one having wider bins.

The vertical beam spot position (*i.e.* the y-position) is calculated in the same way.

The longitudinal beam spot position (*i.e.* the z-position) is found by taking instead the difference, with signs, of the above x-position sums from each VSAT Bhabha diagonal. This difference is proportional to the deviation of the longitudinal beam spot position from the nominal zero value (z=0).

Micro-Vertex beam spot data [71] were used for determining the precision of the `VSAT_MONITOR` horisontal and vertical beam spot calculations, while TPC data [72] were used for testing the longitudinal beam spot estimates.

3.3.4.1 Horisontal Beam Spot Position

Horisontal beam spot comparisons with the micro-vertex detector were done on a run-by-run basis, the only requirement being a minimum of 800 VSAT Bhabha events per run. This corresponds roughly to discarding runs shorter than 10 minutes, *i.e.* the minimum time interval used by `VSAT_MONITOR` for giving online estimates. The data sample used in the analysis consisted of 82 runs from 12 LEP fills.

Figure 3.6 shows the horisontal beam spot positions of `VSAT_MONITOR` *vs.* micro-vertex data. The two measurements are seen to be correlated. Fitting a straight line to the 82 data points results in a χ^2-value of 1.178. There is an overall scale factor between the two detectors, which is due to the magnifying effects of the quadrupole magnets in the horisontal direction.

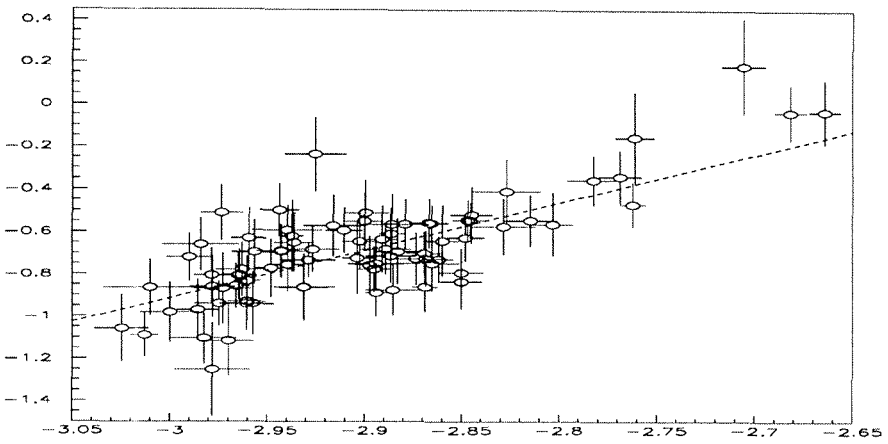

Figure 3.6: VSAT online *vs.* micro-vertex x-positions (mm).

As for the luminosity determinations, VSAT_MONITOR beam spot horisontal positions were plotted inside a fill (Figure 3.7). Data of the LEP Beam Orbit Measuring system (BOM) [44] were superimposed for comparison. The two overlapping curves on top of Figure 3.7 are the BOM electron and positron beam x-positions while the lower curve shows VSAT_MONITOR data. Apart from a scale factor the VSAT is seen to follow the BOM data. The situation in Figure 3.7 is representative of some ten other LEP fills displayed in the same manner.

Though the errors of the VSAT_MONITOR horisontal beam spot measurements are not comparable to those of the micro-vertex, they are still useful for online monitoring, backup measurements and alignment purposes.

3.3.4.2 Vertical Beam Spot Position

VSAT_MONITOR vertical beam spot measurements were compared with the micro-vertex detector as described above.

The upper histogram of Figure 3.8 shows VSAT online vertical beam spot data *vs.* micro-vertex data for 74 runs from 11 LEP fills being rather close together in time (sample 1). That the VSAT_MONITOR vertical beam spot determination accuracy is lower than the horisontal one is seen in the figure, resulting in a worse fit to the micro-vertex ($\chi^2 = 3.312$). The reason is the superconducting quadrupole magnets in front of the VSAT modules, focusing outgoing particles in the vertical direction. The VSAT sensitivity to beam movements in this direction, which are often quite small, is therefore reduced accordingly.

Data from a later LEP fill was then added as shown in the lower histogram of Figure 3.8 (sample 2). The data from this fill can be seen clustered together in the lower left corner of the histogram. An approximately 1.1 mm vertical beam movement is visible, as measured by both VSAT_MONITOR and the micro-vertex, compared

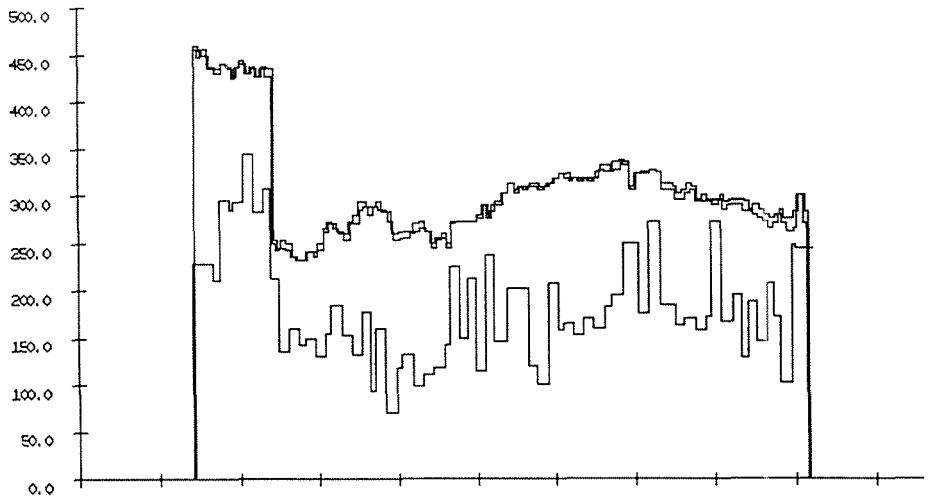

Figure 3.7: VSAT online and LEP BOM x-positions (μm). The two overlapping curves on top are BOM data for the electron and positron beams respectively.

to the compact cluster of sample 1. This quite large vertical beam movement in the 1991 LEP fills was also found by a full DELPHI beam spot analysis using micro-vertex, ID and TPC data [73]. The beam movement was due, at least partly, to LEP moving the quadrupole magnets in front of the VSAT [74]. This also explains why no scale factor was found between the VSAT and micro-vertex measurements.

From the above discussion, it is clear that the `VSAT_MONITOR` sensitivity to normal (*i.e.* small) vertical beam spot movements is low due to the quadrupole focusing effects. However, larger movements can be monitored.

3.3.4.3 Longitudinal Beam Spot Position

A run-by-run analysis of `VSAT_MONITOR` longitudinal beam spot estimates revealed the statistical errors to be too large for any conclusions to be drawn. Comparisons with the TPC were instead carried out on a fill-by-fill level, the results being shown in Figure 3.9. A linear relation between the two measurements is visible, the χ^2 being 1.495. Though the VSAT error bars are appreciable even when integrating over whole fills, useful longitudinal beam spot information is obtainable after only a few runs.

3.4 VSAT Monitoring of a Beam Separation Scan

In the spring of 1990 VSAT monitored a LEP beam separation scan. At this time VSAT was not included in the central DELPHI data aqcuisition, and the VSAT online monitoring routines were not fully developed. Data analysis was instead done offline. Full details of the beam separation scan is given in Appendix E.

From equation (3.1) it is seen that the accelerator luminosity is maximal when many beam particles collide in a small transverse area. The parameters of the beam

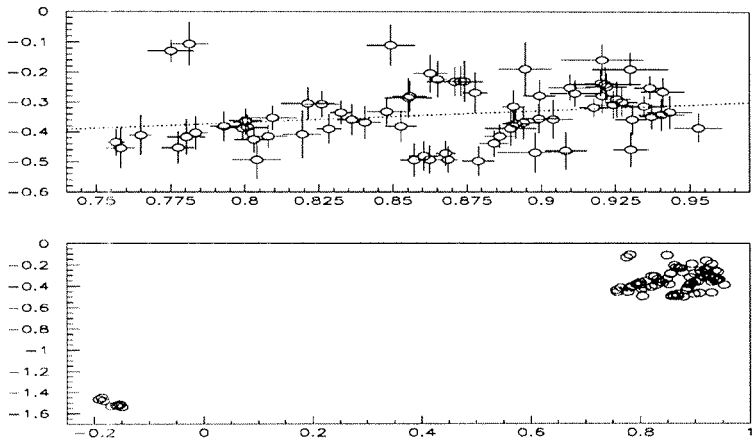

Figure 3.8: VSAT online *vs.* micro-vertex y-positions (mm) for sample 1 (upper histogram) and sample 2 (lower histogram).

optics should reflect this, they being tuned for maximal luminosity delivery. The beam separation scan was carried out in order to test the LEP beam optics.

The LEP beam bunches are highly elliptical, having nominal horisontal and vertical transverse dimensions of σ_x=300 μm and σ_y=12 μm respectively. The small vertical dimension leads to high demands on the vertical beam optics to ensure that the beams collide head-on. Optimal optics parameters were found by separating the beams in the vertical direction using electrostatic separators. Meanwhile VSAT measured the resulting Bhabha scattering event rates, these being proportional to luminosity according to (3.3).

Measurements were made at vertical beam separations of 0 μm, 10 μm, 20 μm and 30 μm. Both beams were moved symmetrically around the nominal zero position, and tests were performed with moving the electron-positron beams up-down as well as down-up. Two values of the LEP so-called β-function [75] were tried: β=7.0 cm and β=4.3 cm.

The nominal beam optics, *i.e.* 0 μm beam separation, was in all cases found to give maximum luminosity, confirming earlier LEP calculations. Changing the β-value from 7.0 cm to 4.3 cm lead to a measured luminosity increase of 22%.

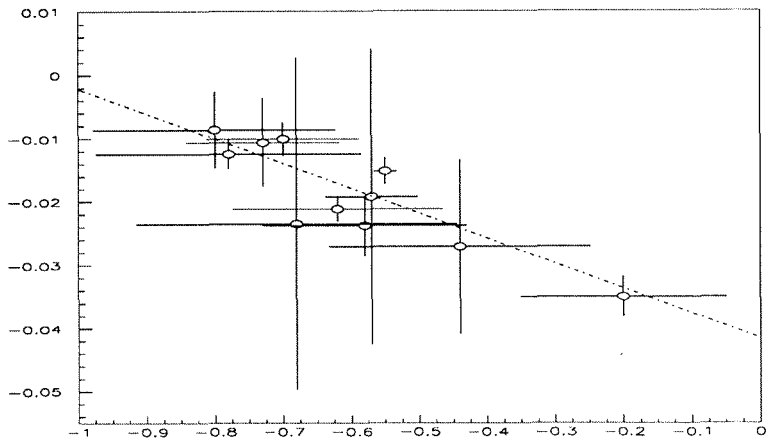

Figure 3.9: VSAT online *vs.* TPC z-positions.

Acknowledgements

I would like to thank my supervisor, Professor Göran Jarlskog, for patiently supporting me in every way and giving me the chance to do this work.

Being a Ph.D. student, many things are best learnt by working together with more senior physicists. I have been very fortunate to work with my collegues and friends Ulf Mjörnmark, Valery Pozdnyakov and Nikolai Zimin. I wish to thank them for their truly invaluable help.

Modern elementary particle physics experiments requires the co-operation of a large number of people, and a very large experiment like DELPHI is no exception. I would like to thank the members of the DELPHI Collaboration for providing a nice working environment and making this thesis possible. In particular, I thank Giuseppina Rinaudo of the VSAT group and Frederic Kapusta and Igor Tyapkin of the two-photon physics team for many fruitful discussions and much help.

Thanks are also due to everybody at the Department of Elementary Particle Physics in Lund. I have especially appreciated the good times and many laughs shared with my fellow-students Anders, Ivan, Lars and Olof.

The financial support from the University of Lund is gratefully acknowledged.

Bibliography

[1] J. Bjarne, Beam Monitoring in LEP, LUNFD6/(NFFL-7049)1988
[2] G.P. Ferri *et. al.*, CERN/ECP 90-8 CERN/SL 90-110 (BI)
[3] The LEP in short, Eds: M. Buhler-Broglin, D. Lajust, R. Lewis, CERN Publications, 1989
[4] Large Electron-Positron storage ring, Tecnical notebook, CERN Publications, 1989
[5] G. Guignard, LEP Parameter Note 9
[6] DELPHI Collaboration, Nucl. Instr. and Meth. A303(1991)233
[7] F. Hartjes *et. al.*, Nucl. Instr. and Meth. A256(1987)55
[8] C. Brand *et. al.*, Nucl. Instr. and Meth. A283(1989)567
[9] A. Amery *et. al.*, Nucl. Instr. and Meth. A283(1989)502
[10] P. Checchia *et. al.*, Nucl. Instr. and Meth. A248(1986)317
[11] G. Barichello *et. al.*, Nucl. Instr. and Meth. A254(1987)111
[12] P. Checchia *et. al.*, Nucl. Instr. and Meth. A275(1989)49
[13] L. Bugge *et. al.*, DELPHI 91-104 PHYS 147
[14] DELPHI Collaboration, CERN/LEPC/92-6, LEPC/P2-Add.1
[15] T. Camporesi *et. al.*, CERN-PPE/92-212
[16] PLUTO Collaboration, Ch. Berger *et al.*, Z. Phys. **C26**(1984)353
[17] TPC/2γ Collaboration, H. Aihara *et al.*, Phys. Rev. Lett. **58**(1987)97; TPC/2γ Collaboration, H. Aihara *et al.*, Phys. Rev. **D41**(1990)2667
[18] AMY Collaboration, R. Tanaka *et al.*, Phys. Lett. **B277**(1992)215
[19] ALEPH Collaboration, D. Buskulic *et al.*, Phys. Lett. **B313**(1993)509
[20] L3 Collaboration, O. Adriani *et. al.*, Phys. Lett. **318B**(1993)575
[21] OPAL Collaboration, R. Akers *et. al.*, Z.Phys. **C61**(1994)119
[22] F.M. Renard, Basics of Electron Positron Collisions, Editions Frontières, 1981
[23] H. Kolanoski, Two-Photon Physics at e^+e^- Storage Rings, Springer, 1984
[24] H. Kolanoski, P. Zerwas, High Energy Electron-Positron Physics, Eds: A. Ali, P. Söding, World Scientific, Singapore, 1988
[25] M. Feindt, CERN-PPE/91-90
[26] J.S. Steinman, Thesis, UCLA-HEP-88-004, 1988
[27] F. Naraghi, Thesis, Univ. Paris VII, 1992
[28] H.-U. Martyn, DESY 89-121 PITHA 89/20
[29] PLUTO Collaboration, Ch. Berger *et al.*, Phys. Lett. **B149**(1984)421
[30] TASSO Collaboration, M. Althoff *et al.*, Z. Phys. **C31**(1986)527
[31] CELLO Collaboration, H.J. Behrend *et al.*, Z. Phys. **C51**(1991)365
[32] J. Rosner, NBL Report 17522(1972)316
[33] J. Rosner, Brookhaven Report CRISP 7126 (1971)

[34] I.F. Ginzburg, V.G. Serbo, Phys. Lett. **B109**(1982)231
[35] J.J. Sakurai, D. Schildknecht, Phys. Lett. **B41**(1972)489
[36] B. Batyunya *et. al.*, DELPHI 94-76 PHYS 393
[37] B. Batyunya *et. al.*, DELPHI 93-60 PHYS 288
[38] J. Bjarne *et. al.*, DELPHI 93-90 PHYS 317
[39] R. Brun, D. Lienart, CERN Program Library Y250
[40] A.G. Frodesen, O. Skjeggestad, H. Tøfte,
Probability and Statistics in Particle Physics, Universitetsforlaget, 1979
[41] M. Drees, K. Grassie, Z. Phys. **C28**(1985)451
[42] H. Plothow-Besch, CERN/PPE 92-123
[43] DELPHI Collaboration, Z. Phys. **C62**(1994)357
[44] C. Bouvet, CERN SL/91-17 (BI)
[45] K. Potter, Proc. of the 1984 CERN Accelerator School, CERN 85-19
[46] H.J. Bhabha, Proc. Roy. Soc. **A.154**(1936)
[47] M. Caffo, E. Remiddi, Z Physics at LEP 1, Vol. 1, CERN 89-08
[48] M. Dam, L. Bugge, DELPHI 87-81 PHYS 21
[49] G. von Holtey, LEP Note 462
[50] H. Burkhardt *et. al.*, CERN SL/94-25 (EA)
[51] A.M. Smith, LEP Note 559
[52] P. Roudeau, LEP Note 472
[53] M.J. Clayton, G. von Holtey, P. Lienard, LEP Controls Note 94
[54] C. Gaspar, M. Dönszelmann DELPHI 94-4 DAS 148
[55] Yu. Belokopytov *et. al.*, DELPHI 93-2 PROG 193
[56] Ph. Charpentier *et. al.*, DELPHI 92-147 PHYS 240
[57] G. Jarlskog, M. Jonker, DELPHI 89-59 MIG 3
[58] J.A. Fuster *et. al.*, DELPHI 91-112 DAS 115
[59] M. Dönszelmann, C. Gaspar DELPHI 93-131 DAS 145
[60] Ph. Charpentier, C.M. Story, DELPHI 86-47 DAS 32
[61] Ph. Charpentier *et.al.*, Proc. of Computing in High Energy Physics '91
[62] M.J. Jonker *et.al.*, Proc. of Computing in High Energy Physics '91
[63] B. Franek *et.al.*, Proc. of IEEE 1991
[64] J. Bjarne, I. Kronkvist, U. Mjörnmark, VSAT Online Shift Instructions,
Internal VSAT report
[65] F. Bianchi, I. Kronkvist, DELPHI 92-116 PROG 190
[66] M. Koratzinos, VSAT Position Reconstruction, Internal VSAT report
[67] A. Håkansson, DELPHI 93-49 PHYS 279
[68] A. Håkansson, Thesis, Univ. of Lund, LUNFD6/(NFFL-7077)1993
[69] L. Lyons, DELPHI 91-97 PHYS 143
[70] DELPHI Collaboration, DELPHI 92-77 PHYS 188
[71] D. Johnson, D. Reid, W. Trischuk, DELPHI 92-36 PHYS 168
[72] G. Hamel de Monchenault, P. Jarry, Y. Sacquin, DELPHI 91-05 PROG 159
[73] P. Billoir, F. Ledroit, Tz. Spassoff, DELPHI 92-3 PHYS 152
[74] T. Taylor, Private communication
[75] H. Widemann, Particle Accelerator Physics, Vol. 1, Springer, 1993

Nuclear Instruments and Methods in Physics Research A305 (1991) 320–330
North-Holland

A silicon–tungsten electromagnetic calorimeter for LEP

Lund [1]–Milano [2]–Torino [3]–Trieste [4] Collaboration
S. Almehed [1], F. Bianchi [3], J. Bjarne [1], W. Bonivento [2], H. Carling [1], R. Cirio [3], M.P. Clara [3], N. Demaria [3], A. De Min [2], P. Folegati [1], D. Gamba [3], A. Hakansson [1], G. Jarlskog [1], G. Kidrich [4], E. Menichetti [3], U. Mjornmark [1], P. Negri [2], P. Poropat [4], G. Rinaudo [3], A. Romero [3], M. Sessa [4], P.P. Trapani [3] and E. Vallazza [3]

Received 31 January 1991

This report describes a silicon–tungsten electromagnetic calorimeter used to determine some beam properties and luminosity in the DELPHI experiment at LEP. The polar angular range covered by this detector is 5–8 mrad, which allows the detection of a Bhabha rate about 10 times the rate of produced Z particles at the peak cross section.

1. Introduction

Each experiment at the CERN large electron–positron collider (LEP) needs to monitor beam conditions and the luminosity of their particular interaction region. The luminosity is derived from the observation of elastically scattered electrons in a well known process, Bhabha scattering. In DELPHI this is done by the means of two different luminosity monitors. The small angle tagger (SAT) covers the polar angular range from 50 to 120 mrad, and the very small angle tagger (VSAT) the subject of this article, covers the range of about 5 to 8 mrad. At its small angle position the VSAT detector has a very high cross section for the Bhabha scattering process, thus obtaining a high statistical precision. However it is quite sensitive to background conditions, beam parameters, and to the precision by which the exact geometry of the detector and the beam transport are known.

The VSAT detector consists of four rectangular calorimeter modules 5 cm high, 3 cm wide and 24 radiation lengths deep. They are located 7.7 m downstream of the DELPHI interaction point, as indicated in

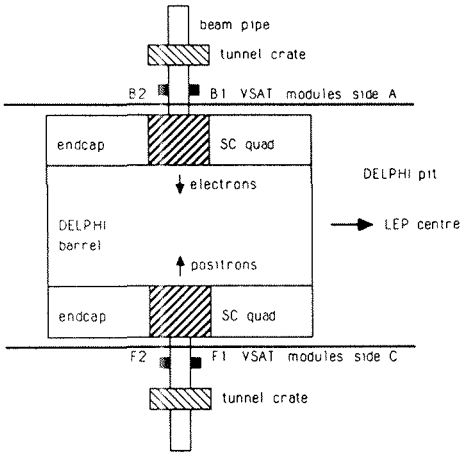

Fig. 1. Layout of the VSAT detector and the DELPHI environment.

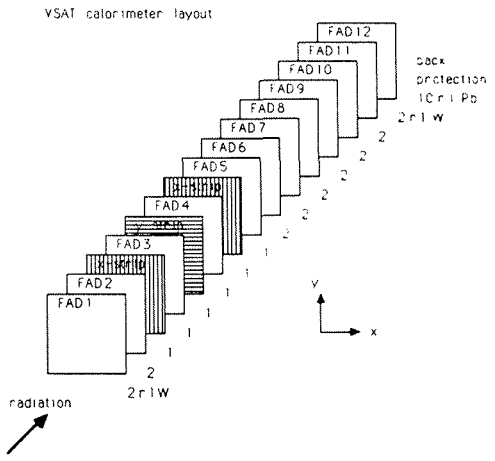

Fig. 2. Calorimeter module layout.

fig. 1. On each side of DELPHI there is one module on the inside and one on the outside of the short elliptical section of the beam pipe, behind the superconducting quadrupoles producing the final focus. These quadrupoles deflect the Bhabha scattered electrons and positrons towards the four detector modules positioned in the horizontal beam plane. This allows the direct observation of the interaction region with relatively little absorbing material in front.

The differential cross section of Bhabha scattering is falling with increasing polar angle θ as θ^{-3}, giving a total rate, integrated over the VSAT acceptance, of a factor 10 above the rate of produced Z at its peak. For the nominal design setting of the LEP beams this means a VSAT Bhabha rate of about 5 Hz.

The contribution to the Bhabha process of radiative processes varies with polar angle – in the SAT region electroweak corrections cannot be neglected, while in the VSAT region only QED corrections need to be considered. In the VSAT the electrons are always well separated from the radiated photons, due to the quadrupole, while this need not be the case for the SAT. Detailed measurements of the radiative Bhabha scattering process in the two regions therefore provide valuable tests on different calculations.

The VSAT detector is designed to measure also the

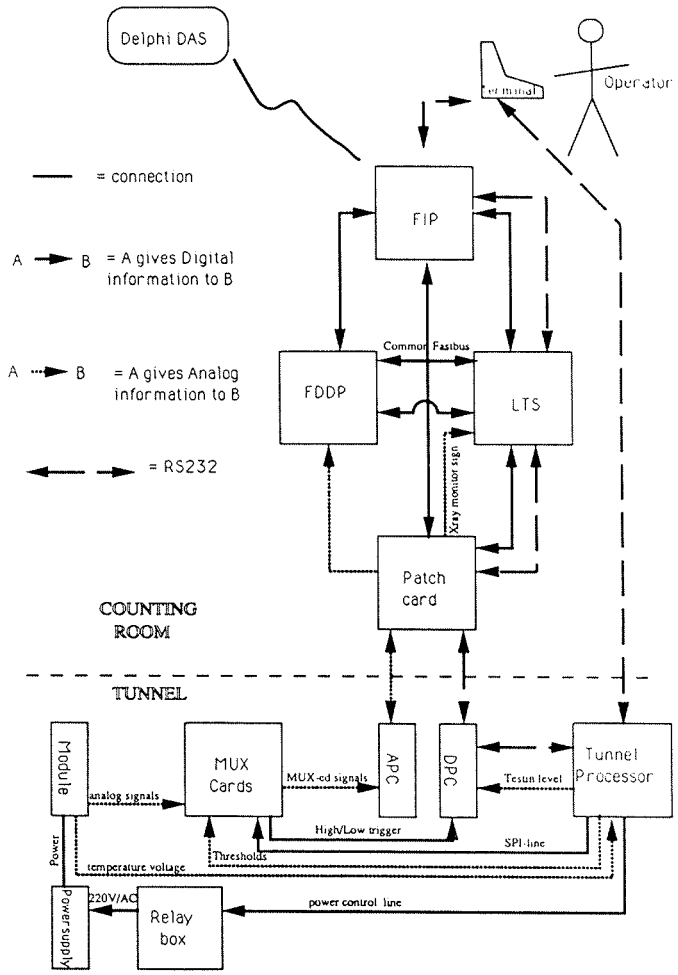

Fig. 3. Block diagram of the readout electronics.

background of beam-gas produced off momentum electrons and of synchrotron radiated X-rays. These measurements provide checks on the optimization of orbits in the LEP machine, and the off-momentum electron background rate can also be used to estimate the accidental background to the Bhabha process. All events are bunch labelled (one through four) and different bunch–bunch configurations can therefore be separated. This has a special interest when the bunches are different as will be the case if in the future the LEP beams can be polarized.

In section 2 the electromagnetic calorimeter modules are described and in section 3 the readout system is discussed. The detector performance, with comparison

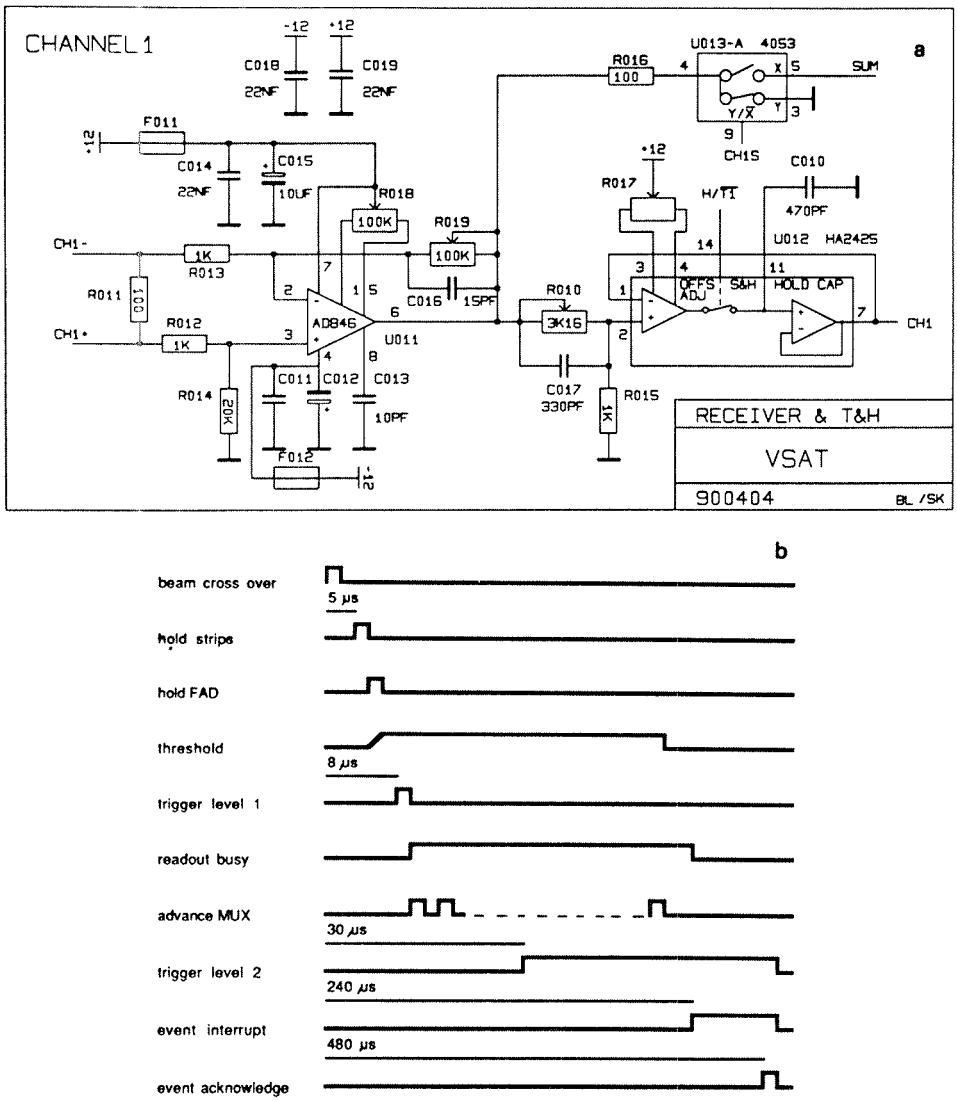

Fig. 4. (a) input stage of the MUX card. (b) Timing signals for data transfer.

to Monte Carlo simulations, is discussed in section 4. Section 5 finally gives a summary.

2. Detector layout

The choice of detector type was essentially dictated by the necessity of having a very compact detector giving very precise position measurement and good electromagnetic shower containment within the space available (25 cm along the beam pipe). The design was inspired by the electromagnetic calorimeters constructed for the LEP beam operation monitors [1] used under similar conditions. The calorimeter modules are assembled using 2 radiation lengths (r.l) of tungsten absorbers interspaced with 12 full area silicon detector (FAD) planes of dimension 30×50 mm^2 for energy measurement. Three silicon strip planes with 1 mm pitch are used to give x and y positions. The strip planes are put close to shower maximum with two x-planes at 5 and 9 r.l. depth, and one y-plane at 7 r.l. The x planes have 32 strips while the y plane has 48 strips (all strips are 1×50 mm^2). The geometry of the assembly is illustrated in fig. 2.

The 300 μm thick FAD and strip detectors were specially designed for this experiment (made by Micron Semiconductor). All planes were cut so that the active area along one 50 mm side (i.e. towards the beam pipe) is only 0.5 mm from the edge. The total thickness of board, wafer and bonding was less than 1.6 mm. The silicon–tungsten assembly is guided by two precisely machined circular rods giving an overall precision in mounting of better than 100 μm.

A weak alpha source is deposited on the tungsten plates facing the 12 FAD detectors for calibration purposes. The silicon–tungsten stack is put into a precision made box containing preamplifiers as well as temperature sensors. Optical survey, integrated with mechanical measurements, allows us to obtain a knowledge of the position of the detectors to within about 0.2 mm, by means of a best fit procedure.

3. Readout electronics

The FAD planes have a full depletion voltage of typically 30 V. The bias is furnished by individual voltage modules with individual control and monitoring of the voltages and currents. Due to the special role of FAD number 1 (X-ray monitoring) this has a separate bias supply while the other FADs share a common supply. The FADs are individually equipped with charge sensitive preamplifiers (LABEN 5243) which are well matched to the large detector capacitance (500 pF at full depletion) exploiting two bipolar devices in parallel. With 500 ns shaping time the total noise of the chain was measured to be about 60 keV rms in the laboratory. Due to various sources of noise, e.g. parasitic oscillations and pickup, this figure was increased by a factor three when mounted in the LEP tunnel.

The strip planes have a full depletion voltage of 25 V. No observable difference in noise level and dark current was observed for the y-planes which have all the strips perpendicular to the thin edge of the silicon plane as compared to the x-planes having the strips parallel to this edge. For the front end of the strips readout, a 16-channel surface mounted preamplifier (MSP16 [2]) was used. Due to the fairly fast rise time of the output signal (50 ns) an intermediate amplifying stage has been

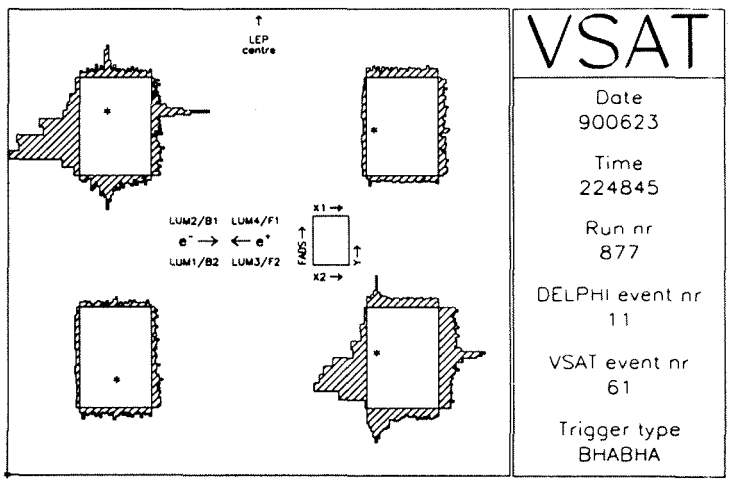

Fig. 5. Event display showing Bhabha candidate.

foreseen between these front end preamplifiers and the standard multiplexing cards (described further on) to avoid slew rate problems. The noise measured in the whole chain in the laboratory was 45 keV rms.

The readout system is shown schematically in fig. 3. Between the detector box and the digitizing electronics located 40 m away in the regular DELPHI electronics room there is an intermediate station, also located inside the LEP tunnel, for handling the signals; the preamplifier signals are transported through 3 m long cables to a crate where the signals are received and amplified with adjustable gain on multiplexing (MUX) cards. In addition to special patch cards for driving the analog signals, and for receiving the digital timing and control signals, this crate also contains a "tunnel processors" (TP [3]), a power relay containing an emergency switch, and the pulse generator used to monitor the behaviour of the readout chain for both FADs and strips.

The counting room electronics consist of a service board (PATCH CARD) to receive/drive the signals, digitizer cards (FDDP [4]) and of the overall trigger supervisor card (LTS). In the following a short description of the most important cards is given.

3.1. The multiplexor card

The 124 silicon channels from each box are distributed over eight MUX cards in the following way:
- one card for the FADS (12 channels) and temperature signals;
- four cards for the two x strip planes ($2 \times 2 \times 16$ channels);
- three cards for the y strip plane (3×16 channels).

The block diagram of the first stage of the MUX cards, shown in fig. 4a, is identical for FADs and strips. Each analog channel consists of a HARRIS 2625 receiver followed by a HARRIS 2425 sample-and-hold. The intermediate integrating and amplifying stage specially developed for the strips consists of a MOTOROLA LF357. The combined shaping time is 650 ns. The signal is then fed through a sample-and-hold (S&H) circuit to a 16-fold multiplexor. The time needed by the S&H to reach stable signals after the start command is about 400 ns, while the time needed by the multiplexor to reach stable signals after each clock is about 1 μs. The multiplexed signals are then sent to the FASTBUS patch card in the control room that, after some last amplification, feeds the signals to the digitizers.

The MUX cards used for the FADs also contain the trigger decision circuitry. The signals coming out of the receivers are sent to an analog adder (with a software remote selection, done by the TP card, of the channels that have to be added) followed by two comparators controlled by the TP providing the trigger answer for two different thresholds.

The two varieties of MUX cards require different timing signals due to the different rise times of FAD and strip signals. The timing of the control signals is generated with respect to the beam cross over reference as shown in fig. 4b. The FAD MUX cards also contain part of the logics for the alpha source trigger.

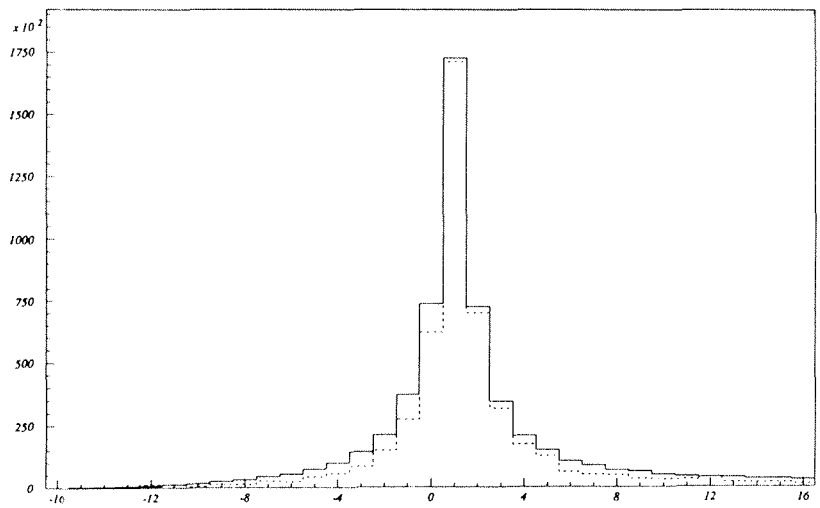

Fig. 6. Lateral widths of 45 GeV showers at 5 r.l. depth ($x1$-plane) with a comparison to Monte Carlo prediction.

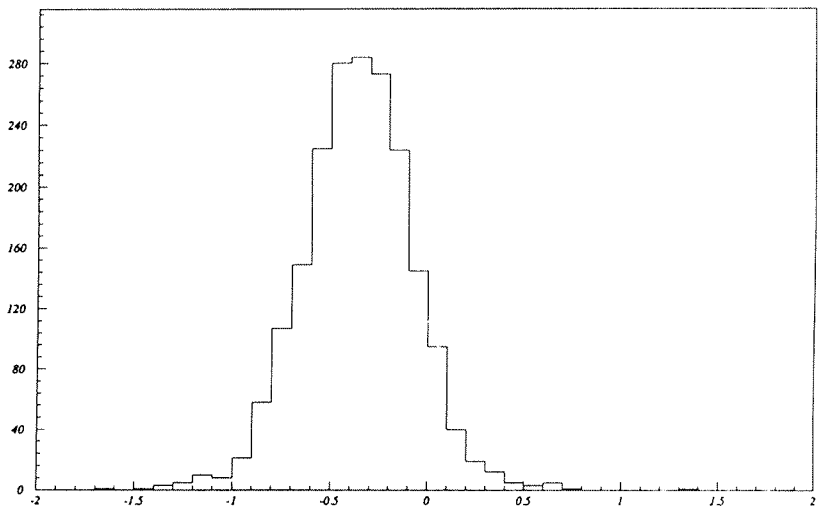

Fig. 7. Position correlation of $x1$- and $x2$-planes.

3.2. The tunnel processor

The tunnel processor, based on the Motorola 68HC11 micro-controller unit, is remotely controlled via RS232. It performs the following tasks:

- set the low and high trigger thresholds;
- select the FAD planes to be added for the analog sum;

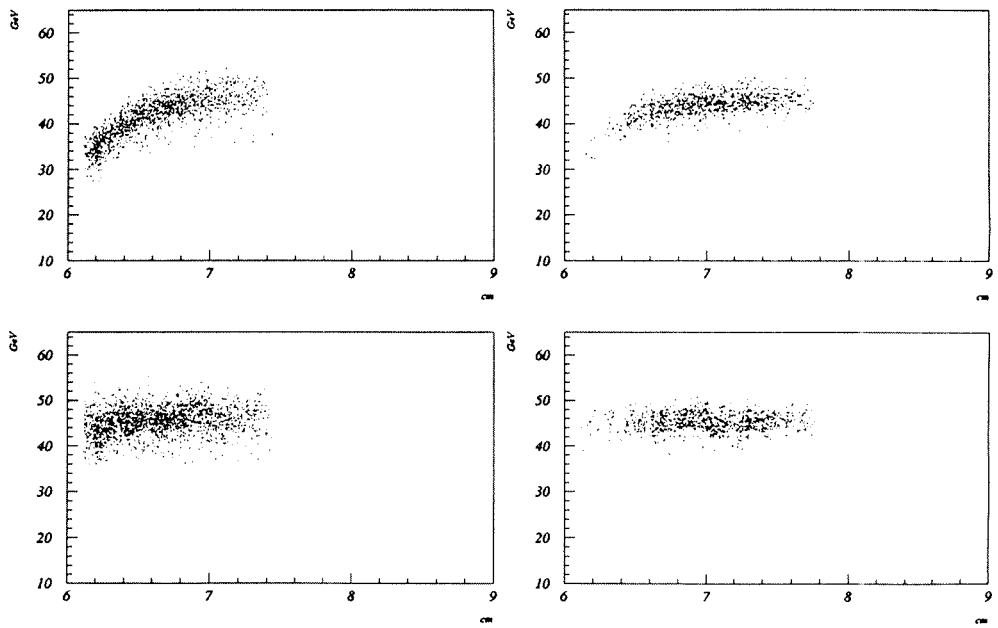

Fig. 8. Energy profiles vs x for selected Bhabha candidates before and after correction for shower leakage in outside and inside modules.

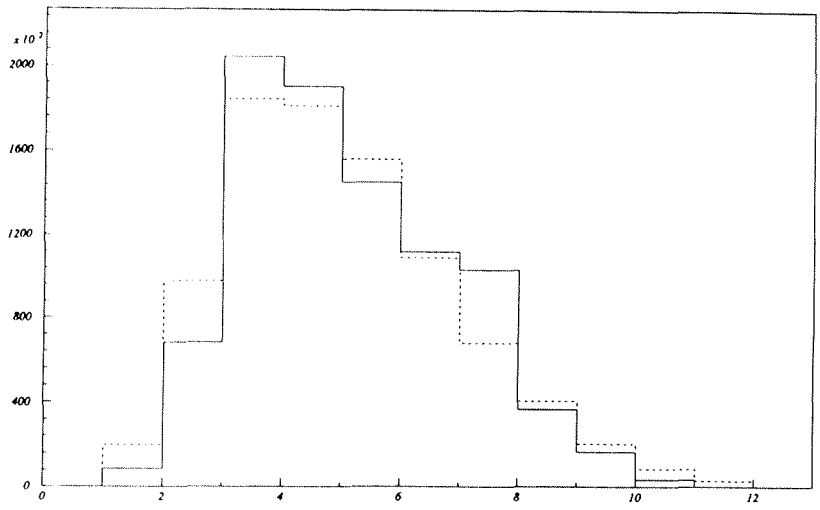

Fig. 9. Longitudinal shower profile, data compared to Monte Carlo prediction.

- monitor preamplifier and calorimeter temperatures;
- control the power supplies for the preamplifiers;
- select signal paths through the MUX;
- control the alpha trigger;
- report status;
- control of test signals.

The TP monitors and protects the silicon and their preamplifiers from overheating (they are normally cooled by a flow of nitrogen gas). If the temperature at the preamplifiers exceeds 70° a warning is issued and their power supply is shut off if no action is taken.

There is a "watchdog" circuit connected to the TP reset input which will restart the processor if not toggled regularly. All communication with the TP is in ASCII format, making the settings of parameters easy by means of an external terminal. Two modes of communication are implemented: one verbose mode and one nonverbose mode. The former is a user friendly, English type, mode for terminal communication. The latter is designed for maximum efficiency in data communication with the FASTBUS crate processor, FIP.

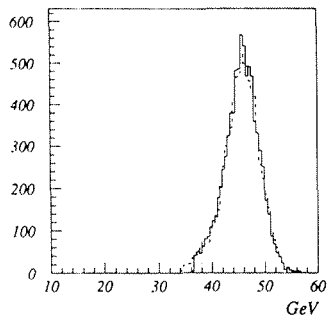

Fig. 10. The Bhabha peak, isolated with an 80% cut in energy.

3.3. The local trigger supervisor

The LTS performs the trigger decisions and provides control signals to the MUX cards (hold and reset signals to the S&H) and to the fast digital data processors (FDDP).

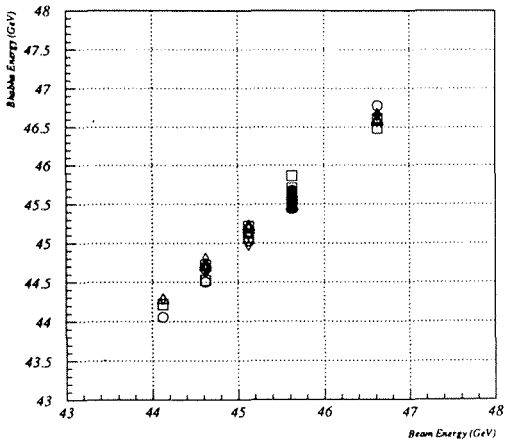

Fig. 11. The VSAT energy measurement vs the beam energy for the Z scan.

The trigger decision is based on the eight digital outputs of the four FAD MUX card comparators. There are two signals for each module, corresponding to the energy deposited in the selected FADs of the module being above the low or high selected thresholds. There are several types of "events" which can be selected by the LTS:

- *Bhabha*: the elastic scattering of electrons on positrons. This is defined as the coincidence between diagonal modules with signals above the high threshold.
- *Single electron*: an energy deposition above the low energy threshold in any of the four modules. It is recorded with a downscaling factor which can be set separately by the LTS for the modules placed inside and outside the LEP circumference.
- *Accidental Bhabha*: the coincidence between a module and its diagonal delayed by four LEP bunch crossings. The threshold conditions are the same as for "true" Bhabhas. This trigger is used for off-line subtraction of accidental coincidences in diagonal modules.
- *Testin*: the preamplifiers are pulsed with test signals of variable amplitude, shape and frequency.
- *Alpha*: the signals of the alpha particles are used for calibration and monitoring of the FADs.

Any VSAT event (including all single electrons) is accompanied by trigger information to DELPHI consisting of 2 times 2 bits giving the number of modules with the FAD sum above the low and high threshold respectively (0, 1, 2 or more than 2). This information can be used by other DELPHI subtriggers for trigger decisions, e.g. in a two-photon physics trigger with a VSAT-tagged electron.

3.4. The fast digital data processor

The fast digital data processor (FDDP) is based on a fast DSP (TMS320). It performs the analog-to-digital conversion of the multiplexed signals, sends the control signals to the multiplexors on the MUX cards, reads the digital data and writes formatted outputs on an output buffer memory. The conversion is done by an 8 bit 10 MHz FADC (Thomson 8328) for the data of the strip planes, and by a 12 bit 1 MHz ADC (Crystal CSZ5412) for the FAD data. One FDDP board reads two diagonal modules. Due to the high rate of Bhabha triggers in the VSAT compared to the normal DELPHI trigger rate, VSAT events are stored locally and the entire buffer, containing up to 20 events, is read out at each DELPHI trigger (or at a preset limit for the number of stored VSAT events forcing a DELPHI trigger).

4. Detector performance

4.1. Position measurements

The position information provided by the x and y strip planes is an essential feature of the VSAT. Fig. 5 shows an online display of a typical Bhabha event. The lateral shower profile for the $x1$-plane at 5 r.l. depth is shown in fig. 6 for 45 GeV electrons. In this figure several events are superimposed where the data of the strip with the largest pulse height has been put in the central bin. A Monte Carlo simulation using the DELPHI standard simulation program, DELSIM, gives

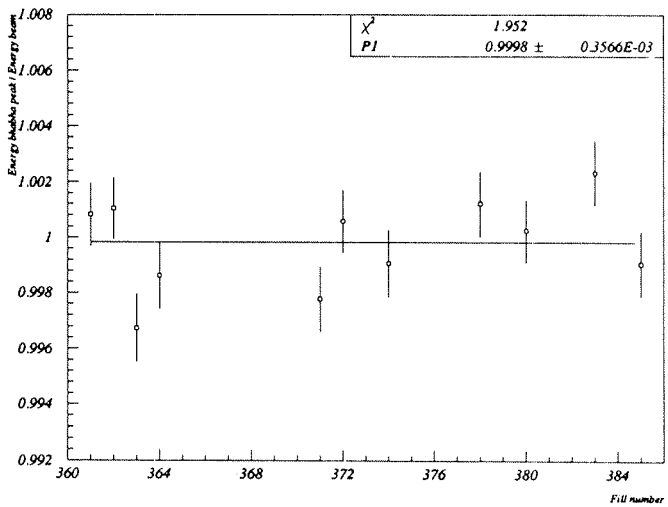

Fig. 12. Ratio of average energies measured by the modules and the beam energy.

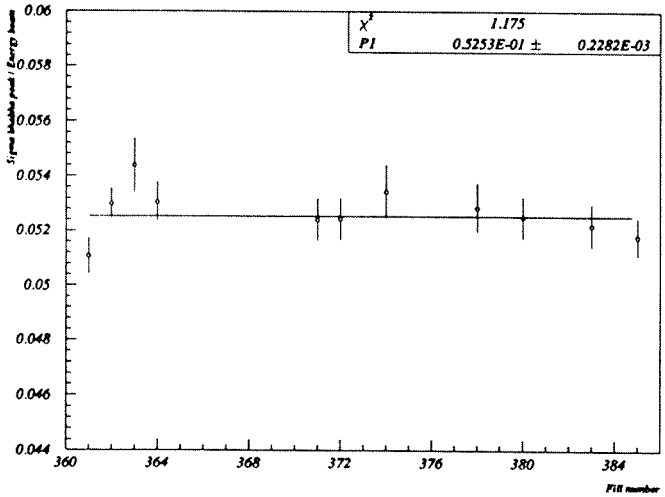

Fig. 13. Energy resolution of a calorimeter for several fills over a period of 1 month.

distributions, also shown in the figure, in reasonable agreement with data. The distributions show that the lateral spread of the shower is very narrow, as expected from the small Molière radius of tungsten. As can be seen, about two thirds of the shower is contained in the three central strips. This prompted us to use only the information of three central strips to reconstruct the shower center of gravity, which has the merit of reducing the statistical fluctuations in the tails as well as giving a good spatial resolution very close to the detector edges.

In the reconstruction the shape of the lateral profile was expressed by the sum of two exponentials as a function of the distance x from the center of the shower:

$$A(x) = a_1 \, e^{-x/b_1} + a_2 \, e^{-x/b_2}.$$

The values of the slope parameters b_1 and b_2 and of the weights a_1 and a_2 have been determined by a fit to the distributions in the three strip planes. While the a_i values change with the depth of the plane, the slopes b_i are practically constant. Best fit values are: $b_1 = 0.9$ mm, $b_2 = 4.0$ mm. In the reconstruction of the coordinates we use only one exponential term with an effective slope b and the three strips having the highest signals with the following algorithm:

$$x = x_i + b/2 \ln(A_i + 1/A_{i-1}),$$

where x_i is the location of the central strip and A_{i+1}, A_{i-1} are the signal amplitides of the neighbouring strips. The value of the slope parameter b_i is different for the three planes and is also dependent on the position in the strip. The resolution in position reconstruction has been checked by comparing the x values of the two x-strip planes. In fig. 7 the difference in reconstructed x-positions from $x1$ and $x2$ is given in cm (the effect of the nonzero angle of incidence for the electron has been removed), from which we can infer a position reconstruction accuracy of 200 μm.

The relative strip calibration was done both using test pulses and the signals of 45 GeV electrons. The information in the x strips is used both to eliminate events with showers at the very edges of the detector – where the first strip has the largest pulse height – and to extract the center of the shower to correct for lateral shower leakage. This is shown in fig. 8, where the energy distribution of Bhabha events, selected with the procedure explained below, is plotted vs x for outside

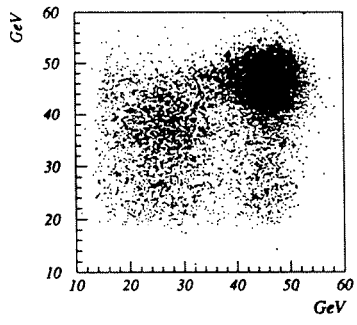

Fig. 14. Scatter plot showing the energy correlation of the two diagonal modules.

and inside (with respect to LEP) modules, before and after the shower leakage correction.

4.2. The energy measurements

Information on the signal amplitudes of the FAD planes are used to select Bhabha events on the basis of the total energy deposited in diagonal modules, both at the trigger level and in the subsequent off-line analysis. Relative calibration of the FADs is obtained from the alpha source signals while absolute calibration was done using 45 GeV electrons from Bhabha events selected with the procedure described in section 4.3.

Typical longitudinal shower profiles for selected Bhabha events are shown in fig. 9 while total energy, corrected for edge effects as explained above, is shown in fig. 10. Both figures also show Monte Carlo simulation results obtained by the DELSIM program. For the same events the energy resolution is 5% or $35\%/\sqrt{E}$, which agrees with the Monte Carlo predictions for the detector geometry (the theoretical value for fully contained showers is about $28\%/\sqrt{E}$). During the LEP

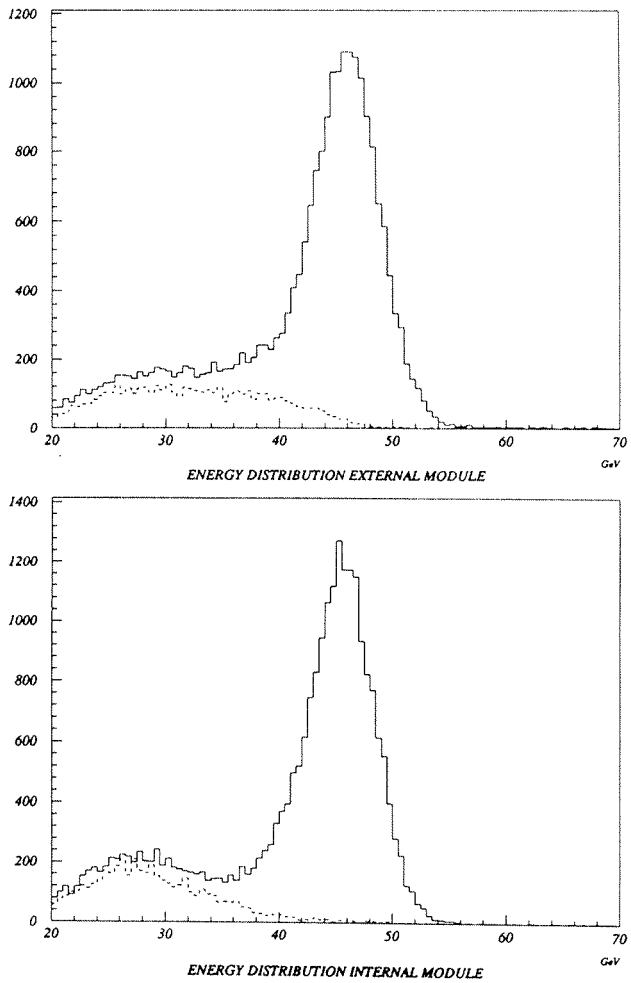

Fig. 15. Energy distributions in an inside and an outside module of Bhabha triggers (histogram) and false Bhabha triggers (shaded) before off-line Bhabha selection.

energy scan over the Z-peak the calorimeter modules could reproduce the beam energy to great accuracy as shown in fig. 11. Here the central total energy values of the Bhabha peaks for the four modules and several LEP fills are superimposed. The ratios of the average VSAT measured energies to the beam energies are shown in fig. 12. The distribution shows that the VSAT modules measure the LEP energy to within 0.5%. Fig. 13 shows the width of the energy distributions normalized to the beam energy. As one can see the energy resolution is stable over long periods.

4.3. Bhabha trigger selection

Typical energy distributions for a pair of diagonal modules during an LEP fill are shown in fig. 14. A clear accumulation of events around the beam energy is visible, due to Bhabha events. The low energy tails are mainly due to accidental coincidences of background electrons. The spectrum and rate of the off momentum electrons are different in the modules which are inside the LEP ring (modules F1 and B1) and outside (modules F2 and B2). In the inside modules the rate is lower and the spectrum is softer. Background spectra are shown dashed in fig. 15. They are obtained by analyzing with the same selection criteria the sample of accidental Bhabha events described above, in which the electron (positron) in the innner module is set in coincidence with a positron (electron) hitting the outer module after four beam-cross-overs when the same bunches are back at the DELPHI intersection. A simple cut in energy, set at 80% of the beam energy, is sufficient to drastically reduce this beam background. The small remaining background, about 2% of accidental Bhabha coincidences, is continually monitored and subtracted using the delayed Bhabha sample.

5. Summary

The VSAT detector has demonstrated that electomagnetic calorimetry using a stack of silicon–tungsten is very promising, and that a high degree of stability can be achieved in the operation of such a detector. The high density of tungsten, together with fine longitudinal and transverse granularity provides the precise energy and space resolution which is required for monitoring the LEP beam background and the measuring the DELPHI luminosity. Results of luminosity measurements and beam monitoring will be discussed in future papers.

Acknowledgements

This project was inspired by the work done for the LEP Machine by G. von Holtey and F. LeMeilleur and their help and advise have been of great importance to us. Thanks are also due to C. Wilburn and P. Jarron for constructive help in setting up the silicon detectors. The intelligent contributions of F. Bertolino, D. Crosetto, S. Kack and Z. Zhengang are warmly acknowledged. Finally the support of the INFN and the Research Council in Sweden is acknowledged.

References

[1] J.Y. Hemery, F. Lemeilleur and G. von Holtey, An interaction rate monitor for LEP, LEP-BI/86-5.
[2] G.P. Ferri et al., CERN/ECP 90-8.
[3] H. Carling, The VSAT tunnel processor, LUNDF6(NFFL-7058) (1990).
[4] F. Bertolino et al, IEEE Trans. on Nucl. Sci. NS-36 (1989) 1469.

DELPHI Collaboration

DELPHI 93-127 PHYS 342

11 October, 1993

Two-photon physics at DELPHI

J. Bjarne
Department of physics, University of Lund,
Sölvegatan 14, S-223 62 Lund, Sweden

Abstract

Results are presented from analyses of multi-hadronic two-photon data obtained with the DELPHI detector at LEP. Single-tagged events having medium-to-high momentum transfers (Q^2) are shown to be well described by a VDM+QPM model. Studying very low Q^2 single-tagged events, it is shown for the first time that a full VDM+QPM+QCD model is required in order to describe the data. The need for perturbative QCD processes is confirmed from a low Q^2 untagged event study. These events have also been used comparing different parton density functions.

Presented at the "HEP 93" Conference
Marseille, 22-24 July 1993

Two-Photon Physics at DELPHI

J. BJARNE*
Department of Physics, University of Lund,
Sölvegatan 14, S-223 62 Lund, Sweden

ABSTRACT

Results are presented from analyses of multi-hadronic two-photon data obtained with the DELPHI detector at LEP. Single-tagged events having medium-to-high momentum transfers (Q^2) are shown to be well described by a VDM+QPM model. Studying very low Q^2 single-tagged events, it is shown for the first time that a full VDM+QPM+QCD model is required in order to describe the data. The need for perturbative QCD processes is confirmed from a low Q^2 untagged event study. These events have also been used for comparing different parton density functions.

The DELPHI detector at LEP [1] has been used to study two-photon processes ($e^+e^- \rightarrow e^+e^- + hadrons$) at center-of-mass energies $\simeq$ 90 GeV. Main results from studying single-tagged and untagged data are presented.

The two outgoing electrons are mainly scattered into small polar angles θ. Electromagnetic calorimeters in the forward direction (FEMC, SAT and VSAT) were used to detect one of these for the single-tagged studies. The untagged events were required to have no electron in either the FEMC or the SAT. Some main characteristics of the different event samples are given below.

Tagger	θ [mrad]	$< Q^2 >$ [GeV$^2/c^4$]	#ev.
FEMC	175 - 637	80	80
SAT	43 - 135	12	300
VSAT	5 - 13	0.07	520
Untagged	< 43	0.12	18300

Event triggering was based on detection of charged tracks in the forward region. A trigger efficiency of more than 95% was estimated by using simulated data and single charged track efficiencies.

A charged track was accepted if it had momentum >0.4 GeV/c, polar angle >20 degrees, radial impact parameter <4 cm and longitudinal impact parameter <10 cm. An untagged event was accepted if it had $\geq$4 charged tracks, charged hadronic energy <12 GeV, total hadronic energy <20 GeV, invariant mass between 3 and 12 GeV/c^2 and total net charge $\leq$2. The same cuts were used for the single-tagged cases, except that $\geq$3 charged tracks were required with tag energy $\geq$20 GeV (VSAT), $\geq$25 GeV (FEMC) and $\geq$30 GeV (SAT).

The background to the two-photon events was studied by Monte Carlo simulations (Z^0 and τ decays), by events not originating from the vertex (beam-gas collisions) and, for the VSAT-tagged case, by calculating the probability of purely statistical coincidences. The event backgrounds to the different single-tagged and untagged cases were estimated to be $\leq$6%.

Monte Carlo simulations were performed using the TWOGAM two-photon event generator [2], JETSET7.3 fragmentation package and DELPHI-specific detector simulation and reconstruction software. Different parton density parametrisations [3] were studied for the VSAT-tagged and untagged cases.

The high and medium Q^2 FEMC- and SAT-tagged two-photon events are found to be fully described by a sum of VDM and QPM models [4]. There is no need for perturbative QCD processes in these cases.

VSAT-tagged events show for the first time the need for perturbative QCD processes in order to describe very low Q^2 single-tagged two-photon data [5]. The visible invariant mass spectrum indicates a perturbative QCD dominance above 5 GeV/c^2 (Figure 1).

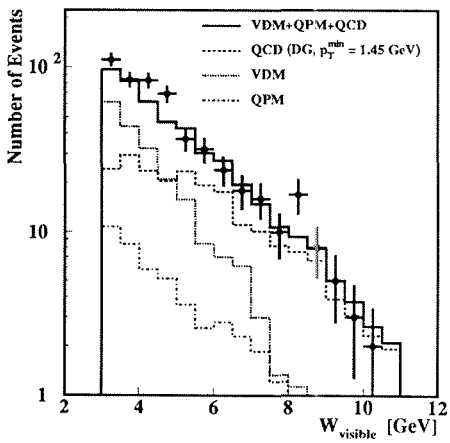

Figure 1: VSAT-tagged visible invariant mass.

*Representing the DELPHI Collaboration.

The dominance of QCD hard scattering processes can also be clearly seen for beam-normalised VSAT tag energies below 0.8 (Figure 2).

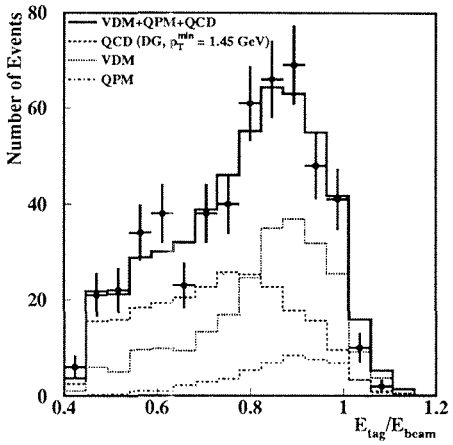

Figure 2: Beam-normalised VSAT tag energy.

Untagged data also show the need for perturbative QCD processes [6], these becoming dominant in the upper tail of the jet p_T distribution. This region was examined by selecting events having at least two jets, each with p_T >1.75 GeV/c and polar angle between 40 and 140 degrees. Four different parton density functions were tried for describing the data, and Figure 3 shows the jet high-p_T regions for these together with data. Here the p_T^{min} value (the minimum parton p_T required for the QCD generator to be included) is set individually for each density function in order to fit the visible cross section. It is clear that the Gordon-Storrow (GS, p_T^{min} = 1.83 GeV/c) and Levy-Abramowicz-Charchula set 1 (LAC1, p_T^{min} = 2.22 GeV/c) parton density functions describe the data better than the Duke-Owens (DO, p_T^{min} = 1.22 GeV/c) and Drees-Grassie (DG, p_T^{min} = 1.45 GeV/c) parton density functions. However, the VSAT-tagged data agrees well with DG (Figures 1-2) as well as some other parametrisations.

Work is currently in progress in order to expand the analyses described here. Values of the photon structure function F_2^γ may be obtained by unfolding the FEMC- and SAT-tagged data. Preliminary results show that by applying simple cuts in the VSAT-tagged $W_{visible}$ *vs.* E_{tag}/E_{beam} plane a clean QCD-dominated sample can be isolated. This potential will be used for further perturbative QCD studies, where comparing different parton density functions are of prime interest. Both untagged and VSAT-tagged data will also be used for studying central and remnant jets.

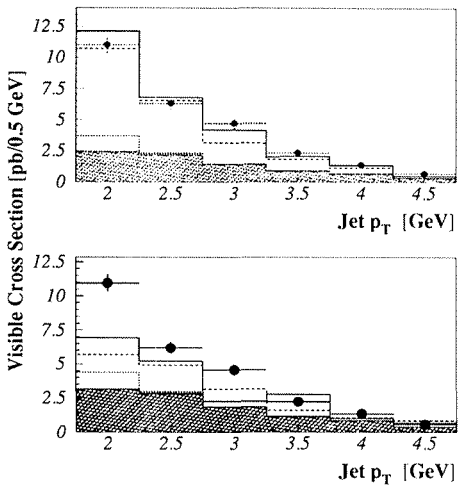

Figure 3: Data and Monte Carlo simulations of the jet high-p_T sample. Hatched area = QPM only, dotted line = QPM+VDM. Upper picture: dashed line = QPM+VDM+QCD (LAC1, p_T^{min} = 2.22 GeV/c), solid line = QPM+VDM+QCD (GS, p_T^{min} = 1.83 GeV/c). Lower picture: dashed line = QPM+VDM+QCD (DO, p_T^{min} = 1.22 GeV/c), solid line = QPM+VDM+QCD (DG, p_T^{min} = 1.45 GeV/c).

References

[1] DELPHI Collaboration,
The DELPHI detector at LEP,
Nucl. Instr. and Meth. **A303**(1991)233

[2] S. Nova, A. Olshevski, T. Todorov,
Monte Carlo Event Generator for two Photon Physics,
DELPHI 90-35 PROG 152 (1990)

[3] H. Plothow-Besch,
PDFLIB: A Library of all available Parton Density Functions of the Nucleon, the Pion and the Photon and the corresponding α_s Calculations,
CERN-PPE/92-123 (1992)

[4] B. Batyunya *et al.*,
Study of single tagged multihadronic $\gamma\gamma^*$ events at a $< Q^2 > \simeq$ 12 GeV$^2/c^4$,
DELPHI 93-60 PHYS 288 (1993)

[5] J. Bjarne *et al.*,
First evidence of hard scattering processes in very low Q^2 single tagged $\gamma\gamma$ collisions using the DELPHI VSAT detector,
DELPHI 93-90 PHYS 317 (1993)

[6] DELPHI Collaboration,
Study of hard scattering processes in multihadronic $\gamma\gamma$ collisions at LEP,
DELPHI 93-89 PHYS 316 (1993)

June 21, 1994

First Evidence of Hard Scattering Processes in Single Tagged $\gamma\gamma$ Collisions

Abstract

For the first time, multihadronic production from single tagged $\gamma\gamma$ collisions has been studied, where one of the scattered leptons was tagged at very low momentum transfer ($< Q^2 >= 0.06$ (GeV/c^2)^2). Data collected during 1991 and 1992 in the DELPHI experiment at LEP are shown to agree well with Monte Carlo predictions. The Monte Carlo programs used included a vector meson dominance model in which the interacting photon is assumed to have converted into a vector meson (ρ, ω or ϕ), a quark-parton model which describes direct photon interactions and a QCD-based model which considers the photon to have quark and gluon structure functions. Five different parametrizations of these structure functions were used and the predictions compared with the data. This study confirms recent results from no-tag experiments in requiring a QCD-based component to successfully describe the data, indicating that the photon has a significant partonic content.

(To be submitted to Phys. Lett. B)

1 Introduction

Two-photon scattering in e^+e^- storage rings has been studied in many experiments at PEP [1], PETRA [2], more recently at KEK [3] and LEP [4]- [7]. The production of multihadronic final states, X, in the reaction $e^+e^- \to e^+e^-X$ is possible due to collisions of the clouds of virtual photons radiated by high energetic electrons and positrons. If both the scattered electron and positron go down the beam pipe and remain undetected, the "no-tag" or "untagged" mode, only the multihadronic system can be studied. In "single tagged" and "double tagged" cases one or both of the outgoing scattered leptons are measured respectively. The detected lepton provides additional information about the event kinematics, allowing more detailed studies of such events to be made than is possible with untagged events. Unfortunately, as the scattered leptons emerge preferentially along the beam direction, requiring that one or both leptons be scattered at a large enough angle to be detected results in a large suppression of the $\gamma\gamma$ cross-section compared with the untagged case. A review of two-photon physics may be found in ref. [8] and recent reports of work in this field may be found in ref. [9]. Interesting results were reported there by AMY [10] for no-tag experimental conditions giving the first satisfactory qualitative description of data by including QCD-based calculations of a hard scattering of hadronic constituents of the photon.

Here, first evidence of hard scattering subprocesses in single tagged $\gamma\gamma$ events at LEP energies is reported and a comparison is made between the data and five different parton density parametrizations used to describe those subprocesses. Data taken with the DELPHI detector during 1991 and 1992, corresponding to an integrated luminosity of 28.4 pb^{-1}, were used to analyze the hadronic final states produced in single tagged $\gamma\gamma$ collisions at a mean value of the photon absolute squared mass, Q^2, around 0.06 $(\mathrm{GeV}/c^2)^2$.

The paper is organized in the following way. Section 2 gives a brief overview of the theory of $\gamma\gamma$ interactions, with emphasis on the three models used for describing the data. Then the implementation of the $\gamma\gamma$ theory in Monte Carlo simulations is described. The DELPHI detector components and the methods used for $\gamma\gamma$ event selection are described briefly in Section 3. The detector for luminosity measurement, the Very Small Angle Tagger (VSAT), used here to tag the scattered leptons, is described in more detail. Section 4 deals with the rejection of background to the $\gamma\gamma$ events and the results are discussed in Section 5.

2 Theoretical framework and simulation

The overall kinematics of a single tagged $\gamma\gamma$ reaction is represented in Figure 1a. The four-momentum transfer $Q^2 = -q_1^2$ is defined as the absolute value of the squared mass of the virtual photon radiated from the tagged electron or positron. In the high Q^2 region the $e\gamma$ Deep Inelastic Scattering (DIS) formalism applies with a quasi-real photon as the target, coupling to quarks in a point-like fashion or through a vector meson bound state (see for example [4]). At moderate x ($x =$

$Q^2/(Q^2+W^2)$ where W is the invariant mass of the produced hadronic system) the data from previous e^+e^- collider experiments are in qualitative agreement with a composite model combining the Vector meson Dominance Model (VDM) and the Quark Parton Model (QPM), illustrated in Figures 1b and 1c. The photon structure function is then extracted from the data using unfolding methods [4] . The theoretical description of the low x region is still not fully satisfactory. An excess of events over the incoherent sum of the expectations from the VDM and QPM was observed experimentally [1]- [3] It was also observed that a significant fraction of those events did not have the simple two-jet topology expected from the model. Recent QCD-based calculations of non-diffractive hard-scattering of hadronic constituents of the photons have shown that high transverse momentum hadrons could be produced in multi-jet configurations [11,12]. In this low x region jets are produced with high transverse momentum (p_T) with respect to the $\gamma\gamma$ axis (usually very close to the beam axis for the single tag case) which implies high $\gamma\gamma$ invariant masses W.

Going to low Q^2, jet production with p_T^2 greater than Q^2 is expected to be more frequent. In the Leading Log approximation of QCD, the hard scattering subprocesses shown in Figures 1d and 1e start to grow, even to dominate when going to very low Q^2. In these subprocesses, called sometimes QCD Resolved Photon Contribution (hereafter denoted QCD-RPC), some partons within the photons can interact with each other. Therefore, a density function formalism is appropriate to express the chance of finding a parton in the photon with given momentum fraction. These QCD-RPC subprocesses offer the possibility of experimentally measuring the quark and gluon densities of the photon [3,4] and hence verifying the theoretical calculations. The hard scattering subprocesses shown in Figures 1d and 1e require high four-momentum transfers (or high p_T^2) of partons to probe the structure of one or both photons and to resolve them into their partonic constituents.

So the scheme used to describe $\gamma\gamma$ process can be represented as follows. The fully non-perturbative term is described through VDM as the diffractive scattering of vector mesons with the cross-section given by [13]

$$\sigma_{\gamma\gamma}(W^2,Q^2,P^2) = F_{VDM}(Q^2)F_{VDM}(P^2)\left[A+\frac{B}{W}\right] \tag{1}$$

where W is the invariant mass of the $\gamma\gamma$ system while Q^2 and P^2 are the absolute squared masses of the two virtual photons. The values $A = 275$ nb and $B = 300$ nb·GeV/c^2 were used [14], which are about 10% larger than those in the standard Rosner formula [13]. This type of parametrization has already been used by previous experiments [2,3].

The quantity F_{VDM} is the generalized VDM form factor [15]

$$F_{VDM}(Q^2) = \sum_{V=\rho,\omega,\phi} r_V \frac{1+Q^2/4m_V^2}{(1+Q^2/m_V^2)^2} + \frac{0.22}{1+Q^2/m_0^2} \tag{2}$$

with $m_0 = 1.4$ GeV/c^2 and where m_V denotes a vector meson mass and r_V is related to the vector meson coupling to the photon. The last term describes the contribution

from the radial excitations of vector mesons. The multihadronic final state was generated from a $q\bar{q}$ pair, with a limited-p_T quark distribution $d\sigma/dp_T^2 \simeq \exp(-5p_T^2)$ in the $\gamma\gamma$ centre-of-mass system using PLUTO tuned parameter [2].

The other contributions are treated using leading order QCD factorization: a hard scattering subprocess gives the dominant scale p_T^2, taken also as the factorization scale. The photon participates by direct coupling to quarks or to a quark or a gluon produced through a QCD evolution starting from a bound state or to a perturbative $q\bar{q}$ pair state. According to the Drees classification [11] there are three terms: the direct term of Figure 1c (a QPM generator was used to describe this interaction term, analogous to the QED process $ee \to ee\mu\mu$), the singly-resolved photon contribution of Figure 1d and the doubly-resolved photon contribution of Figure 1e (both of which were described by the QCD-RPC model). Since the hard scattering subprocesses are considered as perturbative within QCD-RPC, a cut, p_T^{min}, on the transverse momentum of the outgoing partons has to be specified in order to separate them from the non-perturbative contribution and avoid double counting. Unfortunately, there is still no model which completely removes this problem. As mentioned above, the quarks and gluons are emitted from a photon through QCD evolution, starting from either a point-like or a bound state coupling. Total separation implies the use of another quark transfer cut-off (p_T^0) [16] at the first quark pair creation level. Since the existing quark and gluon parametrizations do not allow such a distinction, in the present study the outgoing partons are assumed to participate in high-p_T jet production, while the spectator partons produce remnant jets. The latter were generated along the direction of the incoming quasi-real photons.

In the present study it was found that values of p_T greater than 1.5 GeV/c were suitable, *i.e.* much larger than the magnitude of the mass of the virtual photons. Within the QCD-RPC model, the p_T^2 of the outgoing partons of the hard scattering subprocess in multi-jet production (which is always greater than a required minimum value $(p_T^{min})^2$) probes the structure of one photon in singly resolved processes, or both photons in doubly resolved processes [17]. In this approach the two photons need to be considered as quasi-real.

So in general, the main features of two-photon mechanism described are the following. Most secondary particles from the $\gamma\gamma$ events are produced at small polar angles, and only some of the particles of the final system are actually detected. The resolved photons produce "remnant" or "beam-pipe" jets, which may mix with decay products of the low-p_T central system. The presence of jets of (moderately) high p_T at large angles forms a signature for the isolation of the hard scattering subprocesses from the dominant diffractive dissociation contribution.

Many partonic density functions of the photon are available, but since they are extracted from deep inelastic $e\gamma$ scattering at high Q^2 they cannot always be used to describe hard scattering process at relatively low $(p_T/c)^2$. Only leading order parametrizations have been considered here. *A priori* each of these parametrizations is associated with a specific value of p_T^{min}, constrained by the description of the visible total cross-section and can be tested directly against the data. This approach, as shown below, indicates the distinctive requirements for a successful parametrization. In particular, hard parton distributions will produce more high-p_T jets in the central

region while soft distributions lead to more energy deposition in the remnant jets.

These three models were implemented in the TWOGAM generator [18] used for generating $\gamma\gamma$ events, requiring one lepton to be scattered towards the VSAT polar angle region (see Section 3). No selection was applied to the other lepton, since it mainly goes inside the beam pipe. The generated events were then fragmented using the JETSET 7.3 [19] model. In the simulation of the VDM model, the JETSET parameter σ_q, describing the dispersion of the transverse distribution of primary hadrons within a jet, was set to 450 MeV/c in order to take into account the bound-state origin of the quarks [20].

To take into account the influence of the magnetic field of DELPHI and superconducting quadrupoles on the scattered leptons, specially developed programs [21] were used for fast selection of events with a lepton hitting a VSAT module, as well as for simulating and reconstructing the resulting VSAT response. These programs have been extensively used in VSAT luminosity studies. The hadronic parts of the events were simulated and reconstructed by standard DELPHI programs.

Simulations were performed separately for the VDM, QPM and QCD-RPC processes. Five parametrizations of the parton density function of the photon were chosen for simulation [22]: the Gordon-Storrow (GS) [23] model, the Drees-Grassie (DG) [17] model, the Duke-Owens (DO) [24] model and two of the Levy-Abramowicz-Charchula models(LAC1 and LAC3) [12].

In this analysis, the Q^2 range measured by the VSAT is very small (much lower, than the p_T^2 of the jets) so that the simulation can be made as for a no-tag case. This is indeed the case for VSAT tagging conditions, since the average absolute squared mass is of the order of 0.1 $(\mathrm{GeV}/c^2)^2$, much lower than $(p_T^{min}/c)^2$ which is above 2 $(\mathrm{GeV}/c^2)^2$.

This would not be true for Q^2 values around 1 $(\mathrm{GeV}/c^2)^2$ since there is still no theoretical description of $\gamma\gamma$ collisions in the region where Q^2 and p_T^2 are of the same order. The total cross-section could, in principle, be unfolded from the data with the great advantage that the uncertainty in the VDM form factor extrapolation will be small. Other features of the tagging are useful: the tagged lepton energy gives some additional information about the production mechanisms, the data sample is free from Z^0 contamination and it becomes possible to study and reject most of the LEP machine background.

3 Apparatus and Event Selection

A detailed description of the DELPHI detector can be found in ref. [25]. Only the DELPHI components relevant to the $\gamma\gamma$ event analysis (charged particle tracking and electromagnetic calorimetry) are briefly described here. The VSAT sub-detector [26] is described here somewhat more thoroughly.

A right-handed coordinate system is used in this paper. The z-axis lies along the electron beam direction and the y-axis is defined to point vertically upwards. The polar angle θ is measured with respect to the z-axis, and the azimuthal angle ϕ is measured with respect to the horizontal plane. Charged particle tracks are measured

in a 1.2 T magnetic field by three cylindrical tracking chambers: the Inner Detector (ID), covering polar angle from 30° to 150° at radii 12 to 28 cm, the Time Projection Chamber (TPC), the main tracking device, covering polar angles from 20° to 160° and radii between 35 and 111 cm and the Outer Detector (OD) covering polar angles from 43° to 137° at radii between 198 and 206 cm. Using the ID, TPC and OD, the momentum resolution is $\sigma(p)/p = 0.0015p$ where p is expressed in GeV/c.

Tracking in the forward ($11° < \theta < 33°$) and backward ($147° < \theta < 169°$) regions is performed by two pairs of Forward drift Chambers (FCA and FCB) in the end-caps.

Electromagnetic energy is measured in the barrel region by the High density Projection Chamber (HPC) and in the forward and backward regions by a Forward Electro-Magnetic Calorimeter (FEMC), consisting of 4522 lead-glass blocks in each end-cap and covering the polar angular regions $10° < \theta < 36.5°$ and $143.5° < \theta < 170°$. The angular resolution of the FEMC, as measured for 45 GeV electrons, is 0.3°. The HPC has nine layers of lead and gas covering polar angles from 43° to 137° and radii between 208 and 260 cm.

Hadron shower energies are measured by combining the measurements from the HAdron Calorimeter (HAC) covering polar angles from 10° to 170°, and electromagnetic calorimeters.

The Very Small Angle Tagger (VSAT) is the fundamental tool in this analysis, as it is used to tag the scattered lepton from the $\gamma\gamma$ interactions. The VSAT consists of four rectangular electromagnetic calorimeter modules each of them 5 cm high, 3 cm wide and 24 radiation lengths deep. The modules consist of 12 tungsten absorbers, each two radiation lengths thick, interspaced with 12 energy sampling silicon planes, giving an energy resolution of $35\%/\sqrt{E}$. Three silicon-strip planes are placed around the longitudinal maximum of the electromagnetic showers (between five to nine radiation lengths inside the modules), two measuring the horizontal position and one the vertical position. Each strip is 1 mm wide, giving a reconstructed position resolution of 200 μm. The four modules are placed horizontally on both sides of the beam pipe at ± 7.7 m along the beam axis from the DELPHI interaction point. At this point the beam pipe changes from a cylindrical diameter of 16 cm to an elliptical form of 16 cm vertically by 12 cm horizontally. The modules are placed after the LEP superconducting quadrupole magnets, resulting in scattered leptons being focused vertically and defocused horizontally. The magnitude of this effect is inversely proportional to the lepton energy, resulting in a VSAT polar angle coverage from 5 to 13 mrad for the $\gamma\gamma$ case .

The quality of the event triggering system is very important in $\gamma\gamma$ data taking due to the low multiplicity of the final state, the low particle momenta and the particles mainly being boosted into low polar angles. The VSAT takes no part in the event triggering, which is done entirely on the hadronic part of the $\gamma\gamma$ events. The main component of the barrel part of the trigger for this analysis is the coincidence of ID and OD signals, while the forward trigger is based on the coincidence of signals from the FCA, FCB and TPC sub-triggers. The component from neutral particles contributes negligibly to the $\gamma\gamma$ trigger rate.

Because of the forward-boosted shape of the $\gamma\gamma$ events the most important part of

the event triggering is performed by the forward trigger. Information on all trigger components was recorded for the $\gamma\gamma$ events in order to test the forward trigger performance. The single-track efficiency was then calculated from the redundancy of the independent triggers, leading to a trigger efficiency of more than 95% for the final $\gamma\gamma$ event sample, selected as described below.

The multiplicity and energy of charged particles formed the basic criteria for selecting $\gamma\gamma$ hadronic events. Charged particles were accepted if the following criteria were met:

- momentum larger than 0.4 GeV/c;
- polar angle from 20° to 160°;
- radial projection of the impact parameter relative to the interaction point less than 4 cm;
- projection of the impact parameter along the beam direction less than 10 cm;
- relative error on momentum measurement less than 100%.

All calorimetric information was included in the event selection to reject the background from Z^0 decays. Taking into account the sensitivity, stability and noise performance of the calorimeters, the following minimum-energy thresholds were chosen: 0.5 GeV for the FEMC and HPC neutral clusters, and 1.5 GeV for unlinked calorimetric showers of reconstructed energy in the HAC.

The following criteria were used for the selection of $\gamma\gamma$ events, concerning the hadronic system :

(a) at least three charged particles in the event;
(b) total energy of the charged particles less than 12 GeV;
(c) total visible energy less than 20 GeV;
(d) invariant mass in the range between 3 and 11 GeV;
(e) net charge not more than 2;
(f) thrust value less than 0.999,

and concerning the tagged lepton :

(g) VSAT measured energy larger than 20 GeV;
(h) VSAT (θ, ϕ)-position reconstructed.

Criterion (a) selects hadronic final states, while criteria (b), (c) and the upper limit of (d) suppress Z^0 decay background. The lower limit of criterion (d) suppresses the resonance region of the $\gamma\gamma$ interaction and, together with criteria (e) and (g), the beam-gas background. Criterion (f) rejects the bulk of τ pairs from $\gamma\gamma$ collisions leaving a negligible remaining contribution. Criteria (g) and (h) select well-measured leptons with very low Q^2.

4 Background Rejection

The background to the VSAT-tagged $\gamma\gamma$ events comes from purely random coincidences between two independent events: an off-momentum beam electron hitting a VSAT module and some other physical event producing a hadronic system in the DELPHI detector. The probability of such coincident, but independent, events is given by the product of the individual probabilities of accepting off-momentum elec-

trons in the VSAT and hadronic systems in DELPHI. The hadronic system mainly comes from untagged $\gamma\gamma$ events, *i.e.* an event with both the scattered electrons going undetected into the beam pipe. Also the decays of Z^0, especially those involving τ particles as well as beam-gas interactions also contribute to the background, though to a much smaller degree.

The probability of accepting off-momentum electrons in the VSAT was estimated by studying a specially selected hadronic Z^0 event sample with a strong signal in DELPHI (*i.e.* events having many charged particles, high invariant mass and large energy deposition). According to simulation such events should have given no signals in the VSAT but some were found in the data. The dominant part of this background, 86%, occurred in the two VSAT modules on the outer side of the LEP ring. The results are shown in Figure 2, which shows the VSAT distributions for these off-momentum events in a) azimuthal angle ϕ, b) polar angle θ and c) beam normalized energy. The different energy spectra for the VSAT inner and outer modules correspond to different off-momentum beam components of the LEP machine. The distributions for the outer modules are narrower than for the inner modules, especially for ϕ. This fact was used to introduce cuts on ϕ of the outer modules 2 and 4 ($-0.30 < \phi_2 < 0.14$ and $-0.38 < \phi_4 < 0.14$) in order to reject the majority of the off-momentum electrons. No cut was applied for the inner modules. The ϕ selection rejects 66% of all the incident off-momentum electrons.

The final probability of purely random coincidence events passing all the single tagged $\gamma\gamma$ event selection criteria corresponds to a background level of 3.8% in the final $\gamma\gamma$ event sample.

5 Results

Only simulated events (using the VDM, QPM and QCD-RPC models) which passed all the selection criteria described above were used in order to understand the kinematics of the VSAT tagged $\gamma\gamma$ events. Figure 3a shows the absolute masses of the tagged ($Q^2 = -q_1^2$) and the untagged ($P^2 = -q_2^2$) photons (see also Figure 1a). P^2 is strongly peaked towards very low values since the untagged leptons generally go into the beam pipe. Q^2 for the VSAT tagged events is very small ($< Q^2 >=0.06$ (GeV/c^2)^2), but still much larger than P^2. There is no significant difference between the generated and reconstructed Q^2 distributions.

The remaining part of this section deals with comparisons between data and full simulation. The final data sample consists of 491 events.

The events of QCD-RPC models were generated with p_T^{min} values initially lower than the final ones (see Table 1). These final values were defined by the requirement that the total VDM+QPM+(QCD-RPC) simulation reproduce the observed number of data events. The VDM contribution was allowed to vary by $\pm$ 10% in comparison with the "standard" one defined by formula (1). This was done in order to estimate the variance of the p_T^{min} values due to the influence of the VDM cross-section uncertainty. From Table 1 it can be seen that the variation of p_T^{min} with the VDM contribution is rather smooth for all the parametrizations used and also that

the variations are not significant, being of the order of 5%.

QCD-RPC Model	GS	DG	DO	LAC1	LAC3
+ 10% VDM	2.04	1.64	1.67	2.25	3.07
+ 5% VDM	1.99	1.60	1.63	2.21	3.01
"standard" VDM	1.95	1.56	1.60	2.17	2.95
- 5% VDM	1.92	1.52	1.56	2.14	2.90
- 10%VDM	1.88	1.48	1.52	2.10	2.83

Table 1. Final p_T^{min} values for the QCD-RPC models studied.

In each case the number of finally selected simulated events relative to the data was at least greater than 12. To provide comparable conditions for each QCD-RPC parametrization, the differences in the final number of events were less than $\pm 1\%$.

Statistical comparisons between the data and simulated distributions were performed using two independent methods: the well-known χ^2-test and the Kolmogorov test [27]. This algorithm, though not as well-known as the χ^2-test, has some advantages. It does not require a minimum number of entries per bin, which is useful for testing the rather small statistical data sample available. The Kolmogorov test also takes into account the signs of the differences between distributions rather than just the magnitude, which makes the test sensitive to consecutive deviations of the same sign. The measure of compatibility between two distributions is given as a probability, called $\mathcal{P}$ in this paper. A $\mathcal{P}$ value close to 100% indicates a high compatibility between the two distributions, while a value close to zero shows the inverse. The disadvantage of Kolmogorov test is that the returned probability $\mathcal{P}$ for binned data could be overestimated.

The χ^2 for each distribution was defined by the formula

$$\chi^2 = \sum_{i=1}^{N_{ch}} \left[\frac{R_{data}(i) - R_{MC}(i)}{\sqrt{\sigma^2_{data}(i) + \sigma^2_{MC}(i)}} \right]^2 \tag{3}$$

where $R_{data}(i)$ and $R_{MC}(i)$ are the contents of bins i, $\sigma_{data}(i)$ and $\sigma_{MC}(i)$ are their errors, and N_{ch} is the number of non-empty histogram channels, used as a number of degrees of freedom.

The distribution of the invariant mass of the hadronic system,W, is shown for the data and for the VDM+QPM model and VDM+QPM+(QCD-RPC) models in Figures 3b and 3c, respectively. It is clear that the VDM+QPM model cannot provide a good description of the the observed invariant mass distribution. Even when the VDM cross-section was allowed to vary by a factor of two, the resulting probability $\mathcal{P}$ was very small for both Kolmogorov and χ^2-tests. However, adding the QCD-RPC component with any structure function parametrization other than LAC3 gave a good description of the data. The clear evidence for the need of the QCD-RPC contribution is also illustrated in Figure 3d, for the tagged energy fraction.

To illustrate the compatibility of different simulated models with the data, plots of standard event variables and inclusive distributions are presented in Figure 4, while some plots of typical variables from an analysis using jets are shown in Figure 5. Jet reconstruction was performed by using the Lund cluster algorithm with a maximum distance d_{join} of 1.4 GeV/c, below which two clusters are allowed to join into one.

From the $\mathcal{P}$ values given on plots, some parametrizations cannot provide a satisfactory description of all these distributions, as a probability lower than 5% is obtained for some of them. Very similar results with comparable probabilities were obtained using the χ^2-method. Confirming AMY [3], the LAC3 model can be rejected at this stage as the worst model, giving small values of $\mathcal{P}$ for several distributions. The physical reason for that is known: the LAC3 parametrization gives an extraordinarily large gluon density in comparison with other models.

Further attempts to distinguish between remaining parametrizations were performed using an overall χ^2-test, when several distributions were taken into account simultaneously. The invariant mass, tagged energy and jet transverse momentum distributions were chosen as the most important (and not very closely correlated) variables. The tests were also performed with a $\pm 10\%$ variation of the VDM cross-section. The results are shown in Table 2.

QCD-RPC Model	GS	DG	DO	LAC1
+ 10% VDM	1.39	0.07	0.02	4.29
+ 5% VDM	3.52	0.31	0.08	3.82
"standard" VDM	7.05	0.88	0.20	2.32
- 5% VDM	9.53	2.35	0.31	1.17
- 10%VDM	11.94	3.79	0.36	0.32

Table 2. Probabilities (%) from overall χ^2-test for the QCD-RPC models studied. The number of degrees of freedom is equal to 16.

The GS, DG and DO QCD-RPC models behave similarly, their agreement with data becoming better when the VDM contribution is decreased, whereas the LAC1 model follows the opposite trend. The GS parametrization, starting from the "standard" VDM cross-section, rises above the 5% level. The LAC1 comes close to 5% when the VDM cross-section is at 10% higher than "standard" level, the same being true for the DG model when the VDM cross-section is lowered by 10% from the "standard" level. The DO model should be rejected because the overall probability is always very low. These results are in agreement with the previous no-tag analysis from DELPHI [5].

6 Conclusions

For the first time at LEP, very low Q^2 single tagged events have been studied and compared with a full VDM+QPM+(QCD-RPC) model. The data are consistent

with the predictions for quark and gluon density functions provided the QCD-RPC model is used with the GS parametrization. The LAC1 and DG parametrizations are also capable of providing a satisfactory description of the data after tuning of the VDM contribution. The DO and LAC3 parametrizations do not adequately describe the data. Further studies with higher statistics are needed to distinguish between the GS, DG and LAC1 parametrizations.

References

[1] TPC/2γ Coll., H. Aihara *et al.*, Phys. Rev. Lett. **58**(1987)97;
TPC/2γ Coll., H. Aihara *et al.*, Phys. Rev. **D41**(1990)2667.

[2] PLUTO Coll., Ch. Berger *et al.*, Z. Phys. **C26**(1984)353.

[3] AMY Coll., R. Tanaka *et al.*, Phys. Lett. **B277**(1992)215.

[4] ALEPH Coll., D. Buskulic *et al.*, Phys. Lett. **B313**(1993)509.

[5] DELPHI Coll., P. Abreu *et. al.*, "Study of hard scattering processes in multi-hadron production from $\gamma\gamma$ collisions at DELPHI", CERN-PPE/94-04 (1994), Zeit. Phys. **C** to be published.

[6] OPAL Coll., R. Akers *et. al.*, Z.Phys. **C61**(1994)119.

[7] L3 Coll., O. Adriani *et. al.*, Phys. Lett. **318B** (1993) 575

[8] H.Kolanosky, Two-Photon Physics at e^+e^- Storage Rings, Springer Verlag, 1984.

[9] Proc. 9th Int. Workshop on Photon-Photon Collisions, San Diego 1992, eds. D.O. Caldwell and H.P. Paar (World Scientific, Sngapore, 1993).

[10] R. Tanaka, in Proc. 9th Int. Workshop on Photon-Photon Collisions, San Diego 1992, eds. D.O. Caldwell and H.P. Paar (World Scientific, Singapore, 1993), p.87.

[11] M. Drees, R.M. Godbole, Nucl. Phys. **B339**(1990)355.

[12] H. Abramowicz, K. Charchula and A. Levy. Phys. Lett. **B269** (1991) 458.

[13] J. Rosner, NBL report 17522(1972)316.

[14] I.F. Ginzburg, V.G. Serbo, Phys. Lett. **B109**(1982)231.

[15] J.J. Sakurai, D. Schildknecht, Phys. Lett. **B41**(1972)489.

[16] J.K. Storrow. in Proc. 9th Int. Workshop on Photon-Photon Collisions, San Diego 1992, eds. D.O. Caldwell and H.P. Paar (World Scientific, Singapore, 1993), p.147.

[17] M. Drees, K. Grassie. Z. Phys. **C28**(1985)451.

[18] A. Nova, A. Olshevsky, T. Todorov, DELPHI Note 90-35 PROG/152, unpublished.

[19] T. Sjostrand. "PYTHIA 5.6 and JETSET 7.3", CERN-TH 6488/92 (1992).

[20] PLUTO Coll., Ch. Berger *et. al.*, Phys. Lett. **B149**(1984)421;
TASSO Coll., M. Althoff *et. al.*, Z. Phys. **C31**(1986)527;
CELLO Coll., H.J. Behrend *et. al.*, Z. Phys. **C51**(1991)365.

[21] I. Kronkvist *et. al.*, "FASTSIM examination on how different LEP beam parameters affect the acceptance of the VSAT detector", LUNFD6/(NFFL-7061) (1990).
P. Jonsson *et. al.*, "A simulation of the VSAT detector using parametrization of the electromagnetic showers", LUNFD6/(NFFL-7075) (1993).

[22] H. Plothow-Besch, "PDFLIB: A Library of all available Parton Density Functions of the Nucleon, the Pion and the corresponding α_s calculations", CERN/PPE 92-123 (1992).

[23] L.E. Gordon and J.K. Storrow, "The Parton Distribution Functions of the Photon and the Structure Function $F_2^\gamma(x, Q^2)$", MC-TH 91-29 (1991).

[24] D.W. Duke and J.F.Owens, Phys. Rev. **D26** (1982) 1600.

[25] DELPHI Coll., P. Aarnio *et. al.*, Nucl. Instr. and Meth. **A303**(1991)233.

[26] S. Almehed *et al.*, Nucl. Instr. Meth., **A305**(1991)320.

[27] W. T. Eadie *et.al*, Statistical Methods in Experimental Physics, North-Holland, 1971;
CERN/CN, "HBOOK Reference Manual", CERN Program Long Writeup Y250 (1992).

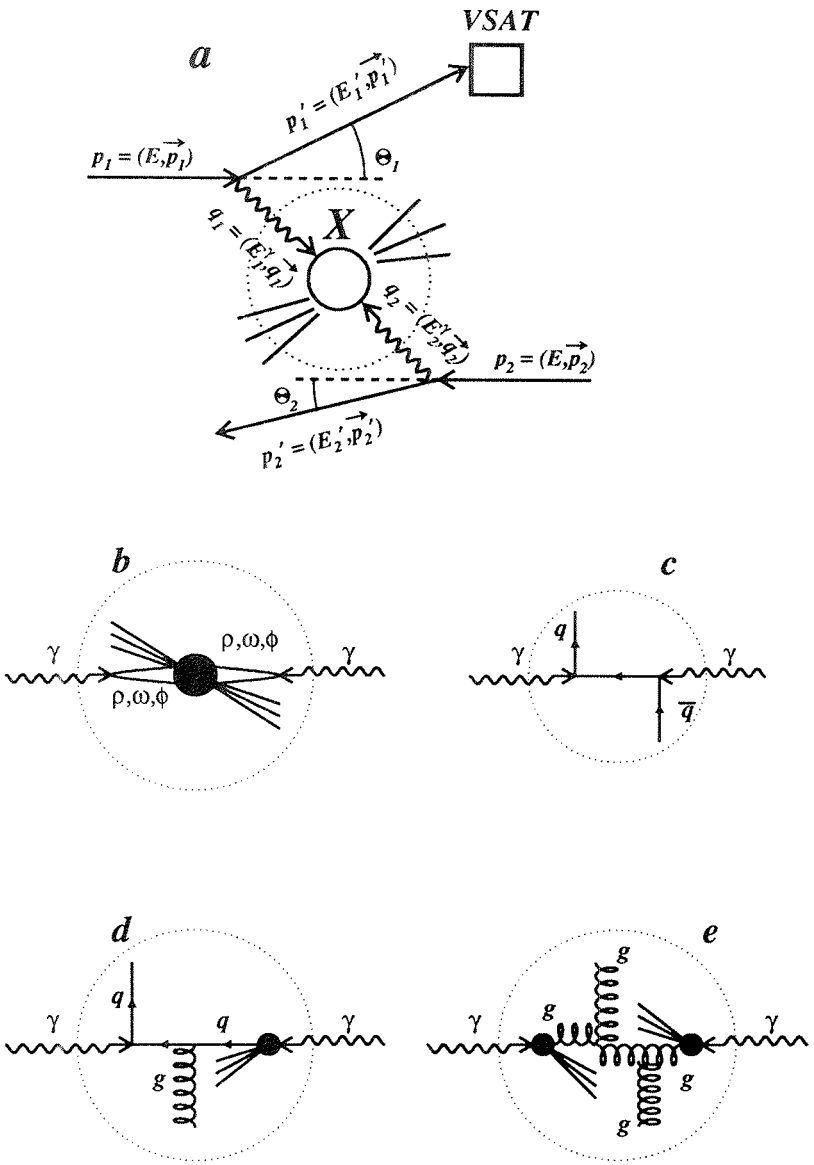

Figure 1: (a) Kinematics of two-photon reaction. One of four VSAT modules is shown as an example of a tagging detector, measured an energy E' and an angle Θ_1 of one of the scattered leptons. (b-e) Diagrams contributing in the lowest order to the $\gamma\gamma$ multihadronic system X: (b) non-perturbative contribution (VDM); (c) direct photon contribution (QPM). Examples of QCD resolved photon contribution (QCD-RPC), (d) for singly resolved photon and (e) for doubly resolved photon.

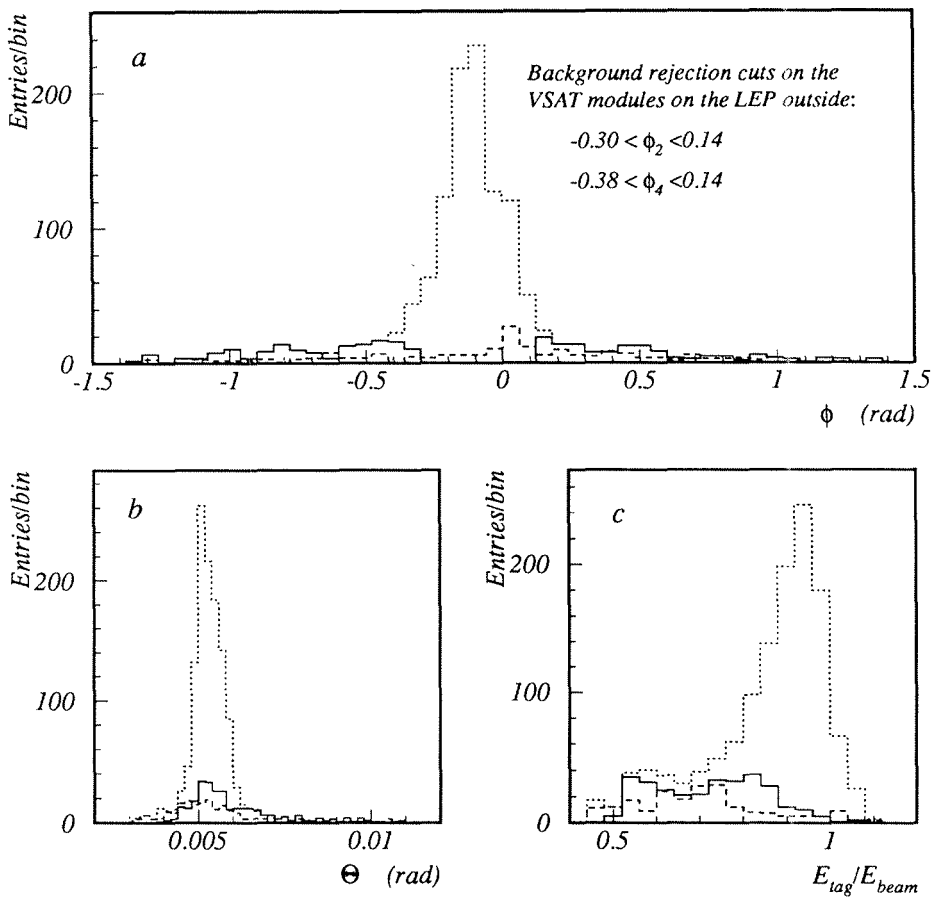

Figure 2: VSAT off-momentum electron background distributions, found from a random coincidence between well measured Z^0 events and high energy signals in one of four VSAT modules: (a) ϕ and (b) Θ-distributions, (c) show E_{tag}/E_{beam}-spectra. Dashed lines show the background behaviors in the inner modules 1 and 3. Dotted lines indicate them in the modules (2 and 4) outside the LEP ring before rejection. Solid lines show the rest of background after applying the cuts on ϕ done for the outer modules 2 and 4 as indicated in (a).

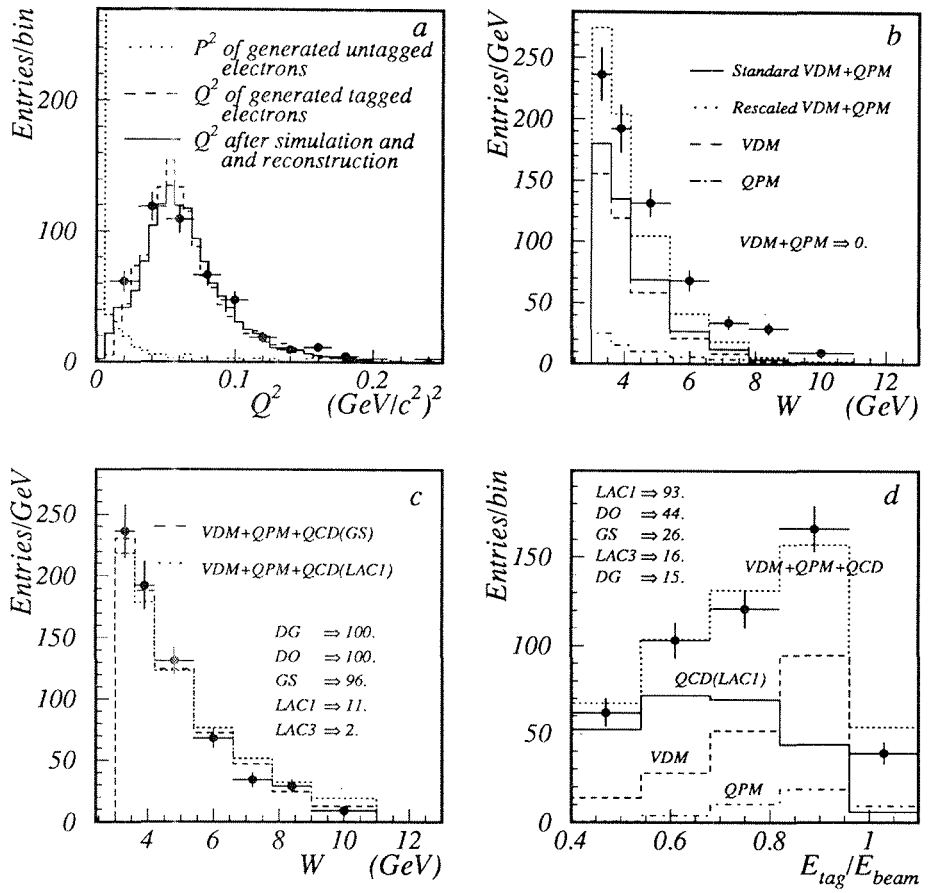

Figure 3: (a) Kinematical Q^2 range of generated and simulated events after final selection. (b) Illustration of impossibility of describing the invariant mass W distribution by VDM+QPM model and (c) satisfactory agreement as for W and (d) as for tagged leptons energy E_{tag} distributions , when some QCD-RPC is added to the simulated events. Without QCD-RPC the resulting probability $\mathcal{P}$ (%) of each Kolmogorov test is very small indeed (indicated as 0. in b) when the VDM contribution is varied across a wide range either to fulfill a total cross-section or to tune the satisfactory description of the shape. Together with some of QCD-RPC models (c and d) the compatibility of data and simulation is rather good, as illustrated by $\mathcal{P}$ with the best model on top and the worst one on bottom.

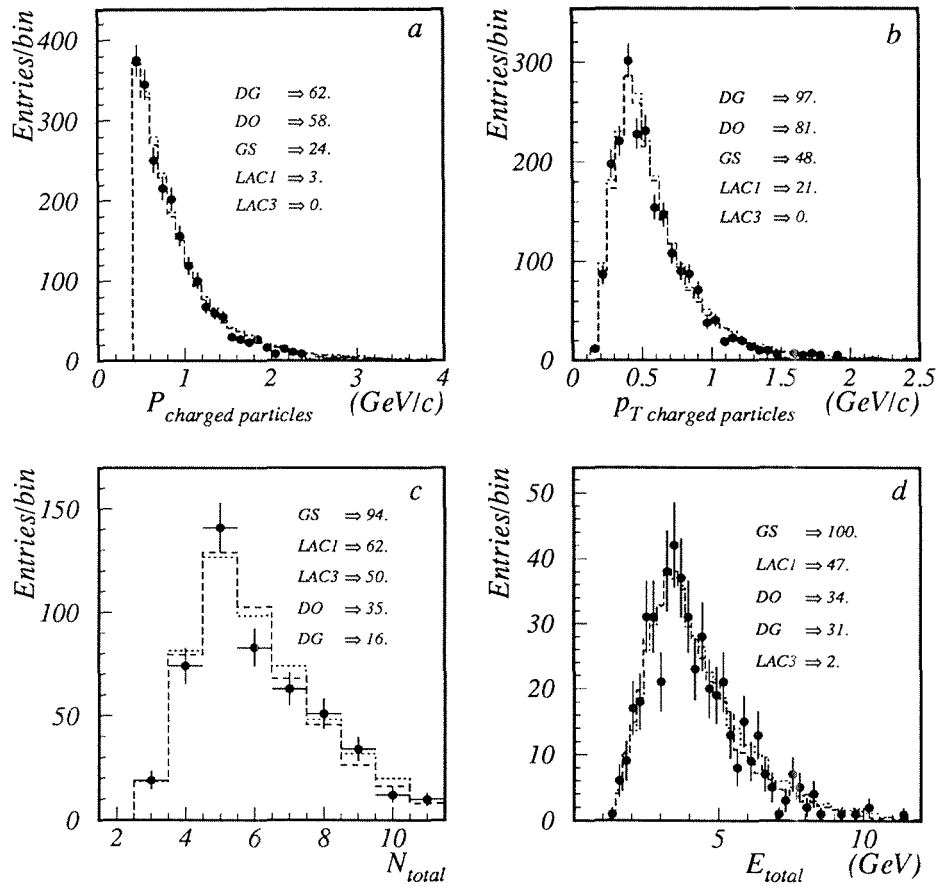

Figure 4: Comparison between data and a full VDM+QPM+(QCD-RPC) simulation. (a) and (b) show some inclusive spectra, while the others display total (charged and neutral particles) multiplicity and energy distributions of the events. The $\mathcal{P}$ values (%) are shown with the best model on top and the worst one on bottom. The GS parametrization used for QCD-RPC simulation is shown by dashed lines and the LAC1 parametrization is shown by dotted lines.

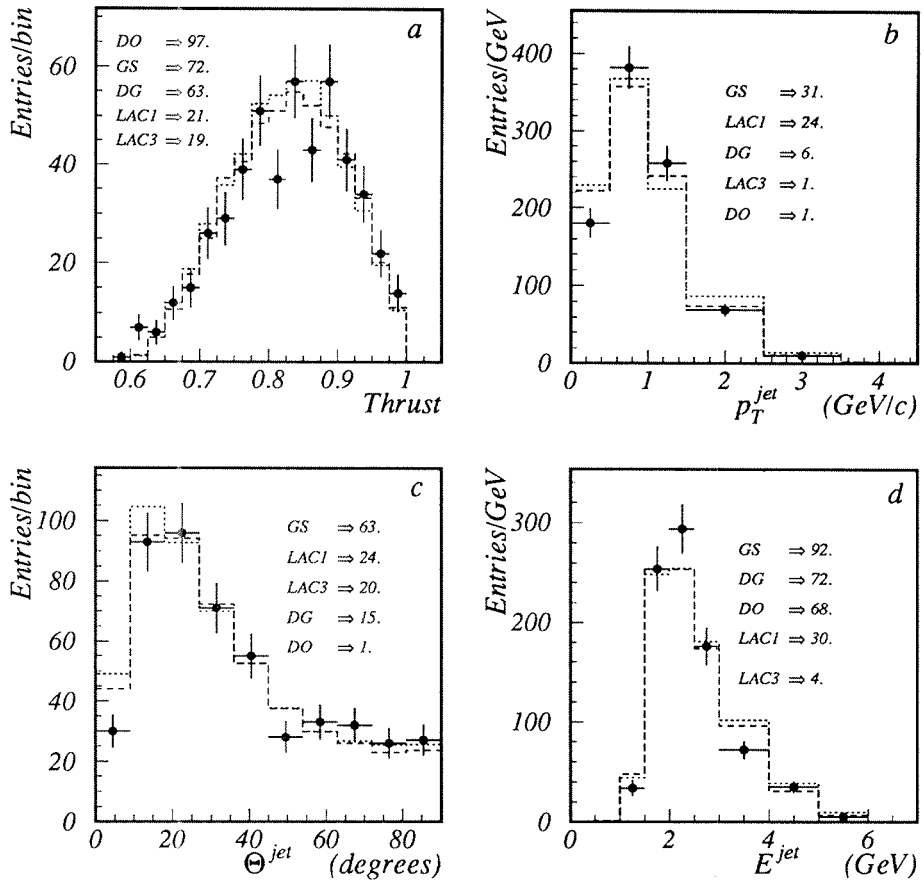

Figure 5: (a) Thrust distribution, (b) transverse momentum, (c) angular and (d) energy distributions for reconstructed jets are shown only for the jets with maximal transverse momentum p_T. The $\mathcal{P}$ values (%) are shown with the best model on top and the worst one on bottom. The GS parametrization used for QCD-RPC simulation is shown by dashed lines and the LAC1 parametrization is shown by dotted lines.

DELPHI Collaboration

DELPHI 93-3 DAS 137
17 December, 1993

The system for online monitoring of LEP beam background and luminosity at the DELPHI interaction point

S. J. Alvsvaag[1], J. Bjarne[2], M. Bozzo[3], J. Buytaert[4], H. Carling[2], Ph. Charpentier[5], P. Courty[6], J. Fuster[5], Ph. Gavillet[5], P. Giacomelli[5], A. Grant[5], Z. Hajduk[7], F. J. Harris[8], G. Jarlskog[2], M. Jonker[5], A. Klovning[1], I. Kronkvist[2], C. Lacasta[9], L. Mathis[6], U. Mjörnmark[2], A. L. Read[10], J. Straver[5], J. Timmermans[11], D. Treille[5], G. Valenti[12], J. A. Valls Ferrer[9]

Abstract

This report describes the DELPHI online system for monitoring LEP beam background and luminosity at the interaction point. The signals available from the various DELPHI sub-detectors are described in detail. The software used for logging and displaying the information, as of the end of 1992, is also briefly described. The system for LEP communication and display have been enhanced during 1993.

[1]University of Bergen
[2]University of Lund
[3]Università di Genova and INFN
[4]Univ. Instelling Antwerpen
[5]CERN, Geneva
[6]Collège de France, Paris
[7]Institute of Nuclear Physics, Krakow
[8]University of Oxford
[9]U. de Valencia
[10]University of Oslo
[11]NIKHEF-H, Amsterdam
[12]Università di Bologna and INFN

Contents

1 Introduction

This report describes the system for online monitoring of LEP machine performance, beam background and luminosity at the DELPHI interaction point. The response of the DELPHI experiment to changing LEP parameters, *e.g.* collimator settings or beam background, is monitored and sent to the LEP and DELPHI control rooms for display. In return general status information is received from LEP and distributed to DELPHI for display, or for to be logged to the LEPM database [1], by this monitoring system.

An earlier report [2] describes the DELPHI part of this monitoring system, while the experiment-to-LEP communication system is defined by [3]. In the current report is the full system described, including all signals, software and hardware. The performance of the system is briefly discussed, and some information is also given on how a user can access the data logged to the LEPM database by the monitoring system. Several references are also included for further reading.

It should be emphasized that this report describes the communications and display system as of the end of 1992. During 1993 an upgraded system has been implemented [4].

2 Detector signals

Signals are sent to the monitoring system from several different sources. By integrating this information a complete picture of the beam situation around the DELPHI interaction point is obtainable. Since some of the signals give measurements of the same quantity using different detectors, cross checking of these is possible. This information redundancy also increases the reliability of the system.

All the DELPHI sub-detectors provide some spatial data, usually four or six sectors in azimuth, on both sides of the interaction point. Some provide information on each of the individual LEP bunches. This granularity allows detailed analysis of various problems of noise or beam background. Online estimates of beam luminosity are also available from different sources.

The monitoring system uses signals from the following DELPHI sub-detectors:

- Radiation Monitor (RM)
- Inner Detector (ID)
- Time Projection Chamber (TPC)
- Small Angle Tagger (SAT)
- Very Small Angle Tagger (VSAT)

The signals available at a given time are defined by the actual beam status. During beam setup and adjustment, *i.e.* when DELPHI is not taking data, monitoring is provided by the ungated[1] RM, SAT and VSAT signals. The ID and TPC signals are available when their high voltages are on. When the DELPHI data acquisition is running additional, WNG_BCO gated, signals are also available.

The following sections contain a description of the signals sent to the monitoring system from the various individual DELPHI sub-detectors and the LEP luminosity monitors.

[1] In the context of this report "ungated" implies ungated by the DELPHI read-out. The signals are, of course, gated by the beam crossing signal (CLK_BCO).

2.1 RM signals

Four signals are derived from silicon detectors, placed close to and equally spread around the LEP beam pipe as near as possible to the Micro Vertex detector (see Appendix A). The signals are in the form of pulse trains, resulting from the frequency conversion digitizition of the voltage induced by the charged particle radiation. These signals are always available, independently of DELPHI status. The measured values are calibrated and corrected for temperature effects, giving an absolute measurement in Rad per hour. The rate is displayed as a trace plot (see Section 5) in the DELPHI control room. In addition, the signals are continuously integrated throughout the year in order to monitor the radiation level near the Micro Vertex detector.

If the measured level reaches more than 10 Rad/hour on at least two detectors a software signal is sent to the LEP control room, where it is used to issue an inhibit signal against further injection. To decrease the influence of noise pick-up this alarm signal is only sent if it is in time coincidence with a significant background signal from the VSAT detector.

2.2 ID signals

The ID sends two sets of ECL level signals (see Appendix B), each consisting of four channels from the different azimuthal ID sectors (*i.e.* in, out, up and down).

The number of off-momentum electrons and beam-gas interaction products near the interaction point are monitored by the trigger layer rates, coming directly from the ID trigger. These signals are usable also for dedicated background study runs provided a special configuration file is loaded into the ID front end modules, making its trigger layers sensitive also to photons. However, running the trigger layers in normal mode, the photons can be extracted at the offline level. The trigger layer signals are available only when the data acquisition is running. They are thus affected by the DELPHI dead-time.

Synchrotron photons, off-momentum electrons and beam-gas interaction products around the interaction point are measured by the ID high voltage current monitor counters, giving counts proportional to the flux of the incoming ionizing particles (including photons). These signals give the instantaneous DC current drawn from each of the the four ID high voltage power supplies, using hardware containing voltage-to-frequency converters and measuring the currents through high resistances. The current monitor signals are available as soon as the ID high voltage is on, independently of the DELPHI read-out. These four signals are continuously displayed in the DELPHI control room as a trace plot, giving a continuous history of the previous hour.

2.3 TPC signals

The TPC [5] provides 12 NIM signals (see Appendix C), coming from the 12 TPC sectors, for counting and background rate evaluations. Each signal is the logical OR of 96 wire pairs made in a FASTBUS trigger/fan-out module using as input 96 discriminator signals. Each discriminator is attached to two wires, of which it compares the sum of the amplitudes with a programmable threshold. These signals are present provided the chamber is on with high voltage and electronic chain. They are not gated by the DELPHI read-out.

The TPC signals are sensitive to any activity in the chamber, electrons as well as photons, and are continuously displayed in the DELPHI control room as a trace plot. The signals

are also normalised to agreed values and sent to the LEP control room as a measure of the charged particle and photon background in DELPHI (BKGD2).

2.4 SAT signals

Thirty-two ECL level signals are sent directly from the SAT local trigger supervisor (LTS) for online beam monitoring purposes (see Appendix D). The 288 SAT calorimeter cells are arranged azimuthally into four quadrants. They provide both off-momentum electron background information as well as Bhabha and accidental Bhabha trigger counting rates for estimating the luminosity. SAT information on luminosity is also provided by their online spy monitor program.

The SAT signals are available gated by the DELPHI read-out or ungated (*i.e.* independently of the data acquisition). Setting the CSR#1<2> bit in the SAT LTS allows it to *internally* trigger on each CLK_BCO. The gating of the signals finally available at the two LTS fan-out connectors S1 and S2 are set by hardware jumpers L9-L14. The gatings of the signals below are described in the way the SAT LTS is normally set up, which is with S1 DELPHI gated and S2 ungated.

The trigger signals available from the S1 and S2 connectors are not bunch-labelled, but a six bit bunch counter is available in the FEB of the SAT LTS for each T2_YES. A counter for the ungated 10 GeV Bhabha coincidences not seen due to DELPHI dead time is also available in the FEB.

2.4.1 Ungated signals

The off-momentum electron rates are given individually by SAT for each azimuthal quadrant and on both sides of the interaction point, using either a 10 GeV or a 30 GeV energy threshold. Four other signals, one for the quadrant sum on each SAT side, are also available with both 10 GeV and 30 GeV energy thresholds. Off-momentum electron background profile and beam-beam background difference studies are made possible using these signals. The sum of the signals for the two sides of the interaction point are displayed in the DELPHI control room as a measure of the $e^{\pm}$ scattered background. It is also used to estimate the background conditions before raising the voltages on the more sensitive detectors.

For estimating the luminosity a Bhabha trigger counting signal is provided, having a 10 GeV energy threshold and a 30 degree acoplanarity cut. A single arm coincidence signal is also available using a 30 GeV energy threshold. The luminosity is calculated using conversion factors reflecting the SAT Bhabha cross section.

During bad beam conditions, the contribution to the Bhabha triggering from purely statistical coincidences can increase. In order to estimate this effect an accidental Bhabha signal is available, triggered by a hit in one SAT side and a hit in the other side N BCOs later, where N is the number of bunches in LEP. The rate is normally low enough to be insignificant for online luminosity measurements.

A 10 GeV *vs.* 30 GeV threshold Bhabha signal is also available with a programmable segmentation size.

2.4.2 DELPHI-gated signals

Four quadrant-sum off-momentum electron background signals are provided as in the

ungated case.

The DELPHI-gated Bhabha, single arm coincidence and accidental Bhabha signals are provided as in the ungated case.

T1_YES, T2_YES and T2_BHABHA signals are available, though only the first is used for the luminosity estimation.

The SAT online spy monitor program, using routines similar to the final offline analysis, gives a good estimate of the luminosity as measured by SAT. Both a continuously updated luminosity (at 20 minutes time intervals) and a fill integrated luminosity are calculated. They are both logged to the LEPM database.

2.5 VSAT signals

The VSAT [6] local trigger supervisor provides 26 ECL level signals to the monitoring system (see Appendix E), giving information on beam luminosity through Bhabha trigger counting and beam background through counting off-momentum electrons and accidental Bhabha coincidences. Information on beam luminosity and vertex position is also given by the VSAT online spy monitor program [7]. Except for the latter, all the VSAT signals are bunch-labelled and use 20 GeV energy thresholds.

The VSAT signals can be divided into three groups: those being ungated (*i.e.* independent of the data acqusition), those being gated by the DELPHI read-out and the bunch counters. Most of the VSAT signals are logged to the LEPM database.

2.5.1 Ungated signals

The ungated signals are independent of the actual VSAT trigger set-up. A signal counting the number of BCOs *not* seen by the VSAT is provided for calculating the VSAT dead-time.

A VSAT estimate of the luminosity is given by Bhabha trigger counting in each of the two diagonal detector arms (subtracting the background, see below). The luminosity is calculated by summing the two diagonals and normalising by an effective cross section derived from the comparison of the integrated SAT and VSAT rates and the well-studied SAT Bhabha cross section.

As in the SAT case, the background to the Bhabha triggering is estimated by counting accidental Bhabhas for each Bhabha arm. This means that after a hit in a VSAT module one waits N BCOs, where N is the number of bunches in LEP, for a hit in its diagonal module. If so, the accidental Bhabha counter for this Bhabha arm is incremented. Though the accidental Bhabha signals in themselves are estimates of the beam conditions, they are also subtracted from the Bhabha triggering signals in order to get a background-corrected estimate of the luminosity.

The off-momentum electron spectrum on either side of DELPHI and on both the LEP inner and outer sides are monitored by VSAT using signals from each of its four modules. These signals are sensitive to beam background conditions, and are displayed in the DELPHI control room. The total sum is normalised and sent to the LEP control room as a measure of the charged particle background at DELPHI (BKGD1).

2.5.2 DELPHI-gated signals

The Bhabha, accidental Bhabha and off-momentum electron signals are also available

gated by the DELPHI read-out. These signals are dependent on the actual VSAT trigger set-up. This normally means that the first electron of an accidental Bhabha event is only taken from the two inner modules of LEP, since these have a lower off-momentum electron rate.

The luminosity is also given by VSAT using the online spy monitor program. It uses Bhabha and accidental Bhabha selection routines similar to the VSAT offline routines. It also gives a measure of the vertex position. The information is updated every 10 minutes and is not bunch-labelled. The spy monitor program is described in detail in [7].

2.5.3 Bunch counters

The current bunch number is available using seven bits, allowing any number of LEP bunches up to 127. The procedures to unpack and use these signals are presently not defined.

2.6 LEP signals

The LEP beam instrumentation group also provides ungated luminosity monitors very similar to those used by the VSAT. These are placed in the collimators at ± 8.5 m from the interaction point. There has been little attempt to provide an accurate luminosity normalisation for these detectors. Since they have a fast response their relative luminosity measurement is used to scan and optimise the voltages on the vertical electrostatic separators.

The data from these detectors is available through the normal LEP-DELPHI communication system [3], and is logged and displayed together with the other monitor data.

3 Hardware

The hardware used by the DELPHI online monitoring system is described in detail in [8]. The signals used by the monitoring system are sent to three 32-channel Struck STR200 FASTBUS scalers, located with the other similar trigger monitor scalers in DELPHI counting room B2. A patch-box receives the ID and TPC signals and merges them into one scaler. The SAT and VSAT signals are routed directly to the other two scalers.

4 Communication software

The software and routes used to read the trigger and luminosity monitoring scalers, and to make the data available on the DELPHI online computer cluster, are described in detail in [8]. Sections 1.3 and 2.0 of this report describe the data formats and communication software which provide values of all the 13 32-channel scalers and control timing information centrally on the online cluster. This information is updated every 15 seconds. An important feature of this package is that the description of the contents of the individual scalers is configured from a database file and is accessible *via* a library program.

Once the monitor data is available on the central cluster the data is processed (*e.g.* sampled, integrated, combined or normalised) and sent to several destinations for displaying or logging.

4.1 LEP communication

Some limited information is received from LEP *via* a video system and displayed in the control rooms and around CERN. All this information and much more details of the machine condition are also received over the computer network. Information on the DELPHI status is also sent to the LEP control room.

One of the most important reasons for monitoring the LEP beam background and the delivered luminosity is, of course, to return this information to the LEP control room. Only by providing sensitive measurements of the beams can the LEP engineers tune the machine for optimum running conditions.

This two-way communication between the LEP and DELPHI computer systems is done *via* a set of data structures, or 'tables' [3]. At 20 second intervals these are read from, or sent to, a server running on a machine in the LEP control room *via* RPC calls overlaid on TCP/IP. At the DELPHI side of this connection runs the LEP_TALK program, which acts as the receiver, processor and dispatcher of all information. This program uses the standard MJU utility packages and is structured in a similar way to the other monitor programs. The program is highly modular due to the complexity of having many different sources of data input, several independent processing strands and multiple output channels. The different aspects are expanded in the following.

The top directory of the programs and files mentioned are found on the DELPHI online cluster in DELPHI$SPECIFIC:[LEP.LEPCOMM]

4.1.1 LEP_TALK input data

The input data to the LEP_TALK program consists of the following classes:

- **Scaler data.** As described in [8], LEP_TALK shares the trigger and monitor scaler data with SCALER_TALK by means of a piece of shared memory (the global section MONITOR_GDATA) in the workstation WSDELE.
- **LEP data tables.** These tables are received by RPC calls to a LEP server *via* TCP/IP. Five different structures are read separately.
- **Solenoid magnet.** The solenoid magnet data are in a shared memory with the process SOL_FIELD, which makes RPC calls to the solenoid G64 system.
- **Luminosity data.** LEP_TALK reads files prepared by the SAT and VSAT detectors containing luminosity data calculated by the respective spy monitoring tasks.
- **Control signals.** As the LEP_TALK program runs as a batch process, its running condition may be altered upon receipt of 'MJU_signals' from the interactive process LUMINOSITY_CONTROL. Possible changes are to alter the source of the luminosity calculation, reset internal scalers, change fill number *etc.*

4.1.2 LEP_TALK output data

The LEP_TALK program produces the following output:

- **LEP data tables.** A data structure (DELPHI1) is sent to the LEP server. It contains a summary of the scaler data: normalised backgrounds (BKGD1 and BKGD2) and

radiation levels from the RM counters. This information is continuously displayed in the LEP control room. Instantaneous and integral luminosities as measured by DELPHI are also sent, these being calculated from several sources (SAT, VSAT, trigger *etc*). What to send is interactively controled by LUMINOSITY_CONTROL, as described above.

- **Luminosity summaries.** The luminosity file LUM_SUMMARY_XXX.DAT is accessible by the LEP coordinator and gives the average luminosity each 20 minutes during the fill XXX. A second luminosity file, INTEGRAL_LOG.DAT, gives the current set of luminosity integrals during the year. In both cases the source of the luminosity calculation is chosen interactively from LUMINOSITY_CONTROL.

- **PAGE101 display.** A file is written that gives a computer-readable form of the video display, together with some additional information. The command `TYPAGE101` has been defined for displaying this on a computer screen.

- **LEP status signal.** A MJU-type signal is generated containing LEP status information. This is widely used in the DELPHI data acquisition chain to distribute the current LEP data, fill number, state *etc.* It is decoded by linking to the library LEP_SIGNAL.OLB and by including LEP_STAT.INC in the source deck.

- **Real time trace plot data.** Some processed data (backgrounds, luminosities *etc.*) is added to the MONITOR_GDATA global section to facilitate the use of the trace plot displays discussed below. A description of the contents is in the file LEP_DATA.TXT.

- **LEP data on output tape.** Some LEP data is accessed by the SCALER_TALK program and sent *via* the TP_CP FIP to be written in the header record of each event. A description of the contents can be found in [10].

- **LEPM database data.** A large amount of LEP data, read from the LEP tables, is logged to the DELPHI database file LEPM. A detailed description of the contents of the various fields can be found in [1]. See also Section 5.3.5 and Appendix F.

In addition to these direct outputs from the LEP_TALK program there are other more indirect transfers of data. LEP_TALK now acts as an information server for the DIM system [11], providing data for a MOTIF display which gives a more sophisticated version of the PAGE101 information. There is also an implemention of a LEP SMI object and various sub-objects which display the states of LEP and the DELPHI data acquisition system. This system was foreseen to handle veto commands [13], but as yet these have not been provided by LEP.

5 Display software

A general set of routines have been written which allows access to all the trigger and LEP database information. Each unit of data, be it a trigger scaler or a database value, is known by its class and its name, which is unique to that class. The configuration of the location of the data to the class and name is in SCALER_DB.DAT for the trigger data, described in [8], and in LEP_DATA_DB.DAT for the LEP database (see Section 5.3.5). The data can be integrated over some time and then displayed. An example from the trigger display is described in [8].

Interactive user access to most of the LEPM database data is provided by the trace plot program, allowing a DELPHI user to look at histogram presentations of the data. The READLOG FORTRAN library is also available for users wishing to access the LEPM data inside a program.

5.1 The trace plot program

A set of graphics routines allow the data to be displayed in the form of trace plots, *i.e.* the data values are continuously updated against a horizontal time axis. The display is only redrawn when the foreseen time span is full. When this happens, the earliest ten percent of the data is discarded and the plot is redrawn with a new starting time. Unlike the PAW package, which treats static data, this trace plot display is completely real-time orientated. The modular structure of the routines allows the system to run on different terminals or workstations (X11, UIS *etc*). Various steering routines can can be linked to the system to access data from the trigger scalers, the LEP database server *via* RPC calls or the archive LEP database *via* the CARGO600 library.

The TRACEPLOT program is an interactive program for displaying the data of the LEPM database in the form of histograms. It is available on the DELPHI online cluster on the area:

VXDEOP::DELPHI$SPECIFIC:[LEP.MONITOR]

Several versions of the program are available (*e.g.* PLOT_LUM_ARCH_X11.COM plotting archived data on an X11 terminal). After asking for some input parameters the program displays the user-requested data on the screen. In order to simplify the plotting of standard histograms the TRACEPLOT program can read and write macro files. They are files the program reads its input parameters from instead of from the terminal. Standard macro files are available in the [.MACROS] sub-directory. A user can use the macro files available in the main macro directory (*e.g.* DB_LUM.MACRO displaying the LEP luminosity) or use his/her own.

5.2 The READLOG FORTRAN library

The small FORTRAN library READLOG has been created for users wishing to access the LEPM data inside a program. It consists of three subroutines, and accesses the data using the CARGO package [9]. The user must therefore link the program to the CARGO600 library as well as to READLOG. A library is available as READLOG_NEW.OLB on the same area as above, while the source code is available on the [.SOURCE] sub-directory.

There are essentially only three things the user must know about the READLOG library: the name of the routine to call, the common block which contains the data and how to decode the data. These things are described in detail below.

5.2.1 The READLOG routine

In the READLOG library exists a subroutine with the same name. This is the only READLOG routine that a user needs to call. There are two arguments in the call:

- **IFILL**, which is the fill you want data from. The first time READLOG is called with a certain IFILL the library automatically reads the auxiliary record for that fill. From

this it gets the date and time for the start and end of the fill. Subsequent calls to READLOG with the same IFILL as the previous call will give the data from the next update in the database.

- **IERR**, which is an error flag. As long as IERR=0 everything is OK. If IERR<0 there is no data available for the required IFILL. If IERR>0 the last update for the specified IFILL has been read, and thus there is no more data to read.

5.2.2 The LEPDAT common block

The output from READLOG is put in the LEPDAT common block. There are three variables in this common, and the line to put in the user program should look like:

```
COMMON /LEPDAT/ DATLEP(500),NTOTUP,NCURUP
```

- **DATLEP** is a real array containing the data having been read from the database. The entries of this array is described in the next section.
- **NTOTUP** is an integer variable defined to contain the total number of updates to the database for the specified IFILL. The use of NTOTUP is as yet not implemented.
- **NCURUP** is an integer variable containing the number of updates having been read from the database for the specific IFILL.

5.2.3 Decoding the output data

In the READLOG directory is also the file LEP_DATA_DB.DAT, defining the data of the LEPM database tree (see Appendix F). For each item it shows:

- The index (N) in the real array DATLEP (see the previous section).
- The class name of the item.
- An integer (I) corresponding to the specific class.
- A one-to-three-word description of the item.
- An integer (J) specifying the order of this item within its class.
- An integer (L) which is 0 if the item is not a valid signal and 1 otherwise.
- The dimension of the item (not always given).

The easiest way to use this table is to search it for the description that matches what is to be read, and then get the corresponding index (N) from the first column.

6 Performance

The performance of the DELPHI online monitoring system regarding some key measurements are demonstrated below, using output from the trace plot program described in Section 5. The horizontal scales are graded in time during fill 1231. The bins (*i.e.* the distances between ticks on the horisontal axes) are set interactively, and are here equivalent

to 120 minutes. The vertical luminosity scales are graded in units of $10^{30} cm^{-2} s^{-1}$, while the vertical background scales are normalised to a value which is consistent for all the four LEP experiments.

A detailed study of the electron and photon beam background around the DELPHI interaction region was made using this monitoring system in 1992. Here the LEP beam collimators were moved while DELPHI monitored its response at each collimator setting. Please see [12] for further details of this study. The performance of the VSAT online spy monitor program is discussed in detail in [7].

7 System upgrade

This report describes the performance of the system as of the end of 1992. During 1993 the DELPHI-LEP communications and display software has been upgraded to enhance its reliability, this development being borne out of several years experience derived from the previous system. The new software is described in [4].

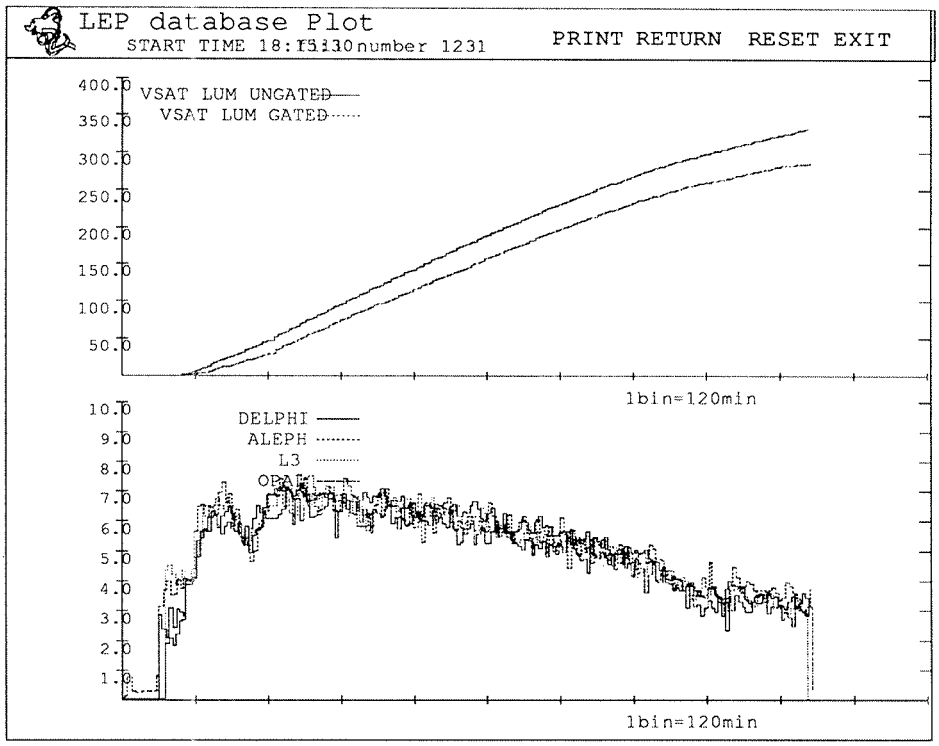

Figure 1: The upper trace plot shows the growth with time of the integral luminosity during fill 1231. The top curve is the luminosity delivered by LEP, while the lower curve is the same but now gated by the DELPHI data acquisition dead time. The lower trace plot shows the instantaneous online luminosity measurements of the four LEP experiments during the same fill. In both of the trace plots are the DELPHI luminosities provided by the background subtracted VSAT Bhabha trigger.

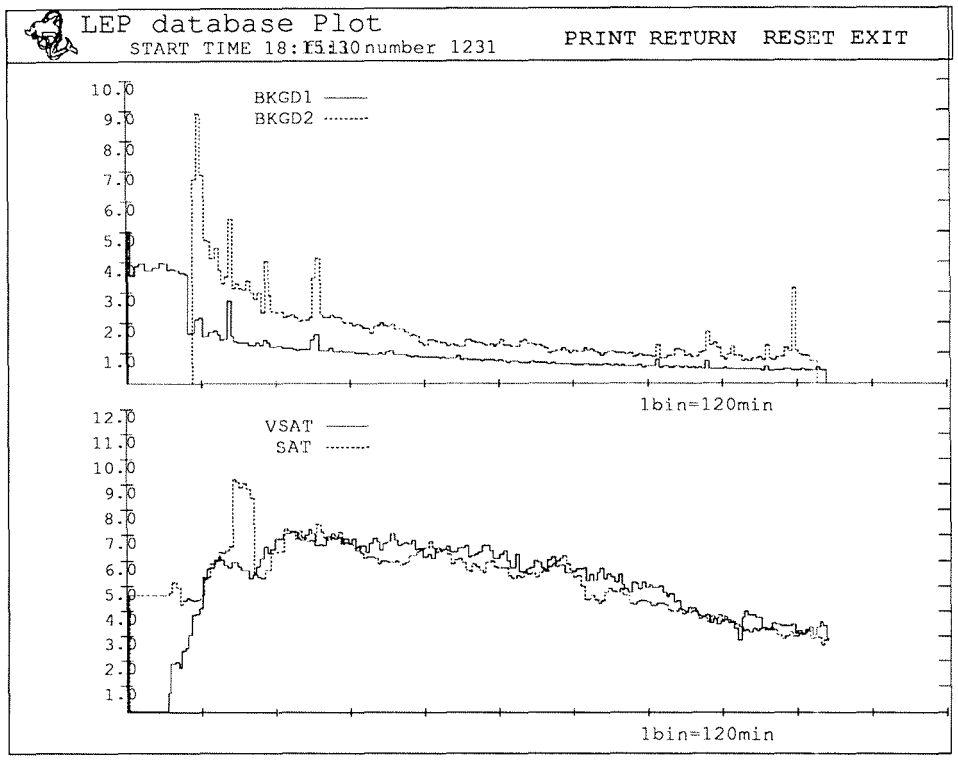

Figure 2: This trace plot shows the beam background variations during fill 1231. BKGD1 is the off-momentum electron background rate from the VSAT. BKGD2 is proportional to the total counting rate of the TPC wires, *i.e.* it is proportional to both the photon and electron fluxes. BKGD1 is available from the beginning of the fill, while BKGD2 becomes available as soon as BKGD1 is low enough to enable the TPC high voltage to be ramped up. The lower plot shows a comparison of the luminosities calculated from the SAT and VSAT Bhabha counters.

A Definition of RM signals

Ch.	Abbreviation	Description
18	RAD_MON_1	Rad/h
19	RAD_MON_2	Rad/h
20	RAD_MON_3	Rad/h
21	RAD_MON_4	Rad/h

Table A1. RM signals in scaler nr. 15, adress 3c00000f.

B Definition of ID signals

Ch.	Abbreviation	Description
12	NW_OUT	Nr. of hit wires, outer quadrant
13	NW_DOWN	Nr. of hit wires, lower quadrant
14	NW_IN	Nr. of hit wires, inner quadrant
15	NW_UP	Nr. of hit wires, upper quadrant
16	HV_IN	HV current counter, inner quadrant
17	HV_UP	HV current counter, upper quadrant
18	HV_OU	HV current counter, outer quadrant
19	HV_DN	HV current counter, lower quadrant

Table B1. ID signals in scaler nr. 4, adress 4c000015.

C Definition of TPC signals

Ch.	Abbreviation	Description
0	NW_A_00	Nr. of hit wires, A side, sector 0
1	NW_C_01	Nr. of hit wires, C side, sector 1
2	NW_A_02	Nr. of hit wires, A side, sector 2
3	NW_C_03	Nr. of hit wires, C side, sector 3
4	NW_A_04	Nr. of hit wires, A side, sector 4
5	NW_C_05	Nr. of hit wires, C side, sector 5
6	NW_A_06	Nr. of hit wires, A side, sector 6
7	NW_C_07	Nr. of hit wires, C side, sector 7
8	NW_A_08	Nr. of hit wires, A side, sector 8
9	NW_C_09	Nr. of hit wires, C side, sector 9
10	NW_A_10	Nr. of hit wires, A side, sector 10
11	NW_C_11	Nr. of hit wires, C side, sector 11

Table C1. TPC signals in scaler nr. 4, adress 4c000015.

D Definition of SAT signals

Ch.	Abbreviation	Description
0	AH	Single arm A-side. High threshold.
1	CH	Single arm C-side. High threshold.
2	AL	Single arm A-side. Low threshold.
3	CL	Single arm C-side. Low threshold.
4	T1_YES_I	Local T1_YES set by LTS CSR#1 and #14h.
5	T2_YES_I	Local T2_YES set by LTS CSR#1 and #14h.
6	TDL2(4)	Second level Bhabha. Gated by D2RDY.
7	TDL2(7)	FDDP tag for "high pulses". Gated by D2RDY.
8	AS	Single arm A-side scintillators. Not impl.
9	CS	Single arm C-side scintillators. Not impl.
10	BBSS	Scintillator coincidence. Not implemented.
11	TDL1(7) BBSHSS	Scintillator*calorimeter coincidence. Not impl.
12	TDL1(0) BBDE	Delayed (accidental) Bhabha. High threshold.
13	TDL1(1) BBHH	Single arm coincidence. High threshold.
14	TDL1(2) BBHL	High*low coincidence. Progr. segment size.
15	TDL1(3) BBLL	Bhabha coincidence. Low threshold.

Table D1. SAT LTS S1 connector signals.

Ch.	Abbreviation	Description
16	QC0	Inner quadrant C-side. Programmable threshold.
17	QC1	Upper quadrant C-side. Programmable threshold.
18	QC2	Outer quadrant C-side. Programmable threshold.
19	QC3	Lower quadrant C-side. Programmable threshold.
20	QA0	Inner quadrant A-side. Programmable threshold.
21	QA1	Upper quadrant A-side. Programmable threshold.
22	QA2	Outer quadrant A-side. Programmable threshold.
23	QA3	Lower quadrant A-side. Programmable threshold.
24	AH	
25	CH	
26	AL	
27	CL	
28	TDL1(0)	
29	TDL1(1)	
30	TDL1(2)	
31	TDL1(3)	

Table D2. SAT LTS S2 connector signals.

E Definition of VSAT signals

Ch.	Description
0	Bhabha F1B2, VSAT gated
1	Bhabha F2B1, VSAT gated
2	Bhabha F1B2, DELPHI gated
3	Bhabha F2B1, DELPHI gated
4	Not connected
5	Not connected
6	Not connected
7	Not connected
8	Bunch number, bit 0
9	Bunch number, bit 1
10	Bunch number, bit 2
11	Bunch number, bit 3
12	Bunch number, bit 4
13	Bunch number, bit 5
14	Bunch number, bit 6
15	Not connected

Table E1. VSAT LTS MIG1 connector signals.

Ch.	Description
16	Acc. Bhabha F1B2, VSAT gated
17	Acc. Bhabha F2B1, VSAT gated
18	Acc. Bhabha F1B2, DELPHI gated
19	Acc. Bhabha F2B1, DELPHI gated
20	F1HI, VSAT gated
21	F2HI, VSAT gated
22	B1HI, VSAT gated
23	B2HI, VSAT gated
24	CLK_BCO
25	WNG0
26	CLK_BCO during VSAT deadtime
27	Not connected
28	F1HI, DELPHI gated
29	F2HI, DELPHI gated
30	B1HI, DELPHI gated
31	B2HI, DELPHI gated

Table E2. VSAT LTS MIG2 connector signals.

F Definition of LEPM data

N	Class	I	Item	J	L	Descr.
1	HEADER	1	FILLNO	0	0	
2	HEADER	1	LBP STATE	1	1	
3	HEADER	1	LBP MODE	2	1	
4	HEADER	1	COLL MODE	3	1	
5	HEADER	1	NUM BUNC+	4	1	
6	HEADER	1	NUM BUNC-	5	1	
7	HEADER	1	E_HALL	6	1	GeV/c
8	HEADER	1	DELTAE	0	0	$\pm 0 - 5$
9	HEADER	1	E_COIL	7	1	GeV/c
10	HEADER	1	COIL TIME	0	0	
11	HEADER	1	RF freq	0	0	
12	HEADER	1	RF freq	8	1	dble prc
13	HEADER	1	BETA* V	9	1	cms
14	HEADER	1	V SEPAR	10	1	microns
15	BUNCH	2	PHE	1	1	nm
16	BUNCH	2	PVE	2	1	nm
17	BUNCH	2	EHE	3	1	nm
18	BUNCH	2	EHE	4	1	nm
19	BUNCH	2	CURR+1	5	1	mA
20	BUNCH	2	CURR+2	6	1	mA
21	BUNCH	2	CURR+3	7	1	mA
22	BUNCH	2	CURR+4	8	1	mA
23	BUNCH	2	CURR+5	9	1	mA
24	BUNCH	2	CURR+6	10	1	mA
25	BUNCH	2	CURR+7	11	1	mA
26	BUNCH	2	CURR+8	12	1	mA
27	BUNCH	2	CURR-1	13	1	mA
28	BUNCH	2	CURR-2	14	1	mA
29	BUNCH	2	CURR-3	15	1	mA
30	BUNCH	2	CURR-4	16	1	mA
31	BUNCH	2	CURR-5	17	1	mA
32	BUNCH	2	CURR-6	18	1	mA
33	BUNCH	2	CURR-7	19	1	mA
34	BUNCH	2	CURR-8	20	1	mA
35	BUNCH	2	SPARE	21	0	
36	BUNCH	2	SPARE	22	0	
37	BUNCH	2	SPARE	23	0	
38	BUNCH	2	SPARE	24	0	
39	BUNCH	2	SPARE	25	0	
40	BUNCH	2	SPARE	26	0	
41	BUNCH	2	SPARE	27	0	
42	BUNCH	2	SPARE	28	0	
43	SOLENOID	3	PSU1	1	1	A
44	SOLENOID	3	PSU2	2	1	A
45	SOLENOID	3	PSU3	3	1	A
46	SOLENOID	3	NMR1	4	1	T
47	SOLENOID	3	NMR2	5	1	T
48	SOLENOID	3	NMR3	6	1	T
49	QUAD	4	QS0R	1	1	A
50	QUAD	4	QS0L	2	1	A
51	QUAD	4	QS1R	3	1	A
52	QUAD	4	QS1L	4	1	A
53	QUAD	4	QS2R	5	1	A
54	QUAD	4	QS2L	6	1	A
55	QUAD	4	QS3	7	1	A
56	QUAD	4	QS4	8	1	A
57	QUAD	4	QS5R	9	1	A
58	QUAD	4	QS5L	10	1	A
59	QUAD	4	QS6	11	1	A
60	VACU	5	P831	1	1	10E10 T
61	VACU	5	P839	2	1	10E10 T
62	VACU	5	G845	3	1	10E10 T
63	VACU	5	P847	4	1	10E10 T
64	VACU	5	P851	5	1	10E10 T
65	VACU	5	G853	6	1	10E10 T
66	VACU	5	P855	7	1	10E10 T
67	VACU	5	P862	8	1	10E10 T
68	LBP	6	FILLNO	1	1	
69	LBP	6	START DAY	0	0	
70	LBP	6	START TIME	0	0	

Table F1. LBPM data.

N	Class	I	Item	J	L
71	LBP	6	END DAY	0	0
72	LBP	6	END TIME	0	0
73	LBP	6	BKGD1	2	1
74	LBP	6	BKGD2	3	1
75	INTEGRAL	7	DISPLAY INT	1	1
76	INTEGRAL	7	DISP TIME	0	0
77	LBP	6	LUM MON1	4	1
78	LBP	6	LUM MON2	5	1
79	LBP	6	LUM ERR AVG	6	1
80	INTEGRAL	7	INT VSA GAT	2	1
81	LUM	8	NUM SAT MIG	1	1
82	LUM	8	LUM SAT MIG	2	1
83	LUM	8	ERR SAT MIG	3	1
84	LUM	8	SPE SAT MIG	4	1
85	LUM	8	NUM SAT SPY	5	1
86	LUM	8	LUM SAT SPY	6	1
87	LUM	8	ERR SAT SPY	7	1
88	INTEGRAL	7	INT SAT SPY	3	1
89	LUM	8	LUM VSA SPY	8	1
90	LUM	8	ERR VSA SPY	9	1
91	INTEGRAL	7	INT VSA SPY	4	1
92	BEAMSPOT	9	HOR POS VSA	1	1
93	BEAMSPOT	9	VER POS VSA	2	1
94	LUM	8	LUM VSA MIG	10	1
95	LUM	8	ERR VSA MIG	11	1
96	LUM	8	SPE VSA MIG	12	1
97	LBP	6	LUM DELPHI	7	1
98	LBP	6	LUM ALEPH	8	1
99	LBP	6	LUM L3	9	1
100	LBP	6	LUM OPAL	10	1
101	BEAMSPOT	9	HOR PO+ BOM	3	1
102	BEAMSPOT	9	HOR AN+ BOM	4	1
103	BEAMSPOT	9	VER PO+ BOM	5	1
104	BEAMSPOT	9	VER AN+ BOM	6	1
105	BEAMSPOT	9	CHISQ HOR+	0	0
106	BEAMSPOT	9	CHISQ VER+	0	0
107	BEAMSPOT	9	HOR PO- BOM	7	1
108	BEAMSPOT	9	HOR AN- BOM	8	1
109	BEAMSPOT	9	VER PO- BOM	9	1
110	BEAMSPOT	9	VER AN- BOM	10	1
111	BEAMSPOT	9	CHISQ HOR-	0	0
112	BEAMSPOT	9	CHISQ VER-	0	0
113	BEAMSPOT	9	RAW DATA B+	0	0
114	BEAMSPOT	9	RAW DATA B+	0	0
115	BEAMSPOT	9	RAW DATA B+	0	0
116	BEAMSPOT	9	RAW DATA B+	0	0
117	BEAMSPOT	9	RAW DATA B+	0	0
118	BEAMSPOT	9	RAW DATA B+	0	0
119	BEAMSPOT	9	RAW DATA B+	0	0
120	BEAMSPOT	9	RAW DATA B+	0	0
121	BEAMSPOT	9	RAW DATA B+	0	0
122	BEAMSPOT	9	RAW DATA B+	0	0
123	BEAMSPOT	9	RAW DATA B+	0	0
124	BEAMSPOT	9	RAW DATA B+	0	0
125	BEAMSPOT	9	RAW DATA B+	0	0
126	BEAMSPOT	9	RAW DATA B+	0	0
127	BEAMSPOT	9	RAW DATA B+	0	0
128	BEAMSPOT	9	RAW DATA B+	0	0
129	BEAMSPOT	9	RAW DATA B+	0	0
130	BEAMSPOT	9	RAW DATA B+	0	0
131	BEAMSPOT	9	RAW DATA B+	0	0
132	BEAMSPOT	9	RAW DATA B+	0	0
133	BEAMSPOT	9	RAW DATA B+	0	0
134	BEAMSPOT	9	RAW DATA B+	0	0
135	BEAMSPOT	9	RAW DATA B+	0	0
136	BEAMSPOT	9	RAW DATA B+	0	0
137	BEAMSPOT	9	RAW DATA B+	0	0
138	BEAMSPOT	9	RAW DATA B+	0	0
139	BEAMSPOT	9	RAW DATA B+	0	0
140	BEAMSPOT	9	RAW DATA B+	0	0

Table F1. LBPM data (continued).

N	Class	I	Item	J	L
141	BBAMSPOT	9	RAW DATA B+	0	0
142	BBAMSPOT	9	RAW DATA B+	0	0
143	BBAMSPOT	9	RAW DATA B+	0	0
144	BBAMSPOT	9	RAW DATA B-	0	0
145	BBAMSPOT	9	RAW DATA B-	0	0
146	BBAMSPOT	9	RAW DATA B-	0	0
147	BBAMSPOT	9	RAW DATA B-	0	0
148	BBAMSPOT	9	RAW DATA B-	0	0
149	BBAMSPOT	9	RAW DATA B-	0	0
150	BBAMSPOT	9	RAW DATA B-	0	0
151	BBAMSPOT	9	RAW DATA B-	0	0
152	BBAMSPOT	9	RAW DATA B-	0	0
153	BBAMSPOT	9	RAW DATA B-	0	0
154	BBAMSPOT	9	RAW DATA B-	0	0
155	BBAMSPOT	9	RAW DATA B-	0	0
156	BBAMSPOT	9	RAW DATA B-	0	0
157	BBAMSPOT	9	RAW DATA B-	0	0
158	BBAMSPOT	9	RAW DATA B-	0	0
159	BBAMSPOT	9	RAW DATA B-	0	0
160	BBAMSPOT	9	RAW DATA B-	0	0
161	BBAMSPOT	9	RAW DATA B-	0	0
162	BBAMSPOT	9	RAW DATA B-	0	0
163	BBAMSPOT	9	RAW DATA B-	0	0
164	BBAMSPOT	9	RAW DATA B-	0	0
165	BBAMSPOT	9	RAW DATA B-	0	0
166	BBAMSPOT	9	RAW DATA B-	0	0
167	BBAMSPOT	9	RAW DATA B-	0	0
168	BBAMSPOT	9	RAW DATA B-	0	0
169	BBAMSPOT	9	RAW DATA B-	0	0
170	BBAMSPOT	9	RAW DATA B-	0	0
171	BBAMSPOT	9	RAW DATA B-	0	0
172	BBAMSPOT	9	RAW DATA B-	0	0
173	BBAMSPOT	9	RAW DATA B-	0	0
174	BBAMSPOT	9	RAW DATA B-	0	0
175	BBAMSPOT	9	RAW DATA B-	0	0
176	BBAMSPOT	9	RAW DATA B-	0	0
177	BBAMSPOT	9	FILLNO	0	0
178	BBAMSPOT	9		11	1
179	BBAMSPOT	9		12	1
180	BBAMSPOT	9		13	1
181	BBAMSPOT	9		14	1
182	BBAMSPOT	9		15	1
183	BBAMSPOT	9		16	1
184	MAGTBMP	10	FILLNO	0	0
185	MAGTBMP	10	MAG 137	1	1
186	AIRTBMP	11	AIR 137	1	1
187	MAGTBMP	10	MAG 163	2	1
188	AIRTBMP	11	AIR 163	2	1
189	MAGTBMP	10	MAG 237	3	1
190	AIRTBMP	11	AIR 237	3	1
191	MAGTBMP	10	MAG 263	4	1
192	AIRTBMP	11	AIR 263	4	1
193	MAGTBMP	10	MAG 337	5	1
194	AIRTBMP	11	AIR 337	5	1
195	MAGTBMP	10	MAG 363	6	1
196	AIRTBMP	11	AIR 363	6	1
197	MAGTBMP	10	MAG 437	7	1
198	AIRTBMP	11	AIR 437	7	1
199	MAGTBMP	10	MAG 463	8	1
200	AIRTBMP	11	AIR 463	8	1
201	MAGTBMP	10	MAG 537	9	1
202	AIRTBMP	11	AIR 537	9	1
203	MAGTBMP	10	MAG 563	10	1
204	AIRTBMP	11	AIR 563	10	1
205	MAGTBMP	10	MAG 637	11	1
206	AIRTBMP	11	AIR 637	11	1
207	MAGTBMP	10	MAG 663	12	1
208	AIRTBMP	11	AIR 663	12	1
209	MAGTBMP	10	MAG 737	13	1
210	AIRTBMP	11	AIR 737	13	1

Table F1. LBPM data (continued).

N	Class	I	Item	J	L
211	MAGTBMP	10	MAG 763	14	1
212	AIRTBMP	11	AIR 763	14	1
213	MAGTBMP	10	MAG 837	15	1
214	AIRTBMP	11	AIR 837	15	1
215	MAGTBMP	10	MAG 863	16	1
216	AIRTBMP	11	AIR 863	16	1
217	RFDT	12	FILLNO	0	0
218	RFDT	12	RF FRBQ1	1	1
219	RFDT	12	RF FRBQ2	2	1
220	RFDT	12	QS B+	3	1
221	RFDT	12	QS B-	4	1
222	RFSW	12	RF_231	1	1
223	RFFCP	13	RF_231	1	1
224	RFRCP	14	RF_231	1	1
225	RFDBT	15	RF_231	1	1
226	RFSW	12	RF_232	2	1
227	RFFCP	13	RF_232	2	1
228	RFRCP	14	RF_232	2	1
229	RFDBT	15	RF_232	2	1
230	RFSW	12	RF_271	3	1
231	RFFCP	13	RF_271	3	1
232	RFRCP	14	RF_271	3	1
233	RFDBT	15	RF_271	3	1
234	RFSW	12	RF_272	4	1
235	RFFCP	13	RF_272	4	1
236	RFRCP	14	RF_272	4	1
237	RFDBT	15	RF_272	4	1
238	RFSW	12	RF_631	5	1
239	RFFCP	13	RF_631	5	1
240	RFRCP	14	RF_631	5	1
241	RFDBT	15	RF_631	5	1
242	RFSW	12	RF_632	6	1
243	RFFCP	13	RF_632	6	1
244	RFRCP	14	RF_632	6	1
245	RFDBT	15	RF_632	6	1
246	RFSW	12	RF_671	7	1
247	RFFCP	13	RF_671	7	1
248	RFRCP	14	RF_671	7	1
249	RFDBT	15	RF_671	7	1
250	RFSW	12	RF_672	8	1
251	RFFCP	13	RF_672	8	1
252	RFRCP	14	RF_672	8	1
253	RFDBT	15	RF_672	8	1
254	RFSW	12	SCRF_233	9	1
255	RFFCP	13	SCRF_233	9	1
256	RFRCP	14	SCRF_233	9	1
257	RFDBT	15	SCRF_233	9	1
258	BNDT	16	FILLNO	0	0
259	BNDT	16		1	1
260	BNDT	16		1	1
261	BNDT	16		0	0
262	BNDT	16		0	0
263	BNDT	16		0	0
264	BNDT	16		0	0
265	BNDT	16		0	0
266	BNDT	16		0	0
267	BNDT	16		0	0
268	BNDT	16		0	0
269	BNDT	16		0	0
270	BNDT	16		0	0
271	BNDT	16		0	0
272	BNDT	16		0	0
273	BNDT	16		0	0
274	BNDT	16		0	0
275	BNDT	16		0	0
276	BNDT	16		0	0
277	BNDT	16		0	0
278	BNDT	16		0	0

Table F1. LBPM data (continued).

References

[1] Yu. Belokopytov, G.P. Gopal, A.L. Grant, H. Klein, V. Perevozchikov:
The Delphi DataBase Description: The LEP Machine Parameter and Luminosity File,
DELPHI 93-2 PROG 193 DAS 136

[2] G. Jarlskog, M. Jonker:
Background and Luminosity Monitoring in DELPHI,
DELPHI 89-59 MIG 3

[3] M.J. Clayton, G. von Holtey, P. Lienard:
Connection of the LEP Experiments and the General Surveillance System to the LEP Control System, LEP Controls Note 94

[4] M. Dönszelmann, C. Gaspar:
The DELPHI distributed information system for exchanging LEP machine related information, DELPHI 93-131 DAS 145

[5] P. Antilogus *et. al.*:
The DELPHI time projection chamber,
Nucl. Instr. and Meth. A283(1989)567

[6] S. Almehed *et. al.*:
A silicon-tungsten electromagnetic calorimeter for LEP,
Nucl. Instr. and Meth. A305(1991)320

[7] J. Bjarne *et. al.*:
VSAT online monitoring of LEP beam parameters,
forthcoming DELPHI Note

[8] J.A. Fuster *et. al.*:
The online software for the first and second level trigger of DELPHI,
DELPHI 91-112 DAS 115

[9] Yu. Belokopytov, V. Perevozchikov:
CARGO400 Data Base Management Package,
DELPHI 90-36 PROG-153

[10] Y. Sacquin:
Delphi Pilot Record Description,
DELPHI 91-90 PROG 177

[11] M. Donszelmann, C. Gaspar:
Distributed Information Manager,
forthcoming DELPHI Note

[12] Ph. Charpentier *et. al.*:
Background Measurements in the DELPHI experiment,
DELPHI 92-147 PHYS 240

[13] M.J. Clayton:
Proposal for the Protection of the LEP,
SL internal note, 14th January 1992

DELPHI Collaboration

DELPHI 90-30 GEN 110 MIG 4

12 July 1990

VSAT RESULTS OF THE LEP BEAM SEPARATION SCAN

S. Almehed [1], J. Bjarne [1], W. Bonivento[2], H. Carling[1], R. Cirio[3], A. De Min[2], D. Gamba[3], G. Jarlskog[1], U. Mjörnmark[1], P. Poropat[4], G. Rinaudo[3], A. Romero[3], M. Sessa[4], E. Vallazza[3],

[1] University of Lund
[2] INFN Milano
[3] INFN Torino
[4] INFN Trieste

VSAT results of the LEP beam separation scan

S. Almehed[1] J. Bjarne[1] W.Bonivento[2] H. Carling[1]
R. Cirio[3] A. De Min[2] D. Gamba[3] G. Jarlskog[1]
U. Mjörnmark[1] P. Poropat[4] G. Rinaudo[3]
A. Romero[3] M. Sessa[4] E. Vallazza[3]

13 June 1990

1 Introduction

In order to obtain the maximum available luminosity, the electron and positron beams of LEP must collide head-on, i.e. with minimum relative separation. These optimum positions can be found by changing the relative beam positions while measuring the resulting Bhabha scattering rate. Useful results concerning the beam background profile can also be extracted from these measurements. One can also, in principle, calculate the beam width from these data.

A beam separation scan was carried out on May 2 1990 to determine the optimum beam positions for the four LEP experiments. This note describes the results of this scan obtained by the VSAT detector at the DELPHI interaction point. The first part gives a brief overview of the general conditions of the measurements, while the second part deals with the data analysis. The main results are discussed in the third part, followed by the conclusions.

[1]University of Lund
[2]INFN, Milano
[3]INFN, Torino
[4]INFN, Trieste

2 General conditions of the beam separation scan

2.1 LEP beam parameters and DELPHI status

The beam separation scan was performed using two different values of the β-function: $\beta = 7.0$ cm. and $\beta = 4.3$ cm.

The beams were, for each β-value, moved relative to each other in the vertical direction only. Both beams were simultaneously moved symmetrically around the nominal zero position using electrostatic separators. Measurements were made at beam separations of 0 μm, 10 μm, 20 μm and 30 μm. For $\beta = 4.3$ cm measurements were also made at 45 μm separations. All the above settings were measured twice: with electron beam moved up and positron beam moved down and *vice versa*. For $\beta = 7.0$ cm and separation -30 μm, and for the second run at 0 μm, no VSAT measurements were made due to a temporary data acquisition problem.

About ten minutes of data collection were allowed for each of the settings, while measurements were taken for about 30 min for the first setting with $\beta = 7.0$ cm and 0 μm separation.

During the scan the beam currents in LEP decreased from about 1.0 mA to about 0.7 mA. Figure 1 shows the time variation of the electron and positron currents during this time. The product of the two currents is also shown here.

During the whole length of the scan the DELPHI solenoid was turned off due to a technical problem.

2.2 The VSAT detector

The VSAT detector [1] consists of four calorimeter modules. Each such module is composed of 12 silicon diodes (size 3x5 cm^2), separated by tungsten absorbers of two radiation lengths thickness. The energy resolution is about $35\%/\sqrt{E}$ for fully contained showers, i.e. about 5% at an energy of 46 Gev. Three silicon strip planes with one mm pitch placed at five, seven and nine radiation lengths into the modules are used for the (x, y) shower position measurement. The accuracy of locating a shower is about 300 μm.

The modules are placed very close to the elliptical beam pipe,

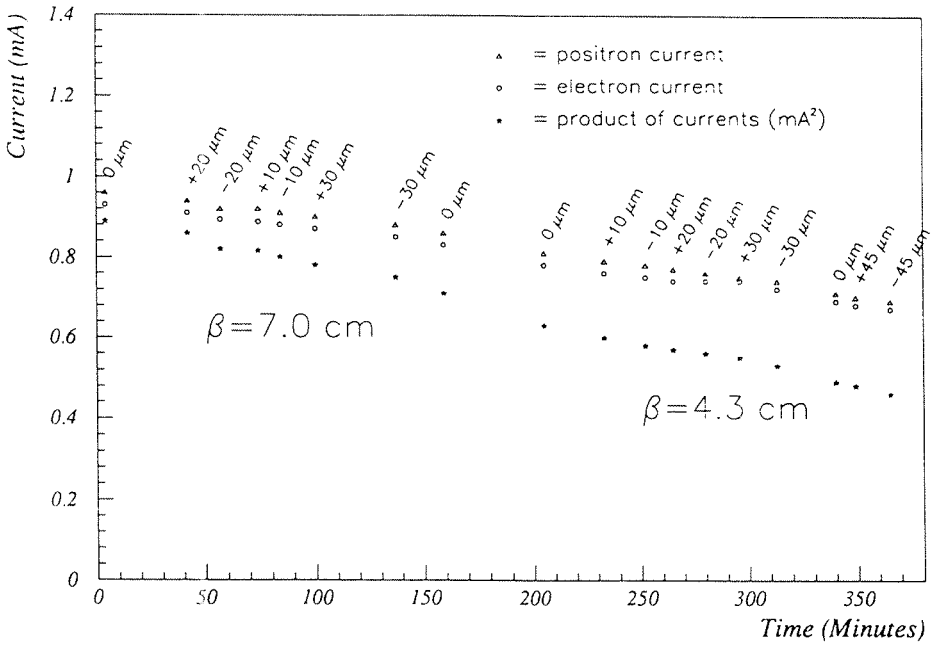

Figure 1: Time variation of LEP currents during the beam separation scan.

and on each side of it, at ± 7.7 m from the DELPHI interaction point (i.e. just outside the superconducting quadrupole magnets). The small-angle coverage makes the VSAT very suitable for luminosity measurements (by counting the number of Bhabha scattered electron-positron pairs) as well as for measurements of other beam parameters, background profiles etc.

To be able to handle even very high beam background counting rates the VSAT data acquisition uses variable down-scaling factors. Such down-scaling were applied for the off-momentum electron measurements described below.

Figure 2 shows an on-line monitoring event display of a VSAT Bhabha scattering event, giving profiles of showers, incident positions and pedestals. Note here also the coordinate definitions as used below in the presentation of the results.

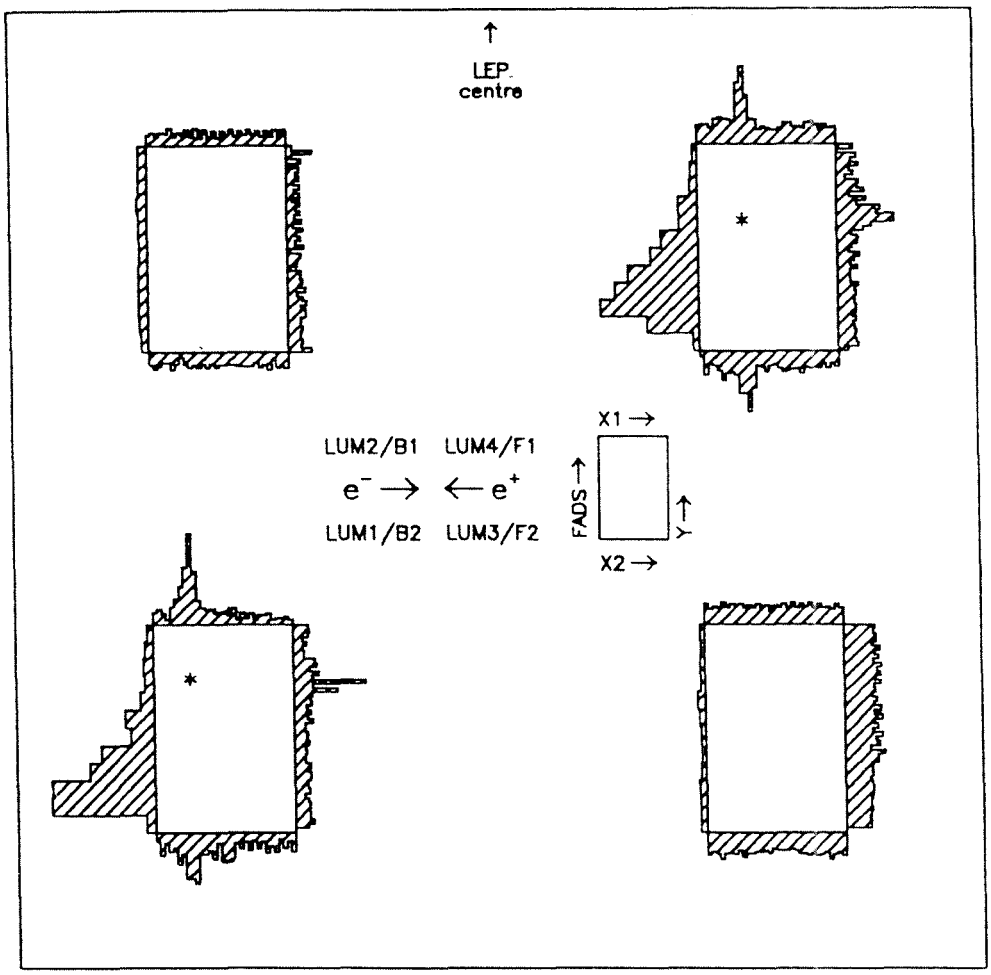

Figure 2: A Bhabha scattering event as seen by the VSAT on-line monitoring. Shown for each module are the shower profile (left vertical), x-position (upper and lower horisontal) and y-position (right vertical). Note VSAT coordinate definitions.

3 Data analysis

3.1 Data selection

The beam separation scan data were passed through an offline data analysis algorithm, containing the following cuts on incident position and energy:

The horizontal positions of the incident particles were given by the silicon-strip planes of the VSAT modules. A one millimetre cut from the calorimeter edges was applied in order to exclude events with considerable shower leakage.

The sum of the signals from the charge-sampling full-area silicon planes of a calorimeter gives a measure of incident energy. These sums were multiplied by position-dependent correction factors to compensate for transverse shower leakage of incident particles hitting close to an edge.

Figure 3 shows a scatter-plot over one of the two (compensated) VSAT Bhabha counting arms, showing the energy deposited in one module versus the energy deposited in its diagonal module. The square indicates the energy cuts used for the subsequent analysis. As can be seen, only signals corresponding to an energy in the range of about 35 GeV to about 55 GeV were considered belonging to the Bhabha scattering process.

In Figure 3 are also shown the projections of the scatter-plot on each axis after the energy cuts were applied.

For the off-momentum electron measurements only very low-energetic cuts were applied in order to subtract the pedestals.

3.2 Data evaluation

Bhabha scattered electrons and positrons are detected in two diagonal VSAT calorimeter modules. However, in the VSAT there is also quite a heavy rate due to beam background particles (off-momentum electrons) which can produce accidental coincidences.

This possible contamination of the data has to be taken into account. This was done by calculating the statistical probability of such background events from the measured rate of off-momentum electrons surviving the data selection cuts. For doing this we define

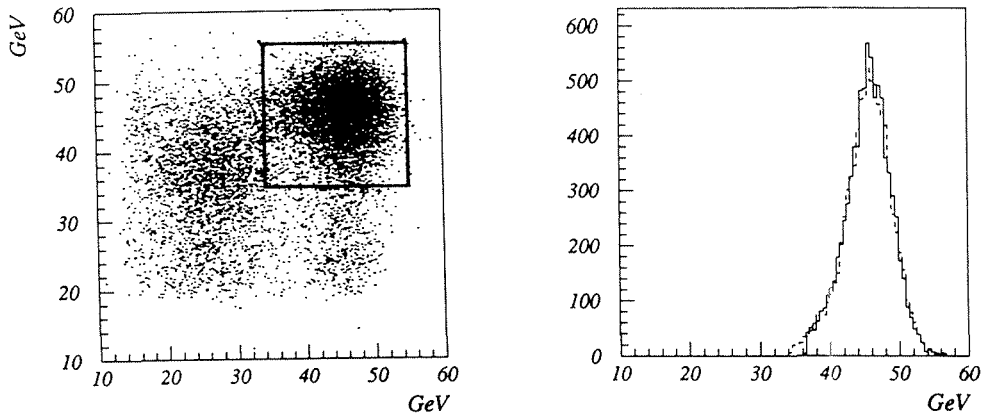

Figure 3: Scatter-plot over energy deposited in one module versus energy deposited in its diagonal module for Bhabha scattering events. The square indicates the energy cuts used. In the right picture are shown the projections of the scatter-plot on each axis after the energy cuts.

the following quantities for a given run:

N_{tru} = number of "true" Bhabha coincidences
N_{tot} = number of coincidences accepted by the Bhabha trigger
N_{acc} = number of accidental coincidences
N_{ref} = number of accepted electrons in one module only
N_{opp} = number of accepted electrons in the opposite module
N_{bco} = number of beam collisions per second
t_{cor} = VSAT dead time corrected duration of measurement

The calculated accidental Bhabha rate due to background is then

$$N_{acc} = \frac{N_{ref}\, N_{opp}}{N_{bco}\, t_{cor}}$$

This contamination has to be subtracted from the raw trigger-accepted Bhabha counts, finally giving

$$N_{tru} = N_{tot} - N_{acc}$$

To take care of the luminosity dependence on beam intensity all data were normalized by the beam currents as given by Figure 1.

The Bhabha counting rate data were normalized by the product of the beam currents, while the off-momentum electron rate data were normalized by their respective incident beam current. The off-momentum energy distributions were normalized to 500 events in each module.

The statistical errors on the corrected Bhabha counting data were calculated, adding both the errors on the statistics of Bhabha coincidences and of the background contamination in quadrature. For the off-momentum data, the errors were given by their statistics only. Since these errors are very small they are not seen in the plots below.

As this is a relative measurement, systematic errors should not affect the results very much.

4 Results

4.1 Bhabha scattering counting rates

The VSAT results concerning Bhabha scattering counting rates as a function of vertical separation of the LEP beams are shown in Figure 4 for $\beta = 7.0$ cm and $\beta = 4.3$ cm respectively.

As can be seen from this figure, the nominal zero separation case is the one giving the highest Bhabha counting rate, thus confirming that the normal beam positions do indeed give head-on collisions.

A β-squeeze from 7.0 cm to 4.3 cm is expected to lead to an increase in luminosity of about 60% for the LEP experiments. The measured luminosity increase due to the β-squeeze was, however, here found to be about 22%. This value is corrected by the 3% VSAT Bhabha counting rate change due to the 0.35% difference in quadrupole field strength of the two β-values.

In Figure 4 are also shown (open markers) the statistically calculated background of accidental Bhabhas. This rate is seen to be fairly constant, independent of changes in beam separation, indicating that small changes in beam position does not have a significant effect on the background.

4.2 Off-momentum electron counting rates and energy distributions

Data with signals in only one of the four VSAT modules were not only used for the estimation of the accidental Bhabha rate, but were also recorded to give a measure of the off-momentum electron background profile around the DELPHI interaction point. Figure 5 shows the off-momentum electron rates for the four modules for both β-values.

For $\beta = 7.0$ cm the two modules on the inner side of LEP both have a rate of about 60 Hz, which increases after the β-squeeze by a factor 2 for one module and 2.5 for the other.

The outer modules have counting rates of about 200 Hz and 300 Hz respectively. These rates are approximately independent of the β-value.

From Figure 5 it is clear that the off-momentum electron counting rate is fairly constant for different beam separations.

Figure 6 shows the energy distributions of the four VSAT modules for both the inner recpectively the outer modules and for both β-values with zero beam separation.

The outer modules do not change their energy distributions when the β-value is changed. The inner modules, on the other hand, do see more high energy background for $\beta = 4.3$ cm.

5 Conclusions

The beams were found to collide head-on with the nominal, zero separation field, beam conditions.

An increase in luminosity of about 22% was found after a β-squeeze from 7.0 cm to 4.3 cm.

The Bhabha counting profiles obtained during the beam separation scan can, unfortunately, not readily be used to extract the vertical beam width due to lack of detailed information on beam-beam interactions, producing non-Gaussian tails.

The vertical beam separations did not significantly affect the off-momentum electron rate, which tends to be higher on the outer side of LEP than on the inner. The β-squeeze did, however, ap-

proximately double the rate on the inner side of LEP. The rate on the outer side remained fairly constant.

The off-momentum electron energy distributions remained the same after a β-squeeze on the outer side of LEP, while the inner side distributions shifted to higher energy with the lower β-value.

Acknowledgements

We would like to thank G. von Holtey for fruitful discussions and critical comments on this report. Thanks are due also to V. Meertens and R. Schmidt.

References

[1] F. Bianchi et. al.,
Very Small Angle Electron Tagger for DELPHI,
DELPHI 88-2 GEN-72

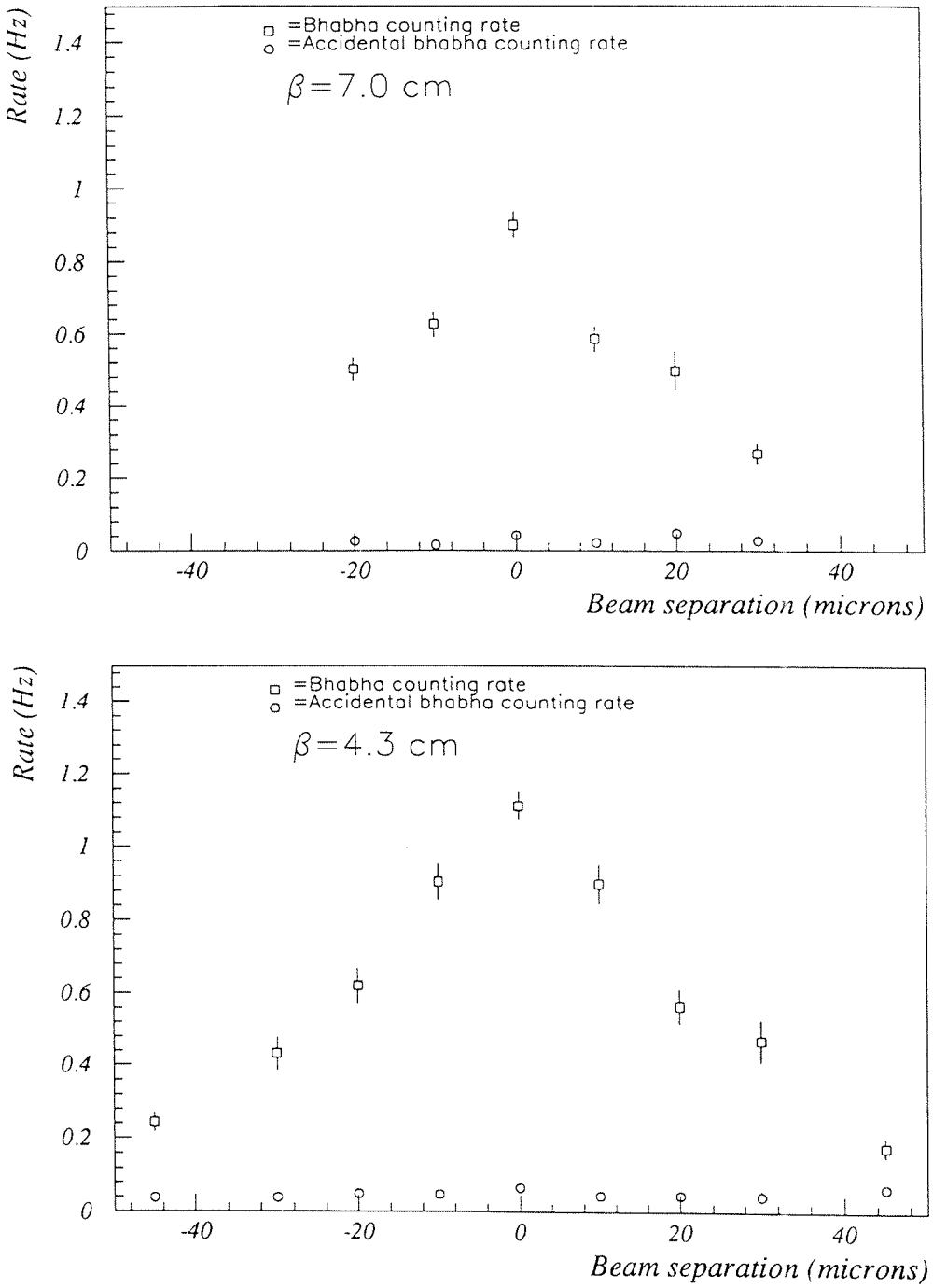

Figure 4: Bhabha scattering counting rates as a function of beam separation for $\beta = 7.0$ cm and $\beta = 4.3$ cm. The calculated accidental Bhabha rates are shown in open markers.

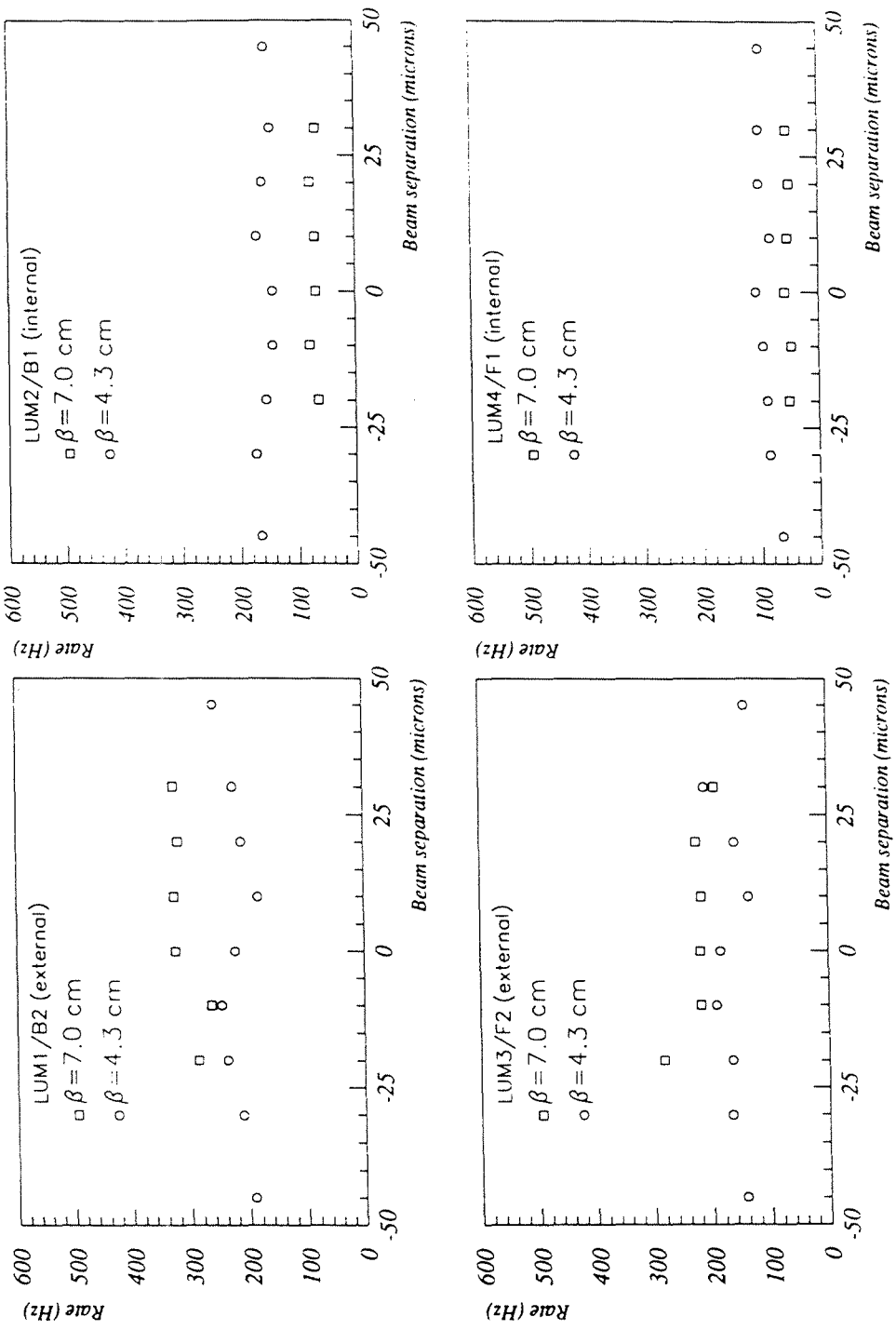

Figure 5: Off-momentum electron counting rates as a function of beam separation for $\beta = 7.0$ cm and $\beta = 4.3$ cm for the four VSAT modules.

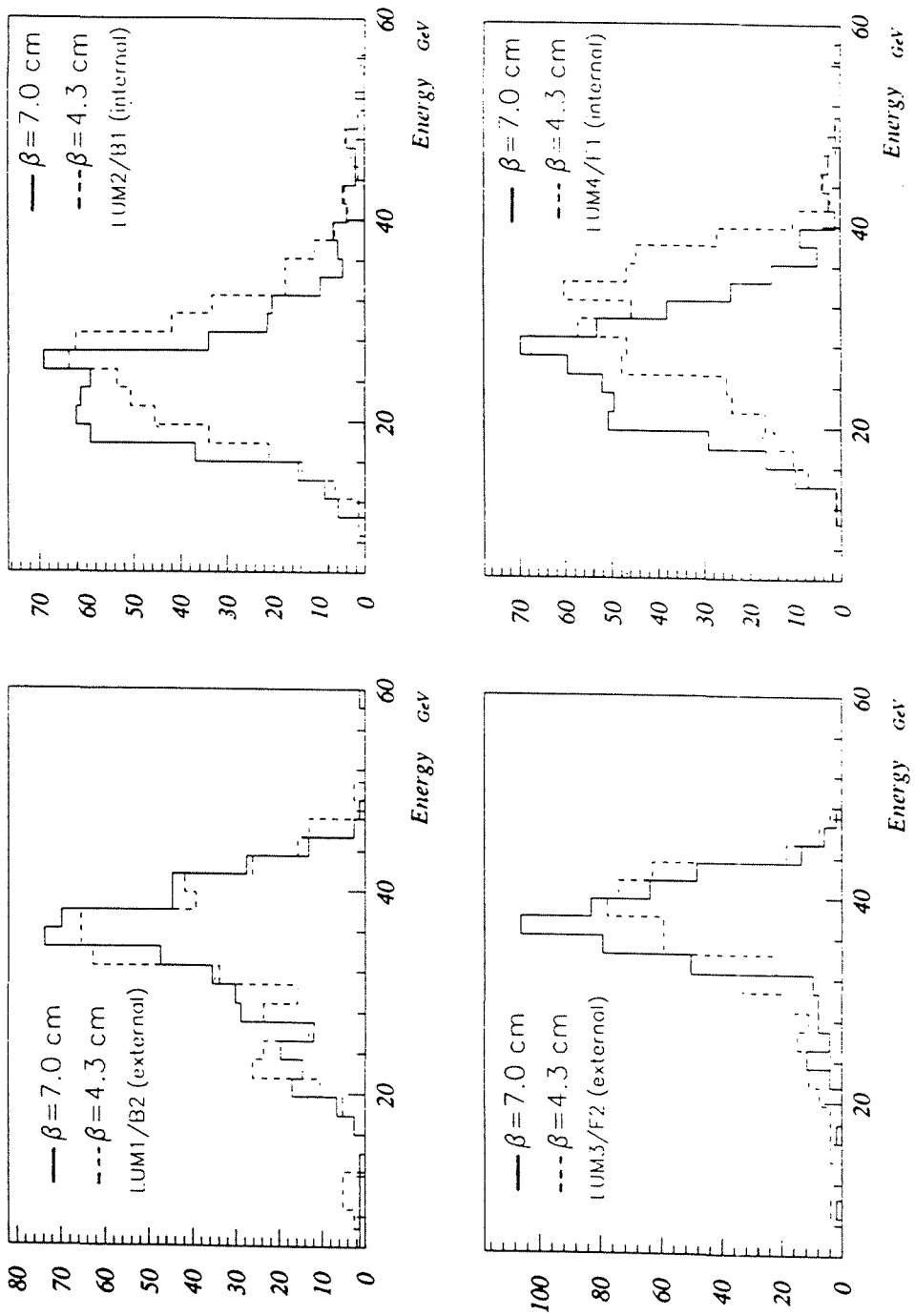

Figure 6: Energy distributions (normalized to 500 events) of off-momentum electrons for $\beta = 7.0$ cm and $\beta = 4.3$ cm for the four VSAT modules.